Intrinsic electrical activity in gonadotropin-releasing hormone neurons: a modelling study

Spencer Moran
Department of Mathematics and Statistics
McGill University, Montreal

August 2015

A thesis submitted to McGill University in partial fulfillment of the requirements of the degree of Master of Science

Contents

List of Figures

List of Tables

Abstract

Gonadotropin-releasing hormone (GnRH) neurons are neurosecretory cells of the vertebrate diencephalon that regulate fertility through pulsatile secretion of GnRH into the median eminence. The physiological mechanism for pulsatile release of GnRH is hypothesized to depend on the intrinsic electrical activity of these cells, which in mice includes two endogenous modes of action potential burst firing; namely *parabolic* and *irregular* bursting. In this thesis, we develop a stochastic Hodgkin-Huxley-like model of the electrical activity in a single GnRH neuron and use it to (i) predict the contributions of specific ionic currents in the generation of parabolic and irregular bursting, and (ii) investigate the mathematical mechanisms underlying bursting behaviour. As part of the model development process, we obtain new data-based submodels for several ionic currents that have been pharmacologically isolated in GnRH neurons. Through numerical simulations, we find that the model generates parabolic and irregular bursting solutions that agree qualitatively with electrophysiological recordings. We show that the type of bursting generated by the model can be toggled by changes in the conductances of certain ionic currents, notably those of a slow inward Ca^{2+} current and a Ca^{2+}-activated K^+ current. The parabolic and irregular bursting models are analyzed using numerical bifurcation techniques, revealing that the two models actually share a common topological structure in their fast subsystems. Despite this mathematical similarity, the two models differ in one major aspect: parabolic bursting is not dependent on neuronal noise, whereas irregular bursting relies on slow stochastic fluctuations that push the system past the threshold for firing. Lastly, we demonstrate that a canonical model for bursting, where spiking is initiated and terminated through passage of a saddle-node on invariant circle bifurcation in the fast subsystem, can also produce both types of bursting.

Résumé

Les neurones GnRH sont des cellules neurosécrétrices qui appartiennent à la diencéphale des vertébrés et qui réglementent la fertilité en sécrétant l'hormone GnRH dans une manière pulsatile dans l'éminence médiane. On fait l'hypothèse que le mécanisme physiologique de ce phénomène dépend sur l'activité électrique intrinsèque de la neurone, qui dans les souris comprend de deux types d'éclatement endogènes de potentiel du membrane; en particulier l'éclatement *parabolique* et l'éclatement *irrégulier*. Dans cette thèse, on construit un modèle stochastique de la forme Hodgkin-Huxley pour l'activité électrique dans une seule neurone GnRH et on l'utilise pour (i) prédire les contributions spécifiques des courants ioniques à la génération de l'éclatement parabolique et irrégulier, et (ii) étudier le mécanisme mathématique par laquelle l'éclatement se manifeste. Comme partie du processus du dévéloppement du modèle, on obtient de nouveaux modèles pour certains courants ioniques qui sont établis en accord avec les données expérimentales. Avec l'aide de la simulation numérique, on trouve que le modèle génère des solutions d'éclatement paraboliques et irrégulières qui sont en accord qualitativement avec les enregistrements électrophysiologiques. On montre que le type d'éclatement produit par le modèle peut être activé/désactivé par un changement des paramètres de résistance appartenant à un courant Ca^{2+} et un courant K^+ activé par Ca^{2+}. Les modèles paraboliques et irréguliers sont analysés avec des méthodes de bifurcation numériques révélant que les deux modèles ont une structure topologique en commun dans leurs sépérations rapides. Bien qu'ayant une similarité mathématique, les deux modèles se distinguent par un aspect majeur: l'éclatement parabolique ne dépend pas sur la fluctuation stochastique alors que l'éclatement irrégulier dépend sur de lentes fluctuations qui dirigent la trajectoire au seuil de l'excitabilité. Finalement, on démontre qu'un modèle réduit pour l'éclatement, où l'excitabilité est débutée et terminée par une bifurcation SNIC dans la séparation rapide, peut aussi générer les deux types d'éclatement.

Acknowledgements

The author would like to acknowledge the support of various individuals and groups in the development of this thesis. To begin, I would like to commend my supervisor, Dr. Anmar Khadra for his patience and his invaluable feedback during the development of the model and the editing of this thesis. Secondly, I would like to recognize the efforts of Dr. Suzanne Moenter and her lab at the University of Michigan for providing us with experimental recordings of GnRH neurons. Next, I would like to thank my lab colleagues, Laurent MacKay, Tina Mitre, Shalon Liu, and Dr. Majid Jaberi for their insights offered during group meetings and their willingness to help at any time of day. Of course, I am also grateful to the Department of Mathematics and Statistics at McGill University that provided partial funding throughout the entire program, and supported my research efforts in the cross disciplinary field of mathematical biology. Last but not least I would like to thank my family, and Emily Walsh, for all their love, support, and patience during my stay at McGill.

Chapter 1

Introduction

This thesis is comprised of a detailed study of a newly developed model for intrinsic electrical activities in gonadotropin-releasing hormone (GnRH) neurons. The study emphasizes the quantitative fitting methods used during model development, the role of individual ionic currents in generating bursting behaviour, and the topological properties of bursting solutions exhibited by the model.

We begin this chapter by providing a physiological context for the model presented in this thesis. Next, we review previous modelling efforts for GnRH neurons to motivate the objectives of the model, as presented in the final section of this chapter. The rest of the thesis is constructed as follows. In the second chapter, we review some of the mathematical tools used for the development and analysis of the model, including stochastic differential equations (SDEs) and slow-fast subsystem analysis. The model is developed in the third chapter, where we describe in detail the methods used to estimate free parameters for each component of the model, and show the results of model fits to data. In the fourth chapter, we show the numerical results obtained for the two types of bursts, describe the effects of various ionic currents on burst characteristics, and provide a geometric analysis of bursting solutions. In the final chapter, we summarize our findings, discuss limitations and physiological implications of the model, and suggest future research directions.

1.1 Physiology of GnRH neurons

GnRH neurons are one member of a class of hypothalamic neurons that synthesize and secrete hormones to regulate the function of the anterior pituitary. These hypothalamic neurons, named after the hormone they produce, project into the median eminence of the

hypothalamus where secreted hormones enter the bloodstream via the hypophyseal portal system [2]. GnRH stimulates the release of two gonadotropins—luteinizing hormone (LH) and follicle-stimulating hormone (FSH)—from the pituitary, making GnRH neurons the final neural output controlling fertility in the hypothalamo-pituitary gonadal (HPG) axis [3]. A pulsatile profile in the output of GnRH is essential for effective release of gonadotropins [4], which are further regulated by the amplitude and frequency of GnRH pulses [5]. The period of GnRH pulses ranges from 30 minutes to hours and is dependent on the reproductive state of the organism [3]. As indicated in Figure 1.1.1, the secretion of GnRH is regulated (in part) by the gonadal steroid estradiol, which in females, exerts negative and positive feedback on GnRH release depending on the stage of the menstrual or estrous cycle [6].

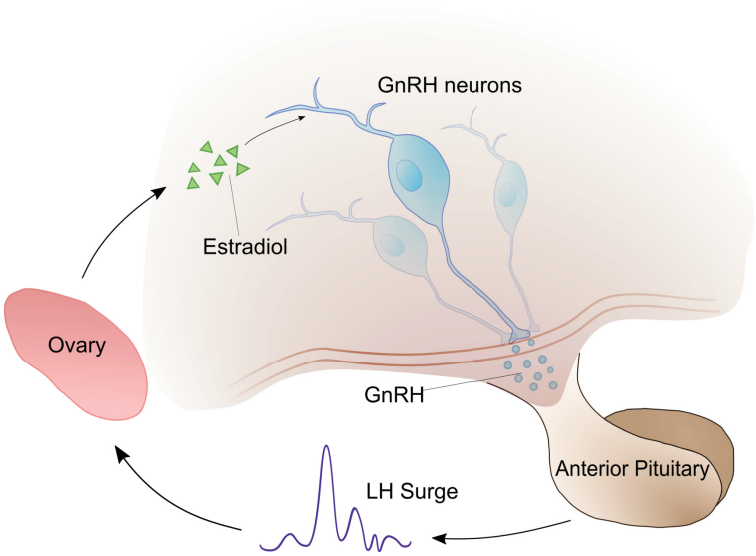

Figure 1.1.1: Schematic of the role of GnRH neurons within the HPG axis.

The determination of the complete mechanism underlying the pulsatile release of GnRH is still an open topic of research. However, the dependence of hormone release on phasic action potential (AP) firing in magnocellular neurons [7, 8]—another type of neuroendocrine cell—suggests that spontaneous electrical activity in GnRH neurons is crucial for GnRH release. In support of this claim, GnRH release in the median eminence is found to be AP-dependent [9]. What is unclear, however, is how specific patterns in AP firing modulate the profile of hormone release.

Burst firing or *bursting*, a commonly observed pattern of electrical activity in neurons, is defined by the repetition of a *burst*—the sequential firing of two or more APs—followed by a period of quiescence called the *interburst interval*. A recent electrophysiological study employing whole-cell patch clamp methods showed that GnRH neurons exhibit at least two

types of bursting [10]. The first type, referred to as *irregular* bursting [10], has been observed in other studies [11, 12], and is characterized by wide variation in interburst interval and burst duration, with quiescent phases corresponding to a stable baseline membrane potential. Despite the wide variation in interburst interval, one study found that the majority of bursts in their sample were separated by an interval of less than 20 seconds [13]. In the same study, the average duration of the burst was found to be less than 10 seconds for a subset of the sample. Another study showed similar results for two representative GnRH neurons, where active and quiescent phase durations did not exceed one minute [10]. A representative recording of a GnRH neuron exhibiting irregular bursting is shown in Fig. 1.1.2b. The second type of bursting—referred to as *parabolic* bursting—is rare (occurring in only 1-2% of cell population), and has only been documented in one published study [10]. This type of bursting is characterized by an oscillatory membrane potential—with a period on the order of seconds—that alternates between an active phase of AP firing and a quiescent phase, where the cell repolarizes well below the threshold for firing. Furthermore, the interspike interval as a function of the spike count during the burst resembles a convex parabola. This burst phenotype, depicted in Fig. 1.1.2a has been observed in other types of neurons, notably in the R15 neuron of *Aplysia* [14].

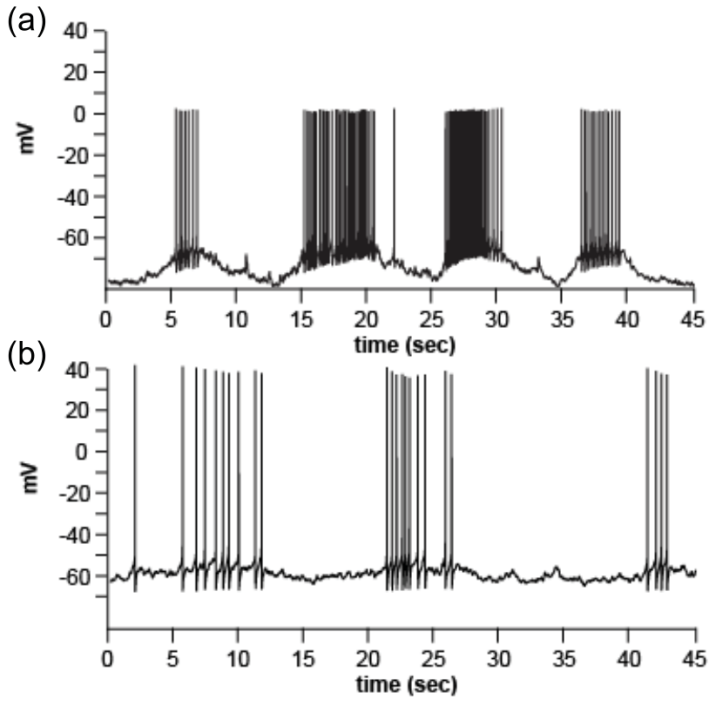

Figure 1.1.2: Two types of bursting recorded in current-clamp mode from GFP-identified GnRH neurons in brain slices of mice. Time series of membrane potential during (a) parabolic bursting and (b) irregular bursting.

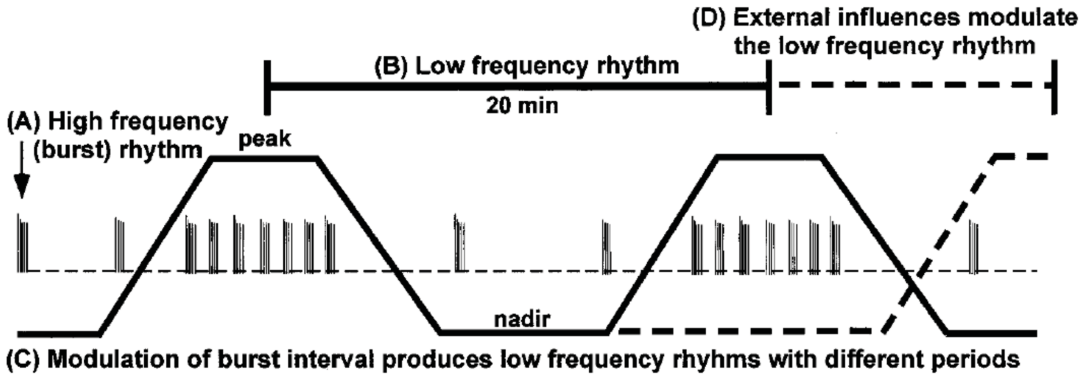

Figure 1.1.3: Biological model of Nunemaker et al. [15] for co-existing rhythms in GnRH neurons. Figure used with permission.

Since pulsatile hormone release occurs with a much lower frequency than that typically observed during parabolic and irregular bursting, it is unlikely that there exists a one-to-one correspondence between a burst of APs and a spike in hormone release. In an attempt to find underlying rhythms that operate on the same timescale as hormone release, one study carried out a spectral analysis of long duration time series from extracellular recordings of firing patterns in GnRH neurons [15]. The spectral analysis revealed two classes of rhythmic events—*clusters* and *episodes*—classified by periods of 100-1000 sec. and >1000 sec. respectively. These low frequency events correspond to slow modulation of AP firing rate. Changes in the firing rate are attributable to changes in the interburst interval, since spike count and duration of the burst did not vary significantly between episodes. The authors proposed a biological model of interacting electrical rhythms in GnRH neurons (Fig. 1.1.3), where bursts are the "fundamental units of activity" required for hormone release. The model suggests that external agents (such as estradiol) modulate interburst interval to produce low frequency rhythms that conform with the pulsatile release of GnRH at a similar frequency.

Given that bursting may be crucial for GnRH pulse generation, it is natural to study the ionic mechanisms governing it. A large body of literature exists on the properties of individual ionic currents conducted by GnRH neurons, which in mice include two types of Na^+ currents [16], various subtypes of Ca^{2+} and K^+currents [17, 18, 19], and a non-selective cation current [20]. A comprehensive list of currents that have been isolated in GnRH neurons and a brief description of their physiological characteristics are provided in Table 1.1. For a more detailed summary of these currents, the reader is pointed to a recent review of GnRH neuron electrophysiology [3]. A handful of studies cited in Table 1.1 also examine the effects of estradiol (*in vivo* [19, 16, 10] and *in vitro* [21]) on the quantitative

properties of various current(s). For instance, one study found that estradiol administered *in vivo* significantly alters the maximum current density and shifts the $V_{\frac{1}{2}}$ parameter of the steady-state inactivation curve of I_A [19]. Since I_A is an outward current that is active at voltages near the baseline potential [22], this result suggests that estradiol targets I_A to modulate the excitability of the cell, which in turn may impact bursting characteristics.

Current	Description	References
I_{NaF}	Tetrodotoxin (TTX)-sensitive transient (fast) Na^+ current primarily responsible for the generation of APs.	[16, 23]
I_{NaP}	TTX-sensitive persistent Na^+ current that may contribute to the generation of afterdepolarization potentials in GnRH neurons.	[24, 16]
I_A	Large-amplitude transient K^+ current. Block of I_A by 4-aminopyridine (4-AP) reduces latency to spike firing.	[19, 22]
I_K	Non-inactivating delayed-rectifier K^+ current. Likely active in the repolarization phase of the AP.	[22, 19]
I_M	K^+ current that is activated by GnRH to reduce excitability in GnRH neurons.	[25]
I_{Kir}	G-protein activated inwardly-rectifying K^+ (GKIR) current that has been evoked in the immortalized GT1 cell-line and contributes to suppressing excitability.	[26]
I_{KCa}	Ca^{2+}-activated K^+ current. Consists of at least two subtypes: (i) a current with small single-channel conductance (I_{SK}) active in controlling excitability and medium duration afterhyperpolarization (AHP), and (ii) a current with "big" single-channel conductance (I_{BK}), likely involved in repolarization of the AP. A third type ($I_{AHP-UCL}$) contributing to slow AHP formation has also been proposed but the channel conducting $I_{AHP-UCL}$ has yet to be verified.	[17, 27, 28, 29]
I_{HVA}	Large amplitude high voltage-activated Ca^{2+} current. Causes influx of Ca^{2+} into the cell during spiking. Comprised of several different current subtypes (L,N,P/Q,R) denoted by I_{CaL}, I_{CaN}, etc.	[30, 18]
I_{LVA}	Low amplitude low voltage-activated Ca^{2+} current conducted by T-type Ca^{2+} channels. May be implicated in rhythmic behaviour due to high input resistance of GnRH neurons.	[18, 31]
I_h	Hyperpolarization-activated cation current. Block of I_h by ZD7288 decreases spike count in current injection experiments.	[20]

Table 1.1: Brief descriptions of ionic currents expressed in GnRH neurons. For each current, references to experimental studies are provided.

One important characteristic of both types of bursting is that it is intrinsic [12, 11, 10], meaning that it persists in the absence of synaptic inputs or currents applied by the experimenter. It follows that bursting activity occurs from the interaction of non-synaptic

currents conducted by voltage- and calcium-gated ion channels embedded in the membrane of the soma and dendrites of these neurons. Electrophysiological experiments such as those cited in Table 1.1, provide only a rough idea of the mechanisms underlying the burst, since they study the effects of each current individually. What is not gained from these studies, however, is an understanding of how the individual ionic currents interact to generate rhythmic behaviour. Mathematical modelling is a useful tool for understanding bursting since one can quickly test physiologically plausible combinations of ionic currents to see if they can generate the rhythmic behaviour observed experimentally. Once this is achieved, the model can then be validated against new experiments, and fine-tuned to agree with experimental results. With a successful model, one can then make informed predictions about the role of certain ionic currents in bursting through the variation of model parameters.

1.2 Existing GnRH neuron models

Several mathematical models have previously been developed to describe various phenomena associated with bursting and/or excitability in GnRH neurons. We summarize these models here in a chronological fashion. Note that some of these models are actually based on electrophysiological data from immortalized GnRH-secreting neurons of the GT1 cell line. Given the progress in electrophysiological methods, it is now possible to use, for example, whole-cell patch-clamp techniques to record GFP-identified GnRH neurons from brain slices in adult mice [18]. All of the models reviewed in this section are of the Hodgkin-Huxley (HH) type, and it is assumed that ionic currents can be described using the HH formalism [32] unless otherwise stated.

Van Goor et al., 2000 [33]

In the first study that we review, the authors investigate the phenomenon of "spike-broadening" in GT1 cells, defined as an increase in AP width and amplitude that leads to an increase in Ca^{2+} influx during spiking. To confirm the ionic mechanisms responsible for spike-broadening, the authors develop an electrical model for GT1 cells, that serves as a framework for several future studies mentioned in this section. The set of spiking currents used in the model, namely I_{NaF}, I_{CaL}, I_{CaT}, I_K, I_M, I_{Kir}, along with a Ca^{2+}-carrying leak current I_d, are modelled according to voltage-clamp data. Of note in the previous set of currents is I_{NaF}, which is not modelled using the typical HH formalism for the fast Na^+ current, but rather a reversible four-state Markov model. The spike trains produced by the model show qualitative agreement with experimental results and the model is able to reproduce the phenomenon of spike-broadening.

Lebeau et al., 2000 [34]

In this study, the authors investigate the role of Ca^{2+}-mobilizing and adenylyl cyclase (AC)-coupled receptors in controlling excitability in GT1 cells through an extension of the model by Van Goor et al. [33]. The ionic currents appearing in the voltage equation are conceptually divided into two main groups. The first consists of the spiking currents from the model by Van Goor et al. [33] that operate on a fast time scale. The second consists of the slow "pacemaker" currents that interact with the multicompartmental Ca^{2+} subsystem, including the small-conductance Ca^{2+}-activated K^+ current I_{SK}, a store-operated Ca^{2+} channel I_{SOC}, and a Ca^{2+}-dependent inward Ca^{2+} current I_d. The effect of GnRH on Ca^{2+}-mobilizing receptors is realized in the model through a decrease in the parameter representing ER membrane permeability. Similarly, the effect of forskolin on AC-coupled receptors is realized through an increase in the maximum conductance parameter of I_d. This model does not explain how intrinsic bursting is generated, but rather focuses on the effect of external modulators (e.g. GnRH, forskolin) on membrane excitability.

Roberts et al., 2009 [35]

In contrast with several of the models reviewed in this section, the model developed by Roberts et al. accounts for the bipolar morphology (one dendrite, one axon) typically observed in GnRH neurons. This morphology leads to heterogeneity in the passive properties (capacitance, resistance) of different sections of the membrane, which affects the recording of current at the soma. Therefore, models which aim to reproduce electrical activity recorded at the soma are more realistic if they account for the morphology of the cell. The authors of this study do so by developing a multicompartmental model using the neurocomputational tool GENESIS (GEneral NEural SImulation System http://www.genesis-sim.org/GENESIS/). For the somatic compartment, the authors assume the presence of I_{NaF}, I_{NaP}, I_K, I_M, I_{Kir}, I_{CaL}, and I_{CaT}. Except for I_{NaF} and I_{NaP}, all currents are adapted from the model of Lebeau et al. [34]. Whereas the active dendritic compartments are assumed to conduct I_{NaF} and I_{NaP}, the axonal compartments are assumed to conduct I_{NaF}, I_{NaP}, and I_K. While bursting is not considered here, a key finding of this study is that afterdepolarization (ADP) amplitude is found to decrease with increasing length of the dendrite.

Fletcher and Li, 2009 [36]

The model presented in this study is an extension of the model presented in Lebeau et al. [34] but with the reduced set of currents I_{NaF}, I_{CaL}, I_K, I_{Kir}, I_d, I_{SOC}, and I_{SK}. The novel component of this model is a two-compartment (cytosol and endoplasmic reticulum (ER)) Ca^{2+} submodel that accounts for spatial diffusion of $[Ca^{2+}]$ in each compartment. The ER and cytosolic Ca^{2+} concentrations ($[Ca^{2+}]_{ER}$, $[Ca^{2+}]_i$) are assumed to be spherically

symmetric, resulting in a partial differential equation (PDE) model for $[Ca^{2+}]_{ER}$ and $[Ca^{2+}]_i$ that depends on one spatial dimension, r. Another distinguishing feature of this study from that of Lebeau et al. [34] is that the model exhibits two types of qualitatively different bursting behaviour, where each type of bursting occurs through a different physiological mechanism. The two types of bursting share some features with the parabolic bursting observed in [10], but in both cases, the bursts do not have the characteristic parabolic profile in interspike interval, and the spikes do not undershoot the plateau of the underlying slow oscillation. The first type of bursting occurs via a time-dependent increase in inositol trisphosphate (IP_3) concentration, which in turn increases Ca^{2+} release from the ER to initiate bursting. It is unclear, however, from the figures presented in this study whether bursting is periodically sustained in this case. The second type of bursting is intrinsic (does not require time-dependent changes in parameters), and is due to an interaction between I_{SOC} and the dynamics of $[Ca^{2+}]_{ER}$. This second type of bursting appears to be periodically sustained.

Duan et al., 2011 [1]

In this study, the focus is set on the modelling of irregular bursting behaviour. The authors develop a model that combines components adapted from previous models reviewed in this section, as demonstrated in Figure 1.2.1. The two-compartment Ca^{2+} submodel is similar to that of Fletcher and Li [36], but diffusion is not accounted for. A distinguishing feature of this model is the inclusion of $I_{AHP-UCL}$, a UCL2077-sensitive, Ca^{2+}-activated K^+ current [28] that contributes to the "slow" AHP, in contrast to I_{SK}—a "medium" AHP current [17]. The current $I_{AHP-UCL}$ plays the role of a pacemaker current during irregular bursting simulated by the model. It is activated by Ca^{2+} released from IP_3 receptor-dependent stores in the ER. The irregular bursting can be roughly explained as a periodic interruption of spiking due to activation of I_{SK}, followed by activation of $I_{AHP-UCL}$, whose slow deactivation generates long interburst intervals. The re-activation of $I_{AHP-UCL}$ during the quiescent phase is prevented by the uptake of Ca^{2+} into the ER, and the efflux of cytosolic Ca^{2+} by the ATPase and Na^+/Ca^{2+} exchange pumps (see Fig. 1.2.1a). Spiking resumes once $I_{AHP-UCL}$ is sufficiently deactivated. Stochasticity in interburst interval, a key characteristic of irregular bursting, is obtained by coupling white noise processes to the open state equations of $I_{AHP-UCL}$. A model simulation of irregular bursting behaviour from their model is shown in Figure 1.2.1b. Note the persistence of Ca^{2+} transients after the firing of action currents, due to Ca^{2+}-induced release of $Ca^{2+}$from IP_3 receptors. The authors of this study, however, did not show whether the model can generate parabolic bursting, and did not include model simulations of membrane potential during bursting (they only show the total ionic current and Ca^{2+}). Therefore, it is unclear if the model can generate parabolic bursting behaviour

and if simulations agree with experimental recordings of voltage obtained during irregular bursting.

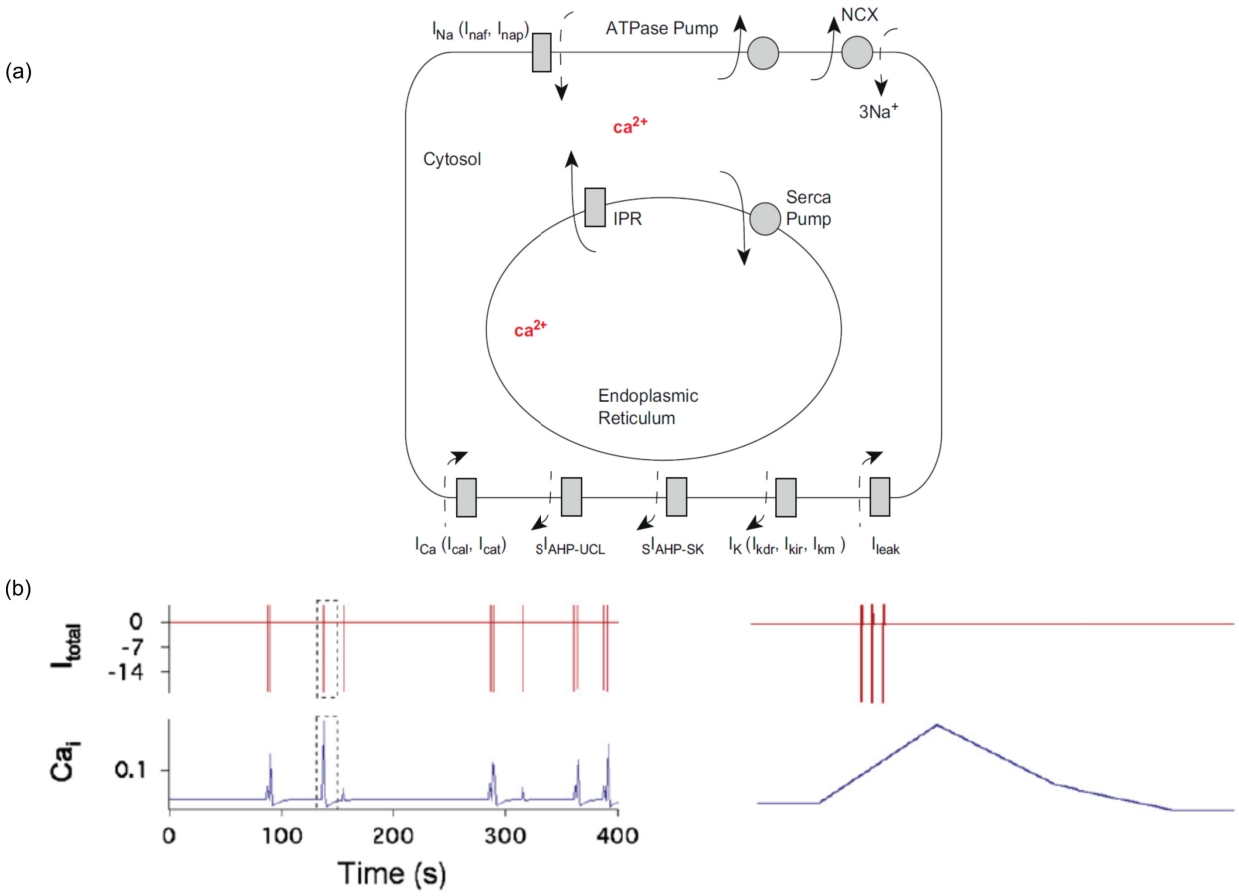

Figure 1.2.1: (a) Schematic representation of the GnRH neuron model developed by Duan et al. [1]. (b) Model simulation of total ionic current (*top*) and intracellular Ca^{2+} concentration (*bottom*). Figures used with permission.

Csercsik et al., 2012 [37]

The model presented in this study takes a hybrid approach to the modelling of membrane currents in GnRH neurons. This means that, in the soma, the spike generating mechanism is abstracted by a simple quadratic integrate-and-fire model [38], whereas the currents interacting with the two-compartment Ca^{2+} submodel are described using a HH formalism. These Ca^{2+}-related currents consist of I_{SK}, and $I_{AHP-UCL}$ adapted from Duan et al. [1], along with the new currents I_{Ca} (representing the combined current $I_{HVA} + I_{LVA}$) and I_{DAP}. The depolarizing afterpotential (DAP/ADP) current I_{DAP} is modelled by a HH-like Na^+ current with Ca^{2+}-dependent activation and inactivation in order to account for the presence of ADPs observed experimentally [24]. The expression for the voltage-gated Ca^{2+} current I_{Ca} is also of the HH-form, and was parameterized by fitting to the voltage-clamp

data in [30]. Additionally, the authors account for the morphology of the GnRH neuron by the inclusion of one active and one passive dendritic compartment. The total ionic current in the active dendritic compartment is described using the same spiking model as in the soma but with no additional Ca^{2+} currents. The model does exhibit irregular bursting in the presence of synaptic input and also supports an intrinsic mode of bursting. However, there is no clear indication whether the model can generate parabolic bursting solutions.

Chen et al., [39]

In the final study that we review, the authors extend the bursting model by Duan et al. [1] to account for the morphology of the cell. In the extended model, it is assumed that the neuron is unipolar (one dendrite), and consists of four distinct compartments: (i) the soma, (ii) the proximal dendrite, (iii) an AP initiation site (iSite) within the dendrite, and (iv) the distal dendrite. The inclusion of the iSite is due to a study by Iremonger and Herbison [40] showing that APs are mostly initiated from a point within the proximal dendrite ($<$100 μm from the soma), where dendritic Na^{+} channel density is the highest. This means for example, that a small depolarization at the soma can trigger an AP at the iSite, which then back-propagates to the soma to generate an AP there. In contrast with the model by Csercsik et al. [37], this extended model uses a one-dimensional cable equation to describe the spatial and temporal dependence of membrane potential. The neuronal compartments are divided up spatially, with the soma occupying an interval $[0, x_1)$, the proximal dendrite extending from $[x_1, x_2)$, and so forth. The equation for cytosolic Ca^{2+} concentration is also assumed to be spatially dependent: a Ca^{2+} diffusion term is included in the equation, but the authors find this formalism to have no effect on the behaviour of the model. The model also reveals that due to rapid diffusion of voltage along the dendrite, bursting is still controlled by ionic mechanisms at the soma, and burst patterns at the soma and iSite are the same, up to a small phase difference. Lastly, we note that this model is used in a more recent study [41] that investigates how synaptic input along the dendrite can modulate bursting and AP propagation.

1.3 Model objectives

Having covered the previous GnRH neuron modelling efforts, we are now ready to state the objectives of the model presented in this thesis. We motivate the objectives by addressing the primary scientific concerns with previous models.

One concern with the models reviewed above (with the exception of the Csercsik et al. [37] model), is that several of the equations for non-pacemaker or "spiking" currents are closely

adapted from the model of GT1 cells developed by Lebeau et al. [34]. Since the development of the Lebeau et al. [34] model, a handful of ionic currents, specifically members of the set $I_{ion} = \{I_{NaF}, I_{NaP}, I_A, I_K, I_{LVA}, I_{HVA}, I_h\}$ have been isolated and recorded from brain slices in GnRH neurons using whole-cell patch-clamp techniques (see Table 1.1). These recent results indicate that a new GnRH neuron model should be developed to include revised versions of the ionic currents appearing in Lebeau et al. [34]. Moreover, it is clear from the models presented above that none of them explicitly incorporate I_A or I_h, which are known to (i) affect the excitability of the membrane, and (ii) operate on medium to slow time scales. This suggests that these two currents play an active role during bursting. Based on this, the first objective of the GnRH neuron model should be to accurately reproduce the characteristics of spontaneous (intrinsically generated) AP firing using the set of currents I_{ion} (and perhaps others, such as I_{KCa}), where each member of I_{ion} is fit to recent electrophysiological data.

The second major objective relates to bursting behaviour. As one can infer from the previous section, no published GnRH neuron model (to the author's best knowledge) has demonstrated the ability to simulate intrinsic parabolic bursting. Irregular bursting has been simulated by the models of Duan et al. [1] and Csercsik et al. [37] through the $I_{AHP-UCL}$ mechanism. However, the voltage- and Ca^{2+}-dependence of (in)activation for $I_{AHP-UCL}$ is not confirmed, and so the modelling of this current is based on phenomenological considerations. This is evident from the models using $I_{AHP-UCL}$ since the maximum conductance of this current is always assumed to be 1-2 orders of magnitude larger than that of all other currents. Furthermore, bursting obtained via the $I_{AHP-UCL}$ mechanism relies on a multicompartmental submodel of $[Ca^{2+}]_i$ that has a large number of unknown parameters. With this in mind, the second objective of the model is to simulate both parabolic and irregular bursting with the following constraints:

- The new ion channel data is taken into consideration.
- The parameters used to simulate both types of bursting lie within a physiologically reasonable range.
- The bursting mechanism does not depend on $I_{AHP-UCL}$.
- The bursting is intrinsic, i.e., the model does not require a periodic source of input to generate rhythmic behaviour.
- The dynamics of $[Ca^{2+}]_i$ are abstracted by a single compartment model in order to minimize the number of free parameters and variables in the combined model.

With a model that satisfies the above criteria, we will be able to determine the major differences between the two types of bursts exhibited by GnRH neurons in mice [10], and determine the role of various ionic currents in generating such bursts.

Chapter 2

Mathematical preliminaries

2.1 Stochastic differential equations (SDEs)

The GnRH neuron model developed in Chapter 3 is a set of ordinary differential equations that accounts for neuronal noise through the coupling of a stochastic process to one or more of the equations. The resulting set of equations then becomes a member of the class of stochastic differential equations (SDEs), that have a rich underlying theory. In this section, we present some introductory concepts in SDEs in order to prepare the reader for the presentation of the model. We mainly follow the treatment of the topic as presented in [42] and [43]. The discussion of numerical methods in Section 2.1.2 is adapted from [44].

We begin by defining the one-dimensional stochastic process $W(t)$, known as the *Wiener process* or *Brownian motion*—a fundamental concept in the theory of SDEs.

Definition A one-dimensional *Wiener process* $W(t)$, $t \in \mathbb{R}$ is a continuous stochastic process satisfying

- $W(0) = 0$.
- $W(t-s) \sim N(0, (t-s))$. In other words, the probability distribution function $p(w,t)$ of $W(t)$ satisfies the diffusion equation

$$\frac{\partial p}{\partial t} = \frac{1}{2}\frac{\partial^2 p}{\partial w^2}, \quad p(w,0) = \delta(w),$$
$$\text{therefore, } p(w,t) = \frac{1}{\sqrt{2\pi t}} \exp[-\frac{w^2}{2t}].$$

- For times $0 < t_1 < t_2 < \cdots < t_n$, the random variables $X_1 = W(t_1), X_2 = W(t_2) - W(t_1), \ldots, X_n = W(t_n) - W(t_{n-1})$ are independent.

The above definition implies that $E[W(t)] = 0$ and $E[W(t)^2] = t$. Moreover, suppose that $0 \leq s \leq t$, then

$$\begin{aligned} E[W(t)W(s)] &= E[(W(t) + W(s) - W(s))W(s)] \\ &= E[(W(t) - W(s))]E[W(s)] + E[W(s)^2] \\ &= E[W(s)^2] \\ &= s, \end{aligned} \tag{2.1.1}$$

where we used independence of $W(t) - W(s)$ and $W(s)$ for the second line. Applying the identity (2.1.1) we have

$$\begin{aligned} E[X_j^2] &= E[W(t_j)^2] + E[W(t_{j-1})^2] - 2E[W(t_j)W(t_{j-1})] \\ &= t_j + t_{j-1} - 2t_{j-1} \\ &= t_j - t_{j-1}. \end{aligned} \tag{2.1.2}$$

Formally, (2.1.2) implies that $E[dW^2] = dt$, indicating that the stochastic calculus differs from the standard calculus.

One can numerically simulate a Wiener process (Fig. 2.1.1) using its discrete time analog

$$W_{i+1} = W_i + \sqrt{h}N(0,1), \quad i = 0, \ldots, n,\ W_0 = 0, \tag{2.1.3}$$

where $N(0,1)$ is an independent sample from a normal distribution and h is the spacing between time points. Note that when simulating (2.1.3) numerically, the numbers obtained from $N(0,1)$ are generated as the output of an algorithm that requires the use of independent and uniformly distributed numbers as input. Two such algorithms for computing $N(0,1)$ numbers are known as the *Box-Muller* method (used by `XPPAUT` [45]) and the more efficient *ziggurat* method (used by `MATLAB` [46]). Of course, these methods rely on the statistical performance of pseudo-random number generators such as the *Mersenne Twister* generator.

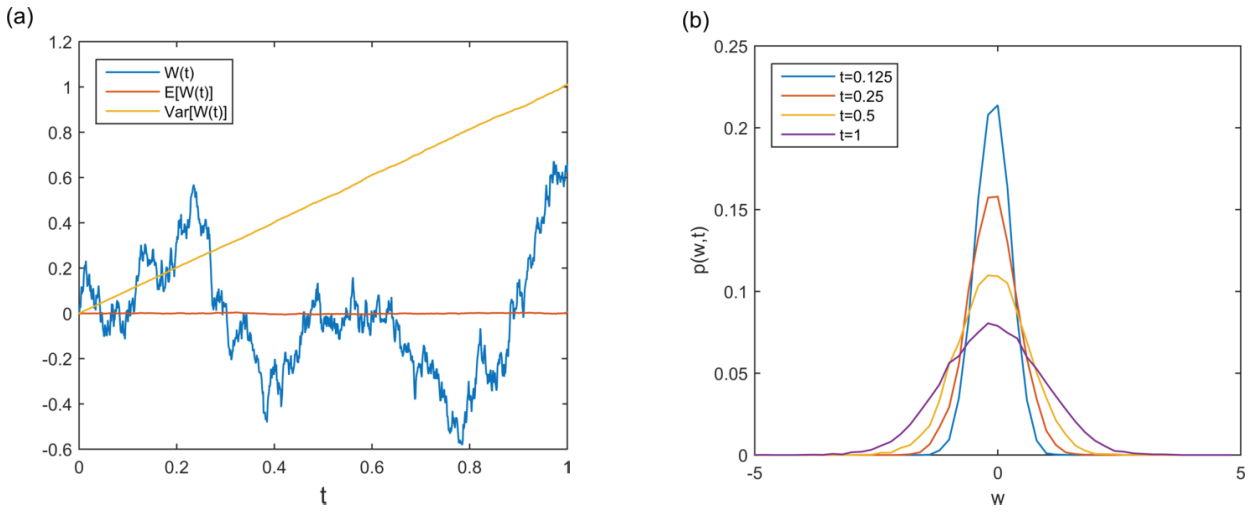

Figure 2.1.1: Graphs demonstrating the statistics of the simulated Wiener process. Equation (2.1.3) was simulated $N = 10\,000$ times on the interval $0 \leq t \leq 1$. (a) Sample path of $W(t)$ (*blue*) with expected value and variance of $W(t)$ for the N trials. (b) Histogram representing probability distribution function of $W(t)$ at the time points listed in the figure legend. Note the diffusive nature of the process.

Based on the properties of $W(t)$ we can now delineate the role of Wiener processes in defining the dynamics of SDEs. A formal, (yet non-rigorous) way of stating a one-dimensional SDE is

$$\frac{dx(t)}{dt} = a(x(t)) + b(x(t))\xi(t), \quad x(0) = x_0, \quad \xi(t) = \frac{dW}{dt}, \tag{2.1.4}$$

where W is the Wiener process defined above. The term $\xi(t)$ in (2.1.4) is commonly known as "white noise". One issue with (2.1.4) is that despite being continuous, the sample paths of $W(t)$ are nowhere differentiable, i.e., $\xi(t)$ doesn't exist. For this reason, the SDE (2.1.4) is more rigorously stated as

$$dx(t) = a(x(t))dt + b(x(t))dW(t), \quad x(0) = x_0. \tag{2.1.5}$$

We say that $x(t)$ is a solution to the SDE (2.1.5) if

$$x(t) = x_0 + \int_0^t a(x(s))ds + \int_0^t b(x(s))dW(s), \quad \text{for } t \geq 0. \tag{2.1.6}$$

The theory of SDEs requires that the last integral on the right-hand side of (2.1.6) is well-defined, which, as it turns out, can be achieved using Riemann sums. In other words, the

integral is defined as the limit of partial sums given by

$$S_n = \sum_{i=1}^{n} b(\tau_i)(W(t_i) - W(t_{i-1})). \tag{2.1.7}$$

In contrast to Riemann sums, however, the infinite limit of S_n depends on the point $t_{i-1} \leq \tau_i \leq t_i$. By taking $\tau_i = t_{i-1}$ in the infinite limit, one obtains the *Itô* integral, whereas taking $\tau_i = (t_i + t_{i-1})/2$ leads to the *Stratonovich* integral. Stochastic calculus has been developed using both the Itô and Stratonovich definitions, and the use of one or the other depends on mathematical and physical considerations that will not be explored here. Notice however, that when $b(x(t))$ is a constant (the *additive noise* case), the two integral definitions are equivalent.

We note in passing that the theory of SDEs is not restricted to one-dimensional systems and has been generalized for use in higher dimensional settings.

2.1.1 Ornstein-Uhlenbeck process

The Ornstein-Uhlenbeck (OU) process $\eta(t)$ is defined as a solution to the SDE

$$t_c d\eta(t) = -\eta(t)dt + \sqrt{2Dt_c}dW(t), \quad \eta(0) = \eta_0, \tag{2.1.8}$$

where t_c and D are parameters that determine that determine the correlation time and intensity of the noise respectively (see Eq. (2.1.12)). The solution to (2.1.8) is obtained using the method of variation of parameters, and given by

$$\eta(t) = \eta_0 e^{-\frac{t}{t_c}} + \sqrt{\frac{2D}{t_c}} \int_0^t e^{-\frac{(t-s)}{t_c}} dW(s), \quad t \geq 0. \tag{2.1.9}$$

From (2.1.9) we obtain the following statistical properties of $\eta(t)$:

$$E[\eta(t)] = n_0 e^{-\frac{t}{t_c}} \implies \lim_{t\to\infty} E[\eta(t)] = 0 \quad \text{(steady-state expectation), and} \tag{2.1.10}$$

$$\text{Var}[\eta(t)] = D(1 - e^{\frac{-2t}{t_c}}) \implies \lim_{t\to\infty} \text{Var}[\eta(t)] = D \quad \text{(steady-state variance).} \tag{2.1.11}$$

Another statistical quantity of interest that can be calculated from (2.1.8) is the *autocorrelation* function defined by $r(t) = E[\eta(t)\eta(s)]$, $0 \leq s \leq t$. In the long time limit ($s, t \gg 1$), the autocorrelation of $\eta(t)$ is given by

$$r(t) = D \exp[\frac{s-t}{t_c}], \tag{2.1.12}$$

which is the reason why $\eta(t)$ is known as "exponentially-correlated" noise.

2.1.2 Numerical methods for SDEs

Similar to mathematical models described by complex sets of ODEs, certain SDE models are studied most effectively using numerical techniques. The *Euler-Maruyama (EM) approximation* of (2.1.4) is a one-dimensional stochastic (Itô) process $X(t)$, $t \in [0, T]$ that satisfies the iterative equation

$$X_{n+1} = X_n + h_n a_n + b_n \Delta W_n, \quad X_0 = x_0 \tag{2.1.13}$$

for the discrete time points $0 = t_0 < t_1 < \cdots < t_n = T$, where $X_n = X(t_n)$, $h_n = t_{n+1} - t_n$, $a_n = a(X_n)$, $b_n = b(X_n)$, and $\Delta W_n = W(t_{n+1}) - W(t_n)$ are the random increments of the Wiener process $W(t)$. We assume an equally spaced grid so that $t_n = t_0 + nh$, i.e., $h_n = h$. The independent random increments ΔW_n are obtained using (2.1.3), which means that an algorithm for generating independent, normally distributed $N(0, 1)$ samples is required.

Based on the discussion above, it is now important to determine how well X_i approximates the true solution $x(t_i)$. Analogous to the definition of global truncation error for numerical solutions of ODEs, we define the error ϵ in SDEs as follows:

$$\epsilon = E[|X(T) - x(T)|],$$

i.e., the expectation of the absolute error in the approximation at time T. An approximation $X_h(t)$, where h denotes the step size, is said to *converge strongly with order* $\gamma > 0$ *at* T if there exists a constant C independent of h, and a $\bar{h} > 0$ such that

$$\epsilon(h) = E[|X_h(T) - x(T)|] \leq Ch^\gamma,$$

for all $h \in (0, \bar{h})$. It can be shown under some growth conditions on $a(x)$ and $b(x)$ that the EM approximation converges strongly with order $\gamma = 0.5$ uniformly on $[0, T]$. Moreover, in the case where $b(x) = b =$ constant, then the strong convergence order improves to $\gamma = 1$. It is important to point out that other approximation schemes may offer higher order convergence. For instance, the Milstein scheme, defined by the iterative equation

$$X_{n+1} = X_n + h_n a_n + b_n \Delta W_n + \frac{1}{2} b_n b_n' ((\Delta W_n)^2 - h), \quad X_0 = x_0, \tag{2.1.14}$$

has strong convergence order of $\gamma = 1$. The approximation schemes (2.1.13) and (2.1.14) are

derived through stochastic (Itô) Taylor expansions, and thus higher order schemes can be derived by taking more terms in the truncated Taylor expansion. The results of stochastic simulations in Chapter 4 were obtained using the EM scheme (typically with $h = 0.01$ms), which is reasonable since the system only contains additive noise terms.

2.2 Slow-fast subsystem analysis

In this section, we review a commonly-used technique for analyzing bursting in neuronal systems referred to as either *dissection of bursting* [47], *slow-fast subsystem analysis* [48], or *geometric singular perturbation (GSP) analysis* [49]. Although we use these terms interchangeably, the latter term is most appropriate since the technique involves using dynamical systems theory to study singularly perturbed systems, that is systems expressed in the form

$$\begin{aligned} \dot{x} &= f(x, y), \quad x(0) = a \\ \dot{y} &= \varepsilon g(x, y), \quad y(0) = b, \end{aligned} \tag{2.2.1}$$

where $x \in \mathbb{R}^n$, $y \in \mathbb{R}^m$, and $\varepsilon > 0$ is a small perturbation parameter. Neuronal models can often be expressed in the form (2.2.1) because of the relative timescales of the underlying biological mechanisms. For example, the processes responsible for action potential generation may operate on much faster timescales than those that regulate intracellular Ca^{2+} concentration. To motivate the discussion of slow-fast subsystem analysis, we will first review some relevant theory on quasistatic-state approximation (QSSA). Our overview of this topic is based on that of Hoppensteadt [50], which should be consulted for technical details.

2.2.1 Quasistatic-state approximations

One goal of the QSSA theory is to show that in some cases, solutions of the *reduced problem*

$$0 = f(x, y) \tag{2.2.2}$$

$$\dot{y} = \varepsilon g(x, y), \quad y(0) = b, \tag{2.2.3}$$

can converge to solutions of the *full system* (2.2.1). First, we assume that f and g are smooth, continuously differentiable functions. We seek solutions to the *slow subsystem,*

$$\dot{y_0} = \varepsilon g(\phi(y_0), y_0), \quad y_0(0) = b, \tag{2.2.4}$$

for which $x = \phi(y)$ is a unique smooth solution to (2.2.2). Now suppose that a solution $y_0(t)$ to (2.2.4) exists, and the manifold $\phi(y)$ is a surface of stable equilibrium points of the *fast subsystem*

$$\dot{x} = f(x; y), \tag{2.2.5}$$

where y is now treated as a vector of parameters. Denoting $x_0(t) = \phi(y_0(t))$, a corollary of the Quasistatic Manifold Theorem in [50] states that if $x(0)$ is within the domain of attraction of $\phi(b)$ in the fast subsystem, then, for ε sufficiently small there exists a solution $(x(t), y(t))$ of the system (2.2.4) on some interval $0 < t_0 \leq t \leq T$ that satisfies

$$x(t) = x_0(t) + o(1), \quad y(t) = y_0(t) + o(1), \tag{2.2.6}$$

uniformly as $\varepsilon \to 0^+$. More precisely, this result implies that at some time t after the initial time, for every $\delta > 0$ there exists an $r > 0$ such that $|(x, y) - (x_0, y_0)| < \delta$ whenever $0 < \varepsilon < r$. In other words, in the limit $\varepsilon \to 0^+$, the solution $x(t)$ of (2.2.1) converges to the trajectory $\phi(y_0(t))$ along the stable equilibrium manifold, where y_0 is the solution of (2.2.4). Furthermore, the solution $y(t)$ of (2.2.1) converges to the solution of the slow subsystem (SS).

The result leading to the equations in (2.2.6) is restrictive in that it requires $\phi(y)$ to be a smooth manifold of stable equilibrium points without folds for the relevant values of y. As mentioned in [50], the presence of a fold in $\phi(y)$ (perhaps due to bistability in fast subsystem) leads to complications in the analysis of singularly perturbed systems. Furthermore, the theory above makes no mention of periodicity in the fast subsystem. Therefore, it does not apply to the active phase of bursting, where the fast subsystem has periodic spiking solutions for values of y that are solutions of the full model. Despite these limitations, advances in slow-fast subsystem analysis have allowed researchers to obtain rigorous results concerning the existence of periodic bursting solutions, as discussed in the next section.

2.2.2 GSP examples

The first step in the slow-fast subsystem analysis of a bursting model is to identify which parameters lead to a separation of time scales in the model so that the full model can be decomposed into fast and slow subsystems (as described by (2.2.4) and (2.2.5)). Ideally, the second step of the analysis is to use the dynamical properties of the fast and slow subsystems to prove the existence of periodic bursting solutions for ε sufficiently small. For example, Lee and Terman [51] show the existence of "square-wave" periodic bursting solutions for certain 3-dimensional systems with two fast variables and one slow variable. They do so

by constructing a contracting Poincaré map that is a composition of maps, with each map corresponding to the passage of the trajectory along a neighbourhood of the fixed point or periodic solution manifolds of the fast subsystem (FS). The proof is complicated by the presence of a homoclinic orbit in the fast subsystem, which leads to values of ε for which the period bursting solution is not uniquely determined. Rigorous existence results have also been obtained for "parabolic" bursting [52], where it was shown that a general class of systems that have slow and fast subsystems satisfying certain geometric assumptions, are dynamically equivalent to a class of systems that possess parabolic bursting solutions [53]. Although the results in [52, 51] are quite general, the hypotheses of the theorems may be difficult to verify analytically for a given model, and so numerical verification is required. In some cases, the justification for the existence of bursting solutions is heuristic [54, 49], meaning that solutions are assumed to exist based on (i) geometric arguments in the phase plane, and (ii) numerical simulations demonstrating that bursting solutions follow a trajectory within a small neighbourhood of the fast subsystem manifolds. The value of the heuristic approach is that the bursting model under investigation can be classified by the two types of bifurcations crossed in the FS, which correspond to the initiation and termination of spiking in the bursting solution of the full model [48]. The classification can then be used to study the dynamics observed in the full model based on a canonical model that is more tractable analytically, as we will demonstrate in Section 4.3.

In order to demonstrate the effectiveness of slow-fast subsystem analysis in deciphering the dynamics of bursting models, we study the Chay-Cook model for bursting in pancreatic β-cells [55]. The slow-fast subsystem analysis of this model was first carried out in the seminal work by Bertram et al. [54]. The Chay-Cook model is a Hodgkin-Huxley-like model given by the set of equations

$$\begin{aligned} C_m\frac{dv}{dt} &= -[I_{Ca}(v,s) + g_K n(v-V_K) + g_L(v-V_L)] \\ \frac{dn}{dt} &= \lambda\frac{n_\infty(v)-n}{\tau_n(V)} \\ \frac{ds}{dt} &= \frac{s_\infty(v,c)-s}{\tau_s(v,c)} \\ \frac{dc}{dt} &= f[-\alpha I_{Ca}(v,s) - k_c c], \end{aligned} \tag{2.2.7}$$

where

$$
\begin{aligned}
s_\infty(v) &= [1+\exp(2A(v,c))]^{-1}, \quad A(v,c) = (V_s + S_s\log(c) - v)/2S_s \\
\tau_s(v,c) &= \bar{\tau}_s[2\cosh(A(v,c))]^{-1} \\
x_\infty(v) &= [1+\exp((V_x - v)/S_x)]^{-1}, \quad x \in \{m,n\} \\
\tau_n &= \bar{\tau}_n[1+\exp((v-V_n)/S_n)]^{-1} \\
I_{Ca}(v,s) &= (g_I m_\infty(v) + g_s s)(v - V_{Ca}).
\end{aligned}
$$

The parameters values chosen for the analysis are those for the "Type II" bursting example in [54]. When integrated numerically, system (2.2.7) exhibits parabolic bursting behaviour; that is, the graph of $v(t)$ shows slow oscillations that underlie clusters of spikes with low frequency at the start and end of the burst, and high frequency near the middle of the burst. The value of $\bar{\tau}_s$ is taken to be large and f small to create a separation of timescales in the system. As a result, the two-dimensional FS consists of the equations for $\dot{v}$ and $\dot{n}$ (with the gating variable s and the intracellular Ca^{2+} concentration c treated as parameters), whereas the two-dimensional SS consists of the equations for $\dot{c}$ and $\dot{s}$ with the fast variables assumed to be at equilibrium (as functions of c and s). Now, in the case of a sufficiently large separation of timescales, we expect the bursting trajectory of the full model to correspond to a cycle along the equilibrium and periodic solution manifolds of FS, as determined by the SS. Using `AUTO` [56], we can plot a projection in the $s-v$ plane of the "s"-shaped equilibrium manifold $\phi(s,c)$ as well as the branch of periodic solutions of FS. In other words, we can compute the one-parameter bifurcation diagram of FS with respect to the "parameter" s (one of the slow variables that is treated as a constant), and plot the periodic solutions extending from any Hopf bifurcation points that are found numerically. Note that the projection of $\phi(s,c)$ remains static in the $s-v$ plane because the FS does not depend explicitly on the slow variable c. If we superimpose the bursting solution in the (s,v) plane onto the one-parameter bifurcation diagram, as shown in Figure 2.2.1, we can then observe how trajectories traverse the branches of fixed points and periodic solutions of the FS. The s-nullcline ($s = s_\infty(v;c)$) at the minimum and maximum values of c (c_{min}, c_{max}) obtained in the bursting solution are also superimposed in Figure 2.2.1 to indicate the direction of the flow in the $s-V$ plane. With these numerical results, we can now heuristically justify that a burst cycle in the full model corresponds to a trajectory along the stable and periodic manifolds of the FS, as suggested by Figure 2.2.1.

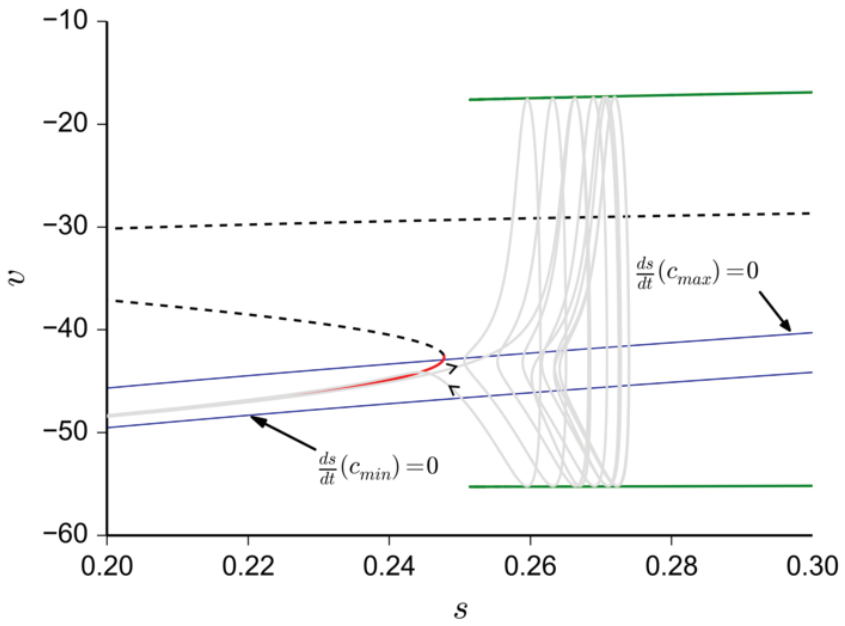

Figure 2.2.1: Graphical representation of the slow-fast subsystem analysis for the Type II burster: Chay-Cook model (2.2.7). The bifurcation structure for the FS has branches of (i) stable (*red*) and unstable (*black*) fixed points, and (ii) maximum and minimum values of periodic solutions (*green*). The projection of the full model solution (*grey*) in the $s-v$ plane, and the s-nullclines (*blue*) at c_{min} and c_{max} are superimposed on the one-parameter bifurcation diagram of the FS. Notice that this model does not possess bistability and that the full model trajectory remains within a small neighbourhood of the branches of the bifurcation structure for the entire cycle.

To begin our analysis, let us suppose that the initial condition of the full model is taken so that it lies in the basin of attraction of the stable equilibrium of the FS, above the slow s-nullcline where $\dot{s} > 0$. Then the trajectory will quickly relax towards the lower stable branch of the FS manifold, and move along it rightward since $\dot{s} > 0$. This behaviour continues (as long as the s-nullcline lies below the stable manifold) until the trajectory passes the fold and enters the parameter regime where FS has a single unstable equilibrium coexisting with a stable limit cycle. For the set of fast subsystem parameters generating "Type II" bursting, the fold occurs at a codimension-one saddle-node on invariant circle (SNIC) bifurcation, i.e., where a saddle-node and homoclinic bifurcation occur simultaneously (see Fig. 2.2.2 for a schematic of this bifurcation).

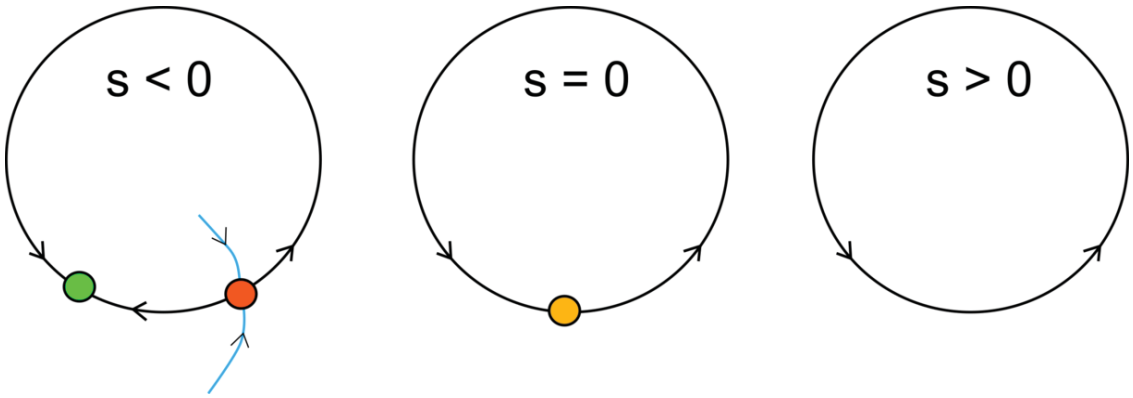

Figure 2.2.2: Schematic diagrams showing the transition through a SNIC bifurcation in a planar system for hypothetical parameter s. For $s < 0$, the system has a saddle (*red*) and a stable (*green*) equilibrium. The stable manifold (*blue*) of the saddle separates a pair of heteroclinic orbits, connecting the stable manifold of the stable equilibrium with the unstable manifold of the saddle point. The SNIC bifurcation occurs at $s = 0$ where a homoclinic orbit coincides with the center manifold of the saddle-node. A stable limit cycle persists for $s > 0$. See [57] for more details.

Within the parameter regime that supports periodic spiking in the FS, the lateral movement of the burst trajectory relative to the fold is determined by the magnitude of $\dot{s}$ and the time that the trajectory spends above and below the nullclines. To see this, notice that during spiking the full model trajectory will repeatedly cross the s-nullcline (whose position in the $s - v$ plane is c-dependent). At the start of the burst, the trajectory spends long periods of time above the s-nullcline, and so one expects a net movement to the right. As the burst progresses, the s-nullcline moves upward (due to an increase in c induced by Ca^{2+} entry into the cell during spiking), increasing the time the trajectory spends below the nullcline. As a result, the trajectory moves back towards the SNIC, eventually crossing it to terminate the burst. After the SNIC is crossed, c begins to decrease (due to Ca^{2+} efflux from the cytosol), shifting the s-nullcline downward. The trajectory continues leftwards along the stable branch as long as the s-nullcline lies above it. The cycle begins anew once the s-nullcline falls back below the stable branch. The position of the trajectory relative to the fold also gives rise to the characteristic "parabolic" profile in spike frequency that is observed within the burst. This phenomenon is explained by the fact that the period of stable limit cycles monotonically approaches infinity as the parameter s approaches the homoclinic bifurcation. Therefore, at the furthest point of the trajectory from the homoclinic, the spike frequency is the highest, while at the start and end of the burst, it is the lowest.

In describing the path of the trajectory in the $s - v$ plane, we required that the $s-$nullcline move in a specific manner as a function of c in order to generate parabolic bursting. Ultimately, this corresponds to a certain configuration of the s- and c-nullsurfaces, given

by $s = s_\infty(v, c)$ and $c = -\frac{\alpha}{k_c} I_{Ca}(v, s)$. One could use the nullsurfaces to justify the existence of bursting solutions in a manner analogous to that of "Type I" bursting in [54], where the slow subsystem is only one-dimensional. Another approach is to analyze the slow subsystem in the two-dimensional phase plane. The basis of this method is to obtain the nullclines of the slow subsystem during the quiescent phase of the burst by using the quasistatic state assumption, and in the active phase by using formal averaging. Using the properties of the nullclines, one can justify the existence of a periodic solution that crosses (for example) the curve of homoclinic bifurcations in the FS, which corresponds to entry or exit from the spiking regime in the FS. Such an approach was used by Smolen et al. [58] in the study of a bursting model with a two-variable SS. For the Chay-Cook model that we presented in this section, we would thus analyze the following systems in the phase plane:

$$\begin{aligned} \dot{c} &= -f[\alpha I_{Ca}(v_\infty(s), s) + k_c c] \\ \dot{s} &= \frac{s_\infty(v_\infty(s), c) - s}{\tau_s(v_\infty(s), c)} \end{aligned} \qquad \text{(quasistatic state assumption), and} \tag{2.2.8}$$

$$\begin{aligned} \dot{\bar{c}} &= -\frac{f}{T(\bar{s})} \int_0^{T(\bar{s})} (\alpha I_{Ca}(v(t, \bar{s}), \bar{s}) + k_c \bar{c})\, dt \\ \dot{\bar{s}} &= \frac{1}{T(\bar{s})} \int_0^{T(\bar{s})} \frac{s_\infty(v(t, \bar{s}), \bar{c}) - \bar{s}}{\tau_s(v(t, \bar{s}), \bar{c})}\, dt, \end{aligned} \qquad \text{(formal averaging)} \tag{2.2.9}$$

where in (2.2.8) $v_\infty(s)$ is the steady solution of the FS, and $T(s)$ in (2.2.9) is the period of the spiking solution $v(t, s)$ of the FS. Note that we can interpret (2.2.8) as "the SS restricted to the manifold of fixed points of the FS".

As a final example, consider the phase plane analysis depicted in Fig. 2.2.3 of a parabolic bursting model by Baer et al. [59]. Using equations analogous to (2.2.8) and (2.2.9), the authors of [59] computed the nullclines of the SS restricted to the equilibrium of the FS (labeled $\dot{x} = 0$ and $\dot{Ca} = 0$ in Fig. 2.2.3) and the nullclines of the formally averaged SS (labeled $\dot{x}_{av} = 0$ and $\dot{Ca}_{av} = 0$ in Fig. 2.2.3). Figure 2.2.3 indicates that the projection of the full model trajectory in the $Ca - x$ plane is well-approximated by a piecewise defined system consisting of two parts. The first part, corresponding to the quiescent phase of the burst, has the form of (2.2.8) and is defined in the region below the curve of homoclinic (HC) bifurcations in the fast system. The second part, corresponding to the active phase of the burst, has the form of (2.2.9) and is defined above the HC curve. To see why the full model trajectory is well-approximated by a periodic solution of such a system, notice that in the regions below and above the HC curve, the trajectory always crosses the nullclines horizontally or vertically.

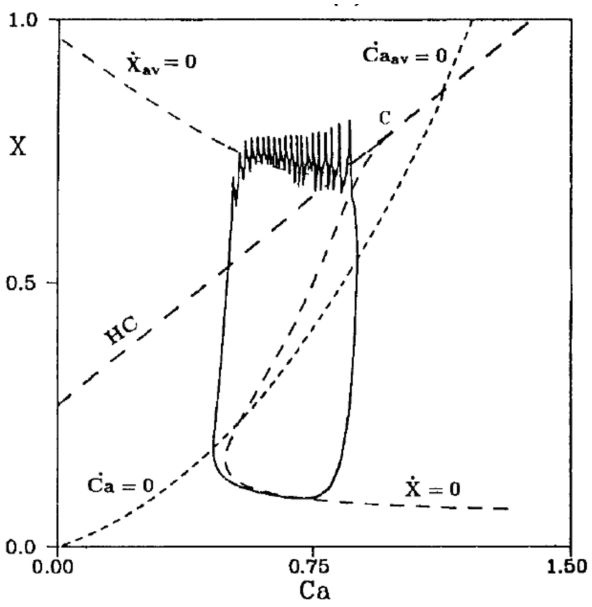

Figure 2.2.3: Graphical representation of slow subsystem phase plane analysis as carried out by Baer et al. [59] for a parabolic bursting model. The nullclines (*short dashes*) $\dot{x} = 0$, $\dot{Ca} = 0$, and $\dot{x}_{av} = 0$, $\dot{Ca}_{av} = 0$ are plotted against the projection of the full model solution in the $Ca - x$ plane (*solid*). The full model trajectory passes through a curve of homoclinic (HC) bifurcations of the fast subsystem (*long dashes*). The point labeled "C" denotes a cusp that forms at the intersection of the x- and x_{av}- nullclines with the HC curve. A similar cusp also exists for the c- and c_{av}-nullclines but it is not visible at this resolution. Figure used with permission.

With this mathematical background, we are now ready to introduce and analyze the GnRH neuron model.

Chapter 3

Model development

3.1 Formalism

To model the intrinsic electrical activity of GnRH neurons, a Hodgkin-Huxley-like (HH) formalism was used [32]. We say "Hodgkin-Huxley-like" because the original HH model has been modified to include additional ionic currents, to incorporate a submodel for intracellular Ca^{2+} concentration, and to use a different description for the Na^{+} current responsible for the generation of action potentials. The dynamical equations governing HH models are derived from basic electromagnetic theory by modelling the cell as an RC-circuit, where the cell-membrane acts as a capacitor in parallel with voltage/Ca^{2+}-dependent ion channels (which in turn behave as resistors in parallel). Each resistor corresponds to one of several ion channel species that are distinguishable from each other by their permeability to specific ions and their protein structure. Due to differences in ionic concentrations between the inside and outside of the cell, electrochemical gradients emerge for each type of ion species resulting in a movement of charges through these channels. In the circuit model, the gradient is the source of an electromotive force that is placed in series with each resistor. To illustrate the types of ion channels expressed on GnRH neurons and to emphasize the theory underlying Hodgkin-Huxley models, a circuit diagram for the GnRH neuron model is provided in Figure 3.1.1. Notice that all conductances, except for that of the leak current, I_L, are variable due to voltage- and Ca^{2+}-dependent permeability of ion channels.

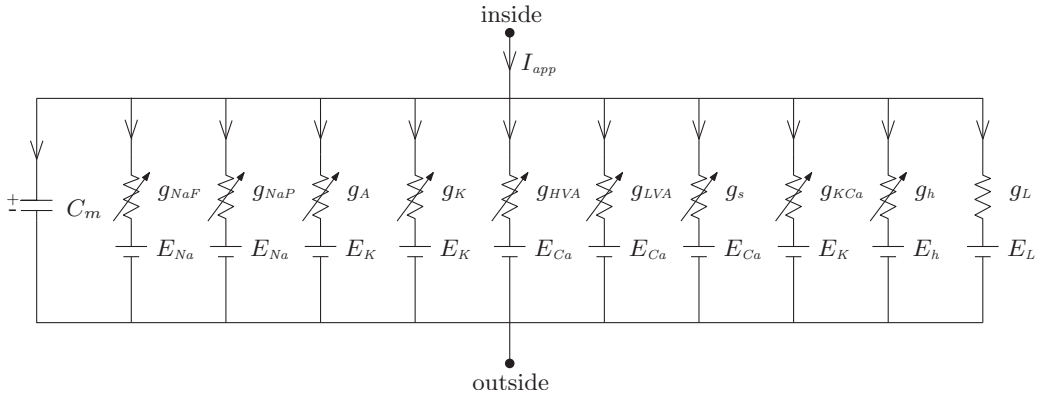

Figure 3.1.1: Circuit diagram illustrating the various ionic currents that are part of the GnRH neuron model.

In Figure 3.1.1 the membrane potential is defined by $V = V_{in} - V_{out}$, the difference in potential between the intracellular and extracellular regions. We use the standard convention that flux of positive ions into the cell corresponds to a negative current, and that current applied to the inside of the cell is positive. Whether ions of type j leave or enter the cell is determined by the sign of the so-called *driving force* $V - E_j$, where E_j is the Nernst or *reversal* potential for ion j. The reversal potential E_j is given by the equation

$$E_j = \frac{RT}{zF} \ln\left(\frac{[j]_o}{[j]_i}\right),$$

where $[j]_o$ and $[j]_i$ are the extracellular and cytosolic concentrations respectively of ion j. The values of the reversal potentials are constants since it is assumed that the concentration gradients of ions are actively maintained by the cell via ion pumps and exchangers. The amount of flux of ion j, otherwise known as ionic current, is denoted by I_j and is given by the equation

$$I_j = g_j(t, V, Ca)(V - E_j), \tag{3.1.1}$$

where g_j is the time-, voltage-, and Ca^{2+}-dependent conductance (inverse of resistance). Equation (3.1.1) can be derived using Kirchoff voltage law applied to the individual RC-loops in the circuit. It is also important to note that g_j is determined by the collective action of all ion channels of type j acting in parallel. In this context, it is then appropriate to refer to (3.1.1) as the *macroscopic* current equation. From this point forward, it is assumed that the units of the quantities introduced in (3.1.1) are $[g_j] = \text{nS}$, $[V] = \text{mV}$, so that $[I_j] = \text{pA}$.

Applying Kirchoff's current law for the circuit in Figure 3.1.1, we obtain the dynamical

equation for the membrane potential V,

$$C_m \frac{dV}{dt} = -(I_{NaF} + I_{NaP} + I_A + I_K + I_{HVA} + I_{LVA} + I_s + I_h + I_{KCa} + I_L) + I_{app} + \eta(t), \quad (3.1.2)$$

where C_m is the membrane capacitance, I_{app} represents an external stimulus applied to the system, and $\eta(t)$ is a stochastic variable that accounts for intrinsic noise within the system. For the present modelling study, I_{app} is usually zero since we seek to model intrinsic electrical activity; however, the simulation of applied current is still useful as a means of model verification. The dynamics of the stochastic variable $\eta(t)$ are determined by an OU process as defined by (2.1.8). Descriptions of all ionic currents appearing in (3.1.2), except for the slow inward Ca^{2+} current I_s and the leak current I_L, are provided in Table 1.1. The currents I_s and I_L are excluded from Table 1.1 because there are no published studies on these currents for GnRH neurons. We refer the reader to [14, 60] for a description of these currents in other cells. In (3.1.2), the voltage-gated currents are I_{NaF}, I_{NaP}, I_A, I_K, I_{HVA}, I_{LVA}, I_s, and I_h, whereas I_{KCa} is Ca^{2+}-gated. For the voltage-gated currents (except I_{NaF}), we have

$$I = gm^p h(V - E), \quad (3.1.3)$$

where m and h are dynamical variables that represent the proportion of open m-subunits and h-subunits in the ion channel population and g is the maximum conductance parameter. The term *subunit* refers to a component of an individual ion channel that undergoes conformational changes to allow the channel to open. Intuitively, m and h can be thought of as "activation" and "inactivation" gating variables respectively. The parameter p represents the number of independent activation subunits assumed to be present in individual ion channels. It follows that the product $m^p h$ is the proportion of ion channels in the membrane that are conducting or "open". The dynamical equations for m and h are given by

$$h = \sum_{i=1}^{n} f_i h_i, \quad 0 \leq f_i \leq 1, \quad \sum_{i=1}^{n} f_i = 1 \quad (3.1.4)$$

$$\dot{m} = \frac{m_\infty(V) - m}{\tau_m(V)} \quad (3.1.5)$$

$$\dot{h_i} = \frac{h_\infty(V) - h_i}{\tau_{h_i}(V)} \quad (3.1.6)$$

$$x_\infty(V) = \frac{1}{1 + \exp[(V - V_h)/k]}, \quad x = m, h. \quad (3.1.7)$$

Notice that the equation for h is composed of a weighted sum of n dynamical variables satisfying (3.1.6) to account for currents that inactivate on multiple (n) time scales, and

$$C \underset{\beta(V)}{\overset{\alpha(V)}{\rightleftarrows}} O \tag{3.1.11}$$

Figure 3.1.2: Simple (in)activation scheme for independent ion channel subunits

that $h_\infty(V)$ is identical for all h_i. Equations (3.1.5) and (3.1.6) can be derived employing a chemical kinetic approach applied to the simple configuration shown in Figure 3.1.2 and defining $x_\infty(V) = \frac{\alpha(V)}{\alpha(V)+\beta(V)}$, $\tau(V) = \frac{1}{\alpha(V)+\beta(V)}$. Equation (3.1.7) can be derived by using the notion of Gibbs free energy, and assuming a linear thermodynamic model for free energy [61] (i.e. by assuming an exponential form for the voltage-dependent transition rates, $\alpha(V)$, $\beta(V)$ between open and closed subunit states). The Boltzmann-like curve (3.1.7) is also a reasonable model for other voltage dependent rates whose functional forms satisfy certain criteria (see Section 3.2.3). The voltage-dependent time constants $\tau(V)$, on the other hand, can assume one of three functional forms:

$$\tau = \text{constant} \tag{3.1.8}$$

$$\tau_1(V) = d + c\exp[-\frac{(V-a)^2}{b}] \tag{3.1.9}$$

$$\tau_2(V) = e[\exp(\frac{a+V}{b}) + \exp(\frac{c+V}{d})]^{-1} + f. \tag{3.1.10}$$

The function $\tau_1(V)$ is symmetric about the maximizing point $V = a$ while $\tau_2(V)$ can be skewed about its maximizing point for certain values of the parameters. The use of such voltage-dependent time constants is standard in the neuronal modeling literature [62, 48, 35].

As mentioned previously, the current I_{NaF} does not follow the formalism of (3.1.4)-(3.1.7). Details on the modelling of I_{NaF} are provided in Section 3.3, but for now, we state the macroscopic current equation given by

$$I_{NaF} = g_{NaF}O^3(V - E_{Na}),$$

where O is the proportion of open Na^+ channels whose dynamics are governed by the Markov model depicted in Figure 3.1.3.

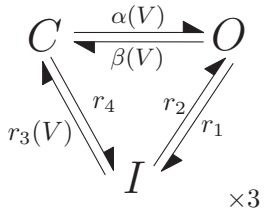

Figure 3.1.3: Three-state Markov model used to describe I_{NaF}. Details on this model can be found in [63].

We now introduce the Ca^{2+}-dependent equations appearing in the model. The dynamics of intracellular Ca^{2+} concentration, denoted by Ca, are described by the following ODE model:

$$\begin{aligned} \frac{dCa}{dt} &= f(-\alpha I_{Ca} - k_p \frac{Ca^2}{K_p^2 + Ca^2}) \\ I_{Ca} &= I_{LVA} + I_{HVA} + I_s \\ \alpha &= \frac{\beta}{2FV_{cyt}}, \end{aligned} \tag{3.1.12}$$

which is a simplification of a more detailed Ca^{2+} subsystem used in previous GnRH neuron models [34, 1]. An important feature of the present Ca^{2+} submodel (3.1.12) is that it prevents the accumulation of Ca^{2+} in the cell that enters through voltage-gated Ca^{2+} channels. The Ca-dependent saturating term on the right-hand side accounts for removal of intracellular Ca^{2+} via membrane-bound pumps and/or exchangers. The parameter f represents the fraction of free (unbound) Ca^{2+} in the cytosol. The term α is a factor that converts the flux I_{Ca} into concentration of Ca^{2+} in units of μM. In the equation for α, F is Faraday's constant, V_{cyt} is the volume of the cytosolic compartment, β is a molar to micromolar conversion factor, and the factor 2 represents the valency of the calcium cation. The variable Ca enters the voltage equation through the Ca^{2+}-dependent K^+ current I_{KCa}, which represents the current conducted by SK channels and has the form

$$I_{KCa} = g_{KCa} \frac{Ca^2}{K^2 + Ca^2}(V - E_K). \tag{3.1.13}$$

In the equation for I_{KCa}, the Ca-dependent term represents instantaneous activation of the SK channel through an indirect binding mechanism involving intracellular Ca^{2+} and the cytoplasmic protein calmodulin [64].

All values of the parameters appearing in this section can be found in Section A.2. Unless otherwise noted, different intrinsic electrical states are simulated by the model through changes in the maximum conductance parameters, without changes to the kinetic

parameters. For visual reference, plots of the voltage-dependent time constants and steady-state (in)activation curves are provided in Section A.3.

3.1.1 Model assumptions

The use of a (stochastic) HH model makes implicit assumptions about the properties of the cell. Assumptions of the present model are listed here.

- The cell is an ideal spherical capacitor with an isopotential somatic compartment. Consequently dendritic contributions to the membrane potential are not considered.
- The included ionic currents account for all ionic flux into and out of the soma.
- In the context of Ca^{2+} handling, the intracellular region is comprised of a single compartment that is well mixed, i.e. intracellular Ca^{2+} concentration is homogeneous.
- The linear driving force approximation (rather than the full Goldman-Hodgkin-Katz (GHK) equation) is adequate for modeling excitability. This assumption was shown to be valid in a study of the original Hodgkin-Huxley equations [65].
- Stochastic fluctuations in membrane potential are the result of variability in one or more slow processes within the neuron. These processes may include (in)activation of ion channels with large time constants or intracellular Ca^{2+} handling.

An additional note is warranted for the assumption involving the GHK equation. Although we stated that the linear driving force or "Ohm" approximation is valid in the original HH model [65], the HH model does not include voltage-gated Ca^{2+} currents. In a typical mammalian neuron, $[Ca^{2+}]_i$ is small (0.1 μM) relative to the concentrations of other ions in the cell, for example $[Na^+]_i$ (5×10^3 μM) and $[K^+]_i$ (140×10^3 μM) [66]. For this reason, the influx of Ca^{2+} through voltage-gated channels can cause a large relative increase in $[Ca^{2+}]_i$, in which case it may be more appropriate to use the GHK current equation for modelling Ca^{2+} current [67]. The resulting current equation would then be

$$I_{Ca} = \bar{p} m^p h \, \frac{V(2F)^2}{RT} \, \frac{Ca_e \exp[-\frac{2FV}{RT}] - Ca}{1 - \exp[-\frac{2FV}{RT}]}, \tag{3.1.14}$$

where $\bar{p}$ is the maximum permeability of the ion channel, V is the membrane potential, Ca_e is the extracellular Ca^{2+} concentration (often taken to be a constant equal to $1.0 - 2.0\,\mu$M [66, 67]), Ca is the intracellular Ca^{2+} concentration as defined above, and R, T, F are the

standard thermodynamic quantities. The use of (3.1.14) could be used in place of (3.1.3) for the voltage-gated Ca^{2+} currents I_{LVA}, I_{HVA}, and I_s that appear in (3.1.2). However for simplicity, we retain the Ohmic form of these currents—a standard assumption in the field of computational neuroscience (e.g., see [35, 28] and many others) .

3.2 Modelling of ionic currents

3.2.1 Parameter estimation for ionic currents

Models describing the electrical activities of neurons grow increasingly complex when one seeks a complete biophysical description of these activities. This typically results from the inclusion of many ionic current submodels. For example, a single current modelled using the HH-formalism that has one time constant of inactivation can introduce two variables and thirteen parameters into the model. This is unavoidable if the purpose of the model is to make realistic predictions about the contributions of individual ionic currents to the overall electrical activity of the neuron. Fortunately, the rapid advance in electrophysiological recording techniques has made accurate parameter estimation an achievable endeavour. The type of data that are useful to conduct such parameter estimations include the time series data obtained from current- and voltage-clamp experiments. In the current-clamp setting, the experimenter records the membrane potential of the cell over a given period of time to gain information about the contribution of all conducting ion channels. It is in this recording mode that one might observe phenomena such as bursting, spiking, or simply a neuron in the resting state. In the voltage-clamp mode, the membrane potential is fixed at certain value, known as the *command potential*, through a feedback circuit so that $\frac{dV}{dt} = 0$ [14]. The feedback current required to maintain this condition is in turn a measure of the ionic current being conducted at the command potential. Data from voltage-clamp recordings is useful for parameter estimation in neuronal models because most currents are assumed to be strictly voltage-dependent. For instance, if it is assumed that the HH formalism is adequate for describing ionic currents, then the ODEs governing the dynamics of the gating variables can be solved for exactly when voltage is fixed. For an HH gating variable given by (3.1.5) or (3.1.6), we have

$$x(t) = x_\infty(V) + (x(t_0) - x_\infty(V))e^{-\frac{(t-t_0)}{\tau(V)}}, \tag{3.2.1}$$

where V is a constant and t_0 is the initial time. Although many currents can be active during voltage-clamp experiments (leading to many equations of the form (3.2.1)), pharmacological agents can be employed to isolate individual ionic currents. For example, the so-called "h-

current", denoted I_h in the present model, is sensitive to the pharmacological agent ZD7288 [20]. Assuming that a sufficiently high dose of ZD7288 is fully effective at blocking I_h, two voltage-clamp experiments with the same voltage-protocols can be performed to extract the contribution of I_h by subtraction. Now suppose that a voltage clamp experiment has been performed with the assumption that the measured current is attributable to a single species of ion channel. Assuming that the current is well described by (3.1.3), the time-dependent current equation for the ion channel is given by

$$I(t) = g[m(t)]^p \sum_{i=1}^{n} f_i h_i(t)(V - E), \tag{3.2.2}$$

where m and h have the closed-form solution (3.2.1). The advantage of closed-form solutions for the current is two-fold. First, it eliminates any error incurred by solving the gating differential equations numerically, and second, an efficient least squares-based method can be implemented to estimate all the parameters appearing in (3.2.2). The latter concept was originally developed by Willms et al. [68] and is called the *full-trace fitting method.* Details on this method are provided in Section 3.2.3. In the following subsection we introduce the voltage protocols employed by electrophysiologists to obtain the data required for the full-trace method, and also describe an alternative method of estimating the kinetic parameters, specifically those appearing in (3.1.5) and (3.1.6).

3.2.2 Voltage protocols

Voltage-clamp recordings are useful for quantifying the (in)activation kinetics of a particular species of ion channel. Using the voltage-clamp data, empirical functions describing the steady-state (in)activation curves $x_\infty(V)$ and time constants $\tau(V)$ can be determined. Although by definition, voltage-clamp means to maintain a constant membrane potential, some kind of transient response needs to be evoked during a voltage-clamp experiment in order to quantify the kinetics of a particular current. Step protocols, where the command voltage undergoes a series of steps to different values, are most frequently used to reveal the kinetic properties of ionic currents. Table 3.1 summarizes two common step protocols used for this purpose.

To determine how the steady-state activation and time-constant curves are obtained using the protocol described in Table 3.1a, we make some simplifying assumptions:

Assumption 1. *i. The evoked ionic current is adequately described by (3.2.2).*

Protocol (Voltage vs. time)	Description
a) 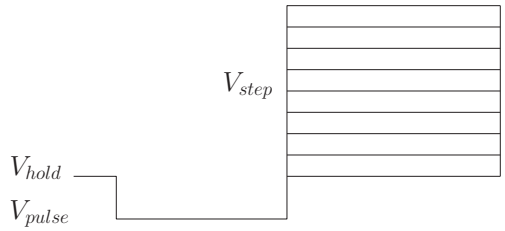	A sufficiently long hyperpolarized pre-pulse is used so that $x \to x_\infty(V_{pulse})$, where $x = m, h$. The step voltage V_{step} is varied. Time constants of (in)activation and steady-state activation at the discrete values of V_{step} can be inferred from this data.
b) 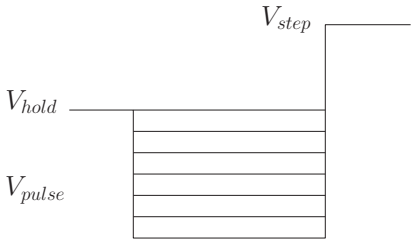	In contrast to protocol a), the *pre-pulse* step potential V_{pulse} is varied while V_{step} remains constant. Steady state inactivation at the discrete values of V_{pulse} can be inferred from this data.

Table 3.1: Summary of voltage-clamp protocols used to determine kinetics properties of ion channels

ii. The ion channels conducting the current are at a steady state at the end of the pre-pulse and are completely deactivated, i.e., $h = h_\infty(V_{pulse}) = 1$ *and* $m = m_\infty(V_{pulse}) = 0$.

iii. The rate of inactivation is slow relative to the rate of activation. That is, no inactivation occurs within the time required to reach peak activation.

By the assumptions above, the value of the steady-state activation curve at a given step voltage V_{step} is obtained through the ratio

$$\frac{I(V_{step})(V_{max} - E)}{I_{max}(V_{step} - E)} = \frac{g[m_\infty(V_{step})]^p}{g} = [m_\infty(V_{step})]^p, \tag{3.2.3}$$

where it is assumed that $I_{max} = \max_{V \in \mathbb{R}}\{I(V)\}$. The values of $I(V_{step})$ are obtained from the measurement of peak current during the voltage step. The calculated values of m_∞ at the various step potentials are then employed to fit to a continuous sigmoidal function raised to some unknown power p. The fitting yields the parameter values associated with the sigmoidal function (including p) so that $m_\infty(V)$ can be used within a continuous ODE model. Next, we show how the time constants of activation can be determined using the protocol in Table 3.1a. Remark that during the activation transient,

$$I(t) = g[m_\infty(V_{step})(1 - e^{-\frac{t}{\tau(V_{step})}})]^p(V_{step} - E). \tag{3.2.4}$$

Thus it is possible for the experimenter to fit the transient current data to the function

$f(t) = A(1 - e^{-\frac{t}{\tau}})^p$, where A, τ are treated as fitting parameters, and the value of p is that obtained from the activation curve fitting. A second fitting must be performed to convert the discrete values of τ at the step potentials into a continuous function, which often has a bell-shaped profile. Finally, the same voltage-step protocol can be used to obtain the time constants of inactivation, assuming that the process of inactivation begins once the current has reached its peak value during the voltage step. Under this assumption, the current equation at some time t after the peak time is given by

$$I(t) = gm_\infty(V_{step})^p \sum_{i=1}^{n} f_i[h_\infty(V_{step}) + (1 - h_\infty(V_{step}))e^{-\frac{t}{\tau_i(V_{step})}}](V_{step} - E), \tag{3.2.5}$$

where we have substituted $m(t) = m_\infty(V_{step})$, and $h(t) = h_\infty(V_{step}) + (1 - h_\infty(V_{step}))e^{-\frac{t}{\tau_i(V_{step})}}$ into (3.2.2). Expanding (3.2.5), we find that $I(t)$ has the functional form $f(t) = \sum_{i=1}^{n} A_i e^{-\frac{t}{\tau_i}} + B$. Once again, $f(t)$ is fit to the current data to obtain the parameters A_i, B, and τ_i, and a continuous function $\tau_i(V)$ is obtained by a secondary fitting procedure. The fraction of channels with inactivation type i (denoted by f_i) can be obtained using the values of A_i because

$$f_i = \frac{A_i}{\sum_{k=1}^{n} A_k}.$$

We remark, however, that there is an estimated value of f_i corresponding to each voltage-step, and therefore f_i is not uniquely determined from this procedure.

The remaining kinetic information that can be extracted from the voltage-clamp data is the steady-state inactivation curve. To obtain this curve, protocol b) of Table 3.1 is often used. Using a similar set of assumptions as in case a), the value of the steady-state inactivation curve at a given pulse voltage V_{pulse} is obtained through the ratio

$$\frac{I(V_{pulse})}{I_{max}} = \frac{g[m_\infty(V_{step})]^p h_\infty(V_{pulse})(V_{step} - E)}{g[m_\infty(V_{step})]^p (V_{step} - E)} = h_\infty(V_{pulse}), \tag{3.2.6}$$

which can then be used to obtain the parameters for the continuous sigmoidal function $h_\infty(V)$.

3.2.3 Full-trace method

The parameter estimation technique described in Section 3.2.2 may lead to inaccuracies in the estimation of the kinetic parameters due to the nature of Assumption 1. More specifically, the assumption that the timescales of activation and inactivation are widely separated may not be

valid for some species of ion channels. In this case, the activation kinetics are "contaminated" by the simultaneous inactivation of the channel, resulting in poor approximations by (3.2.3)-(3.2.6). This issue can be resolved by fitting the voltage-step data directly to (3.2.2), whereby the values of m_∞, h_∞, τ_m, and τ_{h_i} at discrete voltages are obtained simultaneously.

Unfortunately the continuous function describing $\tau(V)$ can assume a variety of biophysically plausible functional forms as suggested by the use of the two different functions $\tau_1(V)$ and $\tau_2(V)$ in the present model. The root cause of this ambiguity is due to the fact that the voltage-dependent transition rates $\alpha(V)$ and $\beta(V)$ can assume various functional forms, which ultimately affects τ because $\tau = \frac{1}{\alpha+\beta}$ in an HH-formulated model. Although the steady-state activation curves also suffer from this issue of ambiguity (since $x_\infty = \frac{\alpha}{\alpha+\beta}$), they do so to a lesser degree than the time-constant curves since the mathematical properties of such rate functions guarantee a saturating functional form for x_∞.

Based on the considerations above, the software package `NEUROFIT` [69] was developed to assist modelers in developing accurate ionic current submodels. The fitting algorithm implemented within assumes that steady state activation is given by the Boltzmann function (3.1.7), and as a result the parameters for this function are returned by the algorithm. However due to the ambiguity in the function $\tau(V)$, only the values of τ are returned for each discrete voltage, requiring a secondary fitting to produce a continuous function for τ. The `NEUROFIT` package was utilized for the present model to parameterize the hyperpolarization-activated I_h current. More details on I_h are provided in Section 3.2.4.

3.2.4 Voltage-clamp fitting results

The ionic currents in the set $S = \{I_{NaP},\ I_K,\ I_A,\ I_{HVA},\ I_{LVA},\ I_h\}$ were parameterized according to voltage-clamp recordings. The use of `NEUROFIT` for fitting to voltage-clamp data was not possible (except for I_h) due to inavailibility of data or the use of voltage protocols not supported by the software. Fortunately, published voltage-clamp recordings exist for all currents in the set S with precise descriptions of the protocols used to evoke them. By simulating the voltage protocols described by the various experimenters, it was possible to parameterize the individual ionic models. Although in most cases the fitting for these currents was qualitative, the goal was to capture key features of the recorded currents; namely, the amplitude and rates of (in)activation. Steady-state (in)activation curves were assumed to have the form given by (3.1.7), while the voltage-dependent time constants $\tau(V)$ assumed one of the forms (3.1.8)-(3.1.10). The remainder of this subsection provides the results of voltage-clamp simulations for the currents in S along with brief summaries of

each current and references to the corresponding experimental studies. The estimates of kinetic parameters obtained from the voltage-clamp fittings are listed in Table A.1, while the estimates of maximum conductance parameters are listed in row g_{vc} of Table A.3.

I_{NaP}

A voltage-ramp recording of the persistent Na^+ current I_{NaP} published by Wang et al. [16] was used as a reference for fitting. The current I_{NaP} was isolated by Wang et al. [23] through a TTX-subtraction method. We point out that even though GnRH neurons conduct two types of TTX-sensitive Na^+ current, it is assumed that the fast Na^+ current I_{NaF} does not activate during the application of a sufficiently slow ramp protocol. In turn, this allows for the isolation of a separate current denoted I_{NaP}. The macroscopic current equation

$$I_{NaP} = g_{NaP} m_{NaP} h_{NaP} (V - E_{Na}), \tag{3.2.7}$$

is based on that used by Magistretti et al. [70] in a study of entorhinal cortex cells. Equation (3.2.7) was parameterized through the use of a genetic algorithm that minimizes the L_2-norm of the error between the simulated trajectory and the digitized current trace of Wang et al. [23]. Figure 3.2.1 shows the resulting model simulation of I_{NaP} under the ramp protocol used experimentally.

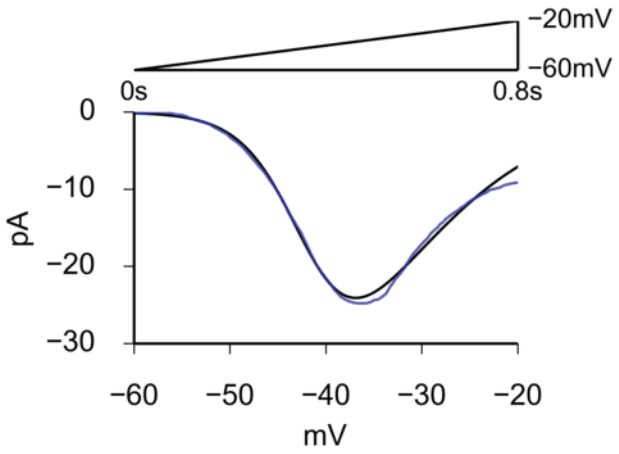

Figure 3.2.1: Simulation of I_{NaP} under a 50 mV/s ramp protocol vs. digitized experimental data (*blue*).

I_K and I_A

A voltage-clamp recording of the isolated K^+ currents I_A and I_K obtained by Pielecka-Fortuna et al. [19] was used as a reference for fitting. The voltage-clamp protocol used in [19] was designed to demonstrate the activation and inactivation characteristics of I_A and I_K separately. In their study, parameters for the activation curves of I_A and I_K were obtained using methods similar to those described in Section 3.2.2. These parameter values were used as initial estimates for the qualitative fitting process. The macroscopic expression for I_K assumes the form used in previous models of GnRH neurons [34, 35], that is,

$$I_K = g_K m_K^4 (V - E_K). \tag{3.2.8}$$

The expression for I_A is similar to that of other neuron models [62, 71] but has a composite inactivation term that was necessary to obtain the best fit. The resulting macroscopic equation is

$$I_A = g_A m_A [f_A h_{A,1} + (1 - f_A) h_{A,2}](V - E_K). \tag{3.2.9}$$

Figure 3.2.2 compares simulation (panel (a)) and recording (panel (b)) of $I_A + I_K$ under the experimental voltage protocol (top of panel (a)). A key characteristic of I_A is that pre-pulses lower than -40 mV remove inactivation of I_A so that a subsequent step to a depolarized potential (e.g. -10 mV) generates a transient spike in K^+ current. Meanwhile, I_K, which is uniquely active during the voltage steps corresponding to the -40 mV and -20 mV pre-pulses, shows a short delay in activation and is essentially non-inactivating, consistent with the lack of inactivation term in (3.2.8).

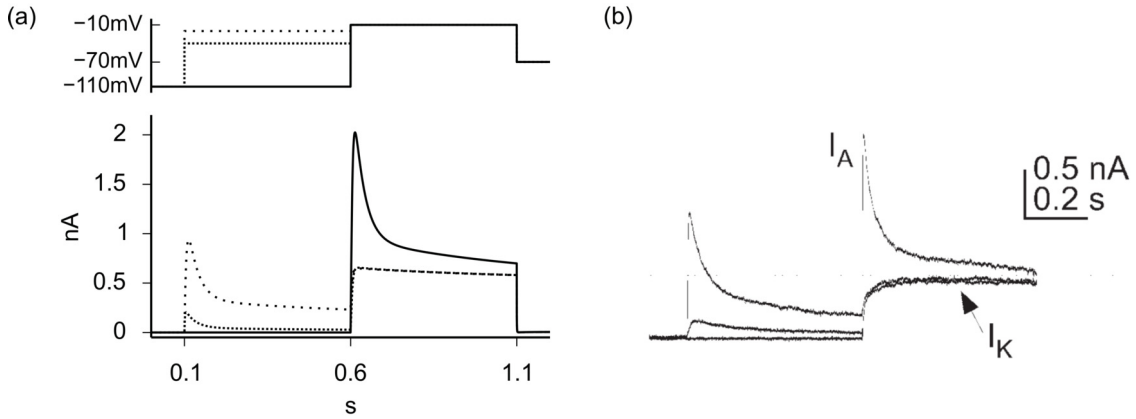

Figure 3.2.2: (a) Simulation of combined K^+ current (*bottom panel*) under pre-pulse voltage protocol (*top panel*). (b) Current traces obtained experimentally using the voltage protocol plotted in (a). Experimental figure from [19] used with permission.

I_{HVA} and I_{LVA}

The reference voltage-clamp recordings for the low- and high- voltage activated Ca^{2+} currents—I_{HVA} and I_{LVA} respectively—were obtained by Sun et al. [18]. In [18], it was demonstrated through the use of pharmacological agents that the high-voltage activated I_{HVA} actually represents the current conducted by a variety of Ca^{2+}channel types. However, by treating I_{HVA} as one entity, the authors were able to obtain the steady-state (in)activation curves of the combined current. The parameters of these activation curves were used as a basis for the fitting of I_{HVA}, whose equations assumed a standard HH form, except for the use of two inactivation variables to account for the diversity in HVA channel types. The resulting equation for I_{HVA} is given by

$$I_{HVA} = g_{HVA} m_{HVA} [f_{HVA} h_{HVA,1} + (1 - f_{HVA}) h_{HVA,2}](V - E_{Ca}). \tag{3.2.10}$$

A striking difference between the LVA and HVA Ca^{2+} currents is that the maximum amplitude of I_{HVA} was found to be at least an order of magnitude larger than that of I_{LVA} [18]. In fact, it was reported in [18] that only 41% of GnRH neurons exhibit a low amplitude LVA current. In contrast with this, however, is that another study recorded larger amplitude I_{LVA}, and found it to be conducted by 100% GnRH neurons in adult mice [31]. Therefore, the conductance and kinetic parameters of I_{LVA} may have a large range of physiologically acceptable values. The voltage range at which the low amplitude I_{LVA} was evoked by Sun et al. [18] is consistent with the voltage range of activation in T-type Ca^{2+} channels [31]. Based on this observation, the kinetics of I_{LVA} were fit to the voltage-clamp data in [31] using the current equation

$$I_{LVA} = g_{LVA} m_{LVA}^2 h_{LVA} (V - E_{Ca}), \tag{3.2.11}$$

which has the same form as I_{CaT} used by Lebeau et al. [34]. The maximum conductance g_{LVA} was then adjusted to fit the data in [18]. Figures 3.2.3a,b compare the results of the two voltage-clamp simulations with experiment for I_{HVA}. The model simulations for I_{LVA} are shown in Figure 3.2.3c.

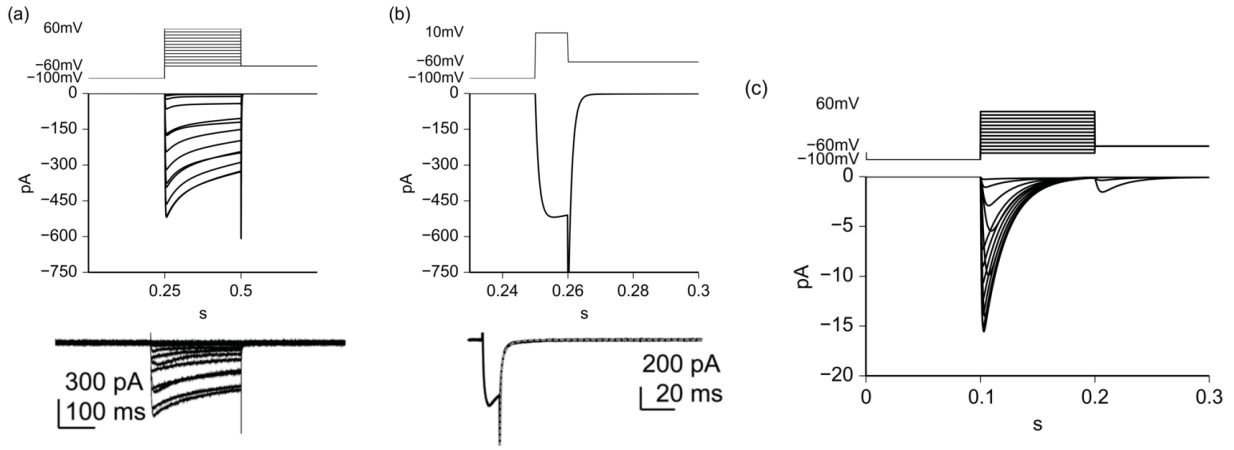

Figure 3.2.3: Simulations and recordings of voltage-gated Ca^{2+} currents in GnRH neurons. (a) Voltage-clamp simulation of I_{HVA} under pre-pulse protocol (*top panel*) vs. experimental data (*bottom panel*). (b) Similar to (a) but with short-duration voltage-protocol designed to evoke tail currents. (c) Simulation of I_{LVA} using similar pre-pulse protocol as (a) and (b). Experimental figures used with permission.

I_h

Current traces of I_h at different voltage steps were obtained by first digitizing published voltage-clamp data from [20]. This data was then input into `NEUROFIT`, which was configured to fit to a current equation of the form

$$I_h = g_h[f_h h_{h,1} + (1 - f_h)h_{h,2}](V - E_h). \tag{3.2.12}$$

The inclusion of two inactivation variables in (3.2.12) is based on a model of I_h by Dickson et al. [72]. Note that in the case of I_h, the use of the terms "activation" and "inactivation" can be misleading since in a physiological context, I_h exhibits little or no inactivation yet has two time scales of activation. In the context of modelling, the term "inactivation" is typically used to describe gating variables with a steady-state curve that saturates as $V \to -\infty$, even if the variables represent activation of the current. The fitting results generated by `NEUROFIT` are plotted against the digitized data in Figure 3.2.4.

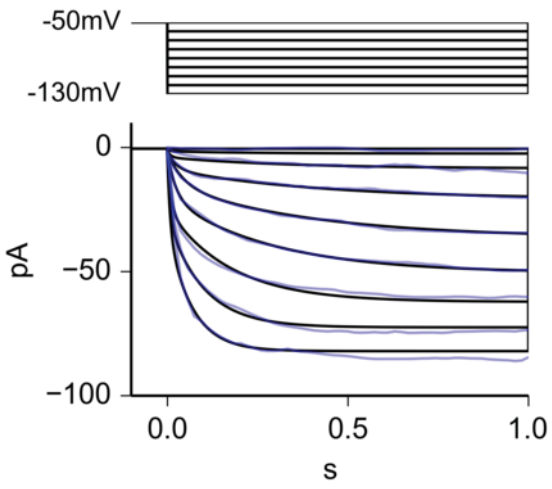

Figure 3.2.4: Voltage-clamp simulation of I_h (*black*) vs. digitized voltage-clamp data (*blue*).

3.2.5 Limitations of voltage-clamp recordings

Although voltage-clamp recordings are useful for modelling, one should keep in mind the implicit assumptions that are made when using voltage-clamp data for building single-compartment models of neurons, regardless of the method of parameterization. One significant assumption is that adequate "space-clamping" was present during the recording of the electrical data used for fitting. A perfect space-clamp is achieved when the membrane potential of the neuronal component is uniformly controlled, i.e., isopotential. However, the assumption of perfect space-clamp is only reasonable for spherical neuronal compartments [73]. In GnRH neurons, the somatic compartment is ellipsoidal [74], suggesting the presence of imperfect space-clamp in voltage-clamp recordings. Furthermore, there are two major dendritic processes in GnRH neurons that may affect the values of current obtained at the soma [35].

Given that there are space-clamp issues associated with the recording of ionic currents in voltage-clamp, it is understandable that spiking models of neurons require parameter tuning relative to the voltage-clamp fitted values in order to produce the correct qualitative behaviour (as is the case with the present model). On the other hand, parameter tuning in the full model might simply be needed to compensate for ionic currents that are missing in the model. If we assume that the model accurately represents the types of ion channels expressed on the membrane, then a recent study by O'Leary et al. [75] may explain the parameter discrepancies. In brief, their modelling study showed that the same average bursting activity can be obtained using different sets of maximal conductance parameters with similar ratios.

In fact, for certain conductance parameters, the acceptable range of values had an upper bound as much as twice the minimum value. Therefore, the notion of variability in ion channel density between cells exhibiting the same qualitative behaviour has physiological grounds, and should be taken into consideration when combining individual ionic currents to form a realistic bursting model for GnRH neurons.

3.3 Action potential fitting

Experimental recordings of spiking GnRH neurons in mice have revealed that the geometry of action potentials remains consistent (with some statistical variation) from cell to cell. Action potential (AP) shapes vary widely with species and anatomical location of the neuron, and hence there is no universal neuron model. Therefore, each model that aims to describe electrical activity in a certain type of neuron must be parameterized by fitting to data obtained from the correct species and cell type. Despite differences in AP shapes, there are still phases of the AP that are common across most types of spiking neurons. The initial or *depolarizing* phase of the AP begins when the rate of change in membrane potential exceeds some sufficiently high threshold. After the onset of an AP, the membrane potential increases rapidly before reaching a maximum, followed by a rapid decrease or *repolarization* back towards the pre-spike baseline. For some neurons, this repolarization leads to a membrane potential below the baseline before a recovery period of *afterhyperpolarization* (AHP) back up to the baseline. In some neurons, a net inward current after the AHP causes a small amplitude local maximum that lies above the baseline potential. This phenomenon is known as *afterdepolarization* (ADP). The AHP and ADP events are quantified by their maximum amplitude relative to the baseline, and/or their duration. Figure 3.3.1 shows a GnRH neuron exhibiting both an AHP and ADP.

Another property of firing or *spiking* GnRH neurons is the short duration of their APs: high resolution current clamp recordings of GnRH neurons have shown that the action potential duration (APD) is less than 1 ms during bursting and current injection experiments. APD can be quantified using the "full-width at half-maximum" (FWHM) measure. The half-maximum voltage is defined by the simple formula

$$V_{HM} = \frac{V_{th} + V_{max}}{2}.$$

The values of V_{th} and V_{max} are determined numerically. At the threshold voltage V_{th}, $\frac{dV}{dt}(V_{th}) = 1$ mV/ms, whereas V_{max} is the maximum voltage attained during the action

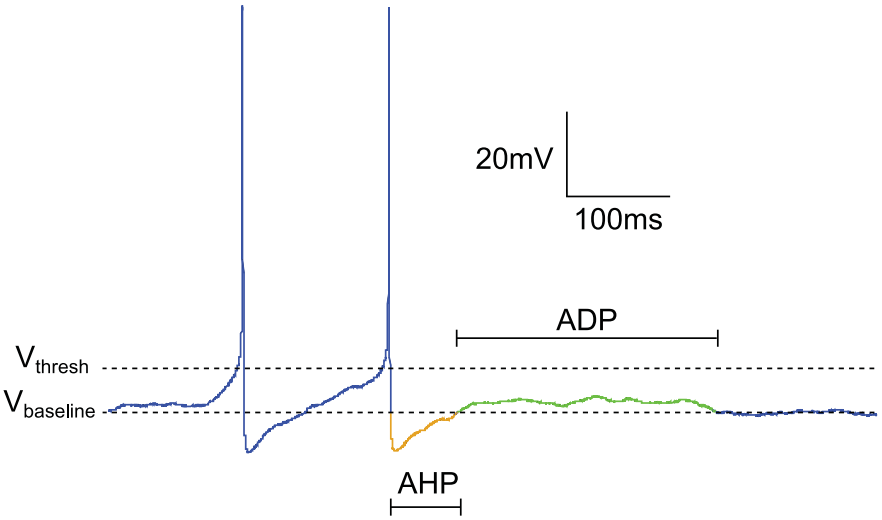

Figure 3.3.1: Typical neuronal action potentials with final spike exhibiting AHP and ADP. Data obtained from a whole-cell recording of a GnRH neuron.

potential. The APD for a spike is thus given by the difference in time between the two points that assume the value V_{HM}. GnRH neurons fire action potentials spontaneously, that is independent of external sources of current, but may also be forced to fire APs by a direct current injection from a resting state.

3.3.1 Fitting attempt I

During the course of modelling spiking activity in GnRH neurons, it was observed that the selected values of the parameters led to action potentials that were too wide (∼3-5 ms). This issue occurred when using a four-state reversible Markov model by Lebeau et al. [34] for the current I_{NaF}. Based on the large amplitude contributions of I_{NaF} and I_K during spiking activity, it was proposed that the submodels for these two currents be reparameterized to minimize the width of the action potential during spiking. This was motivated by the work of Wang and Buzaki [76], whose minimal Hodgkin-Huxley model (consisting of I_{NaF}, I_K and I_L) exhibits tonic spiking with APD and other AP characteristics similar to that observed in GnRH neurons. In addition to minimizing the APD to obtain the proper value, it is also crucial that the model generates realistic AP amplitudes, where amplitude is defined as the difference $V_{max} - V_{th}$. AP amplitudes of $80 - 100$mV have been observed experimentally in GnRH neurons [24, 10]. Therefore given the typical AP threshold voltage of $V_{th} \approx -50$mV, we expect the model to generate APs that peak between +30 and +50 mV. Since AP amplitude is also dependent on the interaction between I_{NaF} and I_K, we incorporated an AP amplitude constraint into the APD minimization procedure. As a final constraint, we

required that I_{NaF} and I_K also exhibit the correct behaviour in voltage-clamp simulations.

The requirements that the full model generates narrow action potentials with sufficiently large amplitude, and that the I_{NaF} and I_K submodels behave appropriately in voltage-clamp were used as the basis for designing an objective function in the parameter search algorithm. A set of 13 parameters from the I_{NaF} and I_K models were selected for the parameter variation, 10 of which represent the rate parameters of the 4-state Markov model for I_{NaF} by Lebeau et al. [34]. The maximum conductances g_{NaF} and g_K of I_{NaF} and I_K, and the scaling parameter e of the activation time constant τ_{m_K}, were also selected for variation. The I_{NaF} submodel was assigned more free parameters since simulations of I_K in voltage-clamp already showed good correspondence with experimental data as demonstrated in Section 3.2.4. In contrast, the I_{NaF} model had less reliable data for fitting implying more uncertainty in its rate parameters.

The objective or *fitness* function, F, used for the AP optimization consists of a sum of two types of error expressions. The first error expression, E_1, is assumed to be a sum of terms quantifying how well the model matches certain experimentally observed AP characteristics. We have that

$$E_1 = \sum_{i=1}^{n} \frac{|c_{model,i} - c_{obs,i}|}{|c_{obs,i}|}, \tag{3.3.1}$$

where c_i represents the i^{th} quantifiable characteristic of the action potential. The characteristics that were chosen for this study include: the global maximum and minimum voltage obtained during the simulation, mean action potential width measured according to the FWHM definition, mean interspike interval, and AP threshold for the first generated spike. Action potentials in this problem were simulated using a 600 ms, 10 pA current step applied from the resting equilibrium, as performed experimentally to evoke APs from rest [20]. The second error expression E_2, on the other hand, is assumed to be a measure of the error between model and data for a voltage-ramp simulation of the combined Na^+ current $I_{NaF} + I_{NaP}$. Data for this error calculation was obtained by digitizing an experimentally published recording [16] and interpolating it using `numpy` [77] linear interpolation at equally spaced time points. The relative L_2 error between model and data used in this study is defined by

$$E_2^2 = \frac{\sum_{j=1}^{N} |I_{model,j} - I_{obs,j}|^2}{\sum_{j=1}^{N} |I_{obs,j}|^2}, \tag{3.3.2}$$

where $I_j = I(t_j)$ are the values of the currents at the interpolation points. Note that relative error terms are used throughout so that individual error terms are equally weighted, i.e., no optimization criterion is deemed more important than any other.

The genetic algorithm and direct search method as implemented in MATLAB Optimization Toolbox [46] were employed for the action potential optimization task. Initial population ranges for the genetic algorithm and initial parameters for the direct search method were estimated based on the manual discovery of the parameters needed to generate spiking in the model. Although action potential characteristics can be optimized through manual or "hand"-fitting of parameters, the use of optimization routines automates the daunting task of searching a high-dimensional parameter space and often generates better results. Of course, the success of these optimization routines depends on the correctness of the underlying model, and the appropriate choice of error functions. The probabilistic nature of the genetic algorithm allows for a wider sweep of the parameter space when compared with the direct search method and thus was most successful at generating an optimal parameter set. Figure 3.3.2 shows the outcome of the genetic algorithm when minimizing the APD for model spikes, and minimizing the error between model and experimental Na^{2+} current under the 50 mV/s voltage-ramp protocol.

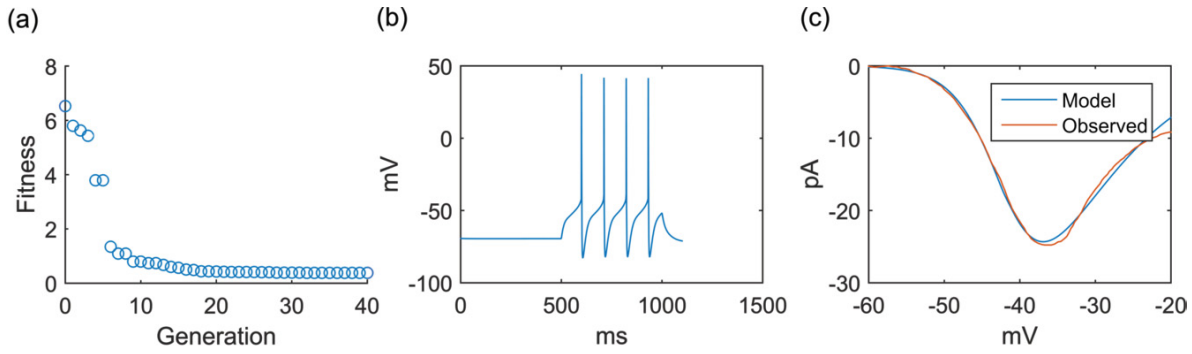

Figure 3.3.2: Output from the genetic algorithm for the action potential width and voltage-ramp optimization task. (a) Value of F as a function of generation number shows convergence to a potential minimum. (b) Time series of membrane potential corresponding to the best iteration. (c) Voltage-ramp simulation corresponding to best iteration.

Although the results from Figure 3.3.2 seem promising, closer inspection of the action potentials shows a more elevated threshold for firing and a steeper transition to firing than observed experimentally. Rather than modifying the error function F through additional terms, a different error function was implemented by incorporating voltage-time series data of a spiking cell into the optimization problem. The improved error function involves calculating the error between two signals in the phase plane in order to eliminate time from the fitting process as described in detail in Section 3.3.2.

3.3.2 Phase plane fitting method

The phase plane fitting method was developed to improve upon the traditional least-squares approach of fitting neuronal models to voltage time series data [78]. As described in [78], the least-squares fitness function introduces phase error, that is an increase in the value of the fitness coefficient depending on the relative phase between two signals. For example, without a reliable means of "phase locking" two signals, a stochastic integration of a model could generate spikes at different times than the data leading to large errors, even if the model is potentially accurate. Thus the phase plane fitting method, which involves fitting model to data in the $(V, \dot{V})$ plane, is computationally more efficient as it eliminates time from the fitting process. This allows the fitting algorithm to be started from any initial condition, as long as the system is not undergoing transient behaviour.

Assuming that the available data is in the form of a voltage time series, the first step when applying the phase plane method is to generate a time series of the derivative, $\dot{V}$. For the GnRH neuron data, this was accomplished by using `scipy` [77] interpolation tools to obtain a cubic spline interpolation of the time series and then using the built-in methods to calculate the derivative. Plotting V vs. $\dot{V}$ for the data reveals a characteristic cycle that clarifies the geometry of different components of the action potential as is shown in Figure 3.3.3c.

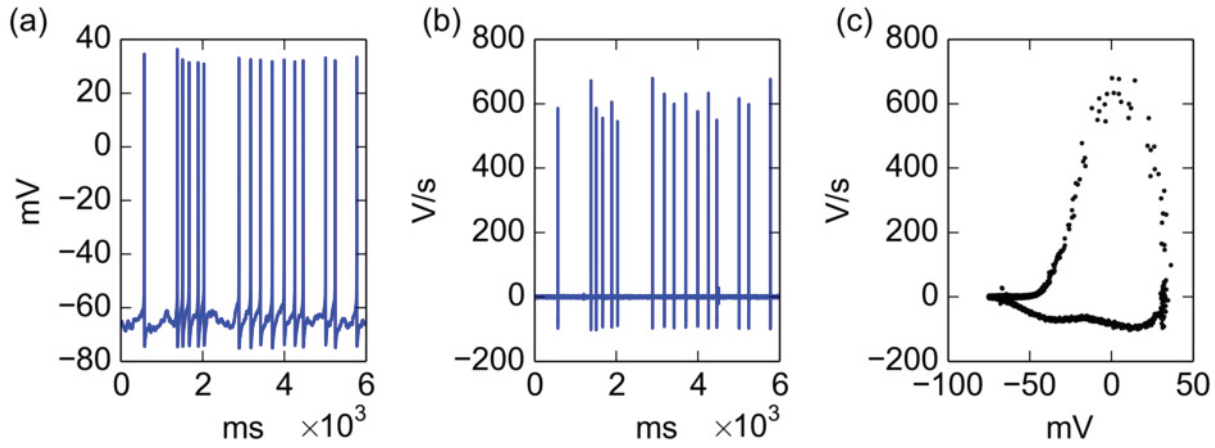

Figure 3.3.3: Data from a recording of GnRH neuron membrane potential. (a) Membrane potential, V. (b) Rate of change of V as a function of time. (c) Scatter plot of rate of change of V as a function of V.

The error function for this fitting method relies on calculating the temporal density of the trajectory in the $(V, \dot{V})$ plane. Denoting a point in the plane by $x = (V, \dot{V})$ and a point on the system's trajectory by $y(t) = (V(t), \dot{V}(t))$, the continuous formulation for the temporal

density of the trajectory at a point x is given by

$$D(x) = \frac{1}{T}\int_0^T \delta(x - y(t))\, dt, \tag{3.3.3}$$

where T is the final time for the data and δ is the Dirac delta function. However, for equally spaced data points y_i (with spacing Δt), (3.3.3) is calculated numerically using the discrete approximation of the density function

$$D(x) = \frac{1}{N}\sum_{i=1}^{N} \eta(x, y_i)$$
$$\eta(x, y) = \begin{cases} 0, & y \notin \Omega(x) \\ 1, & y \in \Omega(x) \end{cases},$$

where $N{=}\frac{T}{\Delta t}$ and $\Omega(x)$ is some small neighbourhood of x. Based on this, the error between the model and the observed data at x is defined as

$$E(x) = D_{model}(x) - D_{obs}(x). \tag{3.3.4}$$

The total error is then obtained by integrating (3.3.4) over an area in the $(V, \dot{V})$ plane that contains both the model and data trajectories. In practice the integration area A in the $(V, \dot{V})$ plane is discretized into a grid consisting of, for simplicity, rectangular cells of equal area. A simple way to define A so that both trajectories are contained in A is

$$A = [\min_{V\in\{V_{model},V_{obs}\}} V, \max_{V\in\{V_{model},V_{obs}\}} V] \times [\min_{\dot{V}\in\{\dot{V}_{model},\dot{V}_{obs}\}} \dot{V}, \max_{\dot{V}\in\{\dot{V}_{model},\dot{V}_{obs}\}} \dot{V}].$$

Thus by choosing a grid spacing h_i in the V-direction and h_j in the $\dot{V}$-direction, we obtain the rectangular cells $\Omega_{ij} \in A$. We then normalize $E(x_{ij})$ by the area of Ω_{ij} to obtain the total discretized error

$$E_{tot}^2 = \sum_{i,j} \left(\frac{E(x_{ij})}{|\Omega_{ij}|}\right)^2, \tag{3.3.5}$$

where $|\Omega_{ij}|$ is the area of the cell. In the typical case of equal grid spacing, $|\Omega_{ij}| = |\Omega|$ can be taken as a common factor outside the sum in 3.3.5. In this case, the following relative error function is obtained for the purposes of equal weighting in fitness functions with multiple terms:

$$R^2 = \frac{\sum_{i,j}[D_{model}(x_{ij}) - D_{obs}(x_{ij})]^2}{\sum_{i,j} D_{obs}(x_{ij})^2}. \tag{3.3.6}$$

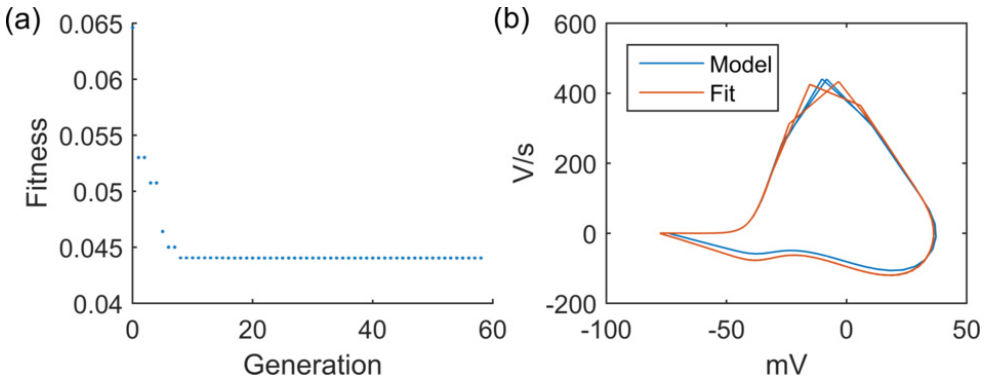

Figure 3.3.4: Validation of the phase plane fitting method using GnRH neuron model. (a) Convergence of fitness function to a potential minimum. (b) Model reference curve (*blue*) and the trajectory (*orange*) corresponding to the best genetic algorithm iteration.

As a validation of the phase plane fitting method, a continuously spiking version of the GnRH neuron model was fit to itself. Specifically, the genetic algorithm was run with the fitness function given by (3.3.5) using g_{NaF} and g_K as free parameters. As shown in Fig. 3.3.4, the trajectory in the phase plane is recovered accurately and the parameters selected by the genetic algorithm were close to the model values. For this fitting, the grid spacing in the $(V, \dot{V})$ was equal in both directions with $h_i = h_j = 1$. This spacing is hereafter used as the default value for all fitting attempts.

3.3.3 Fitting attempt II

Using the phase plane fitting method, various models for the transient sodium current I_{NaF} were tested to compare how well they allowed the full model to fit the data shown in Fig. 3.3.3. It was assumed that the other parameters in the model, except for g_K and the scaling parameter e for τ_{m_K} remained static. Different models were selected because initial fitting attempts (discussed above) showed that the originally proposed sodium model did not generate an adequate fit to the phase plane data. The schematics of the four fast sodium models that were tested are shown in Figure 3.3.5. Model A is the reversible version of a three-state model for the squid axon Na^+ channel [63], model B is that used in Section 3.3.1, model C is the same as model B but does not satisfy a detailed balance condition (enforced in model B through the parameter a), and model D is the Hodgkin-Huxley model for the squid axon Na^+ channel [32].

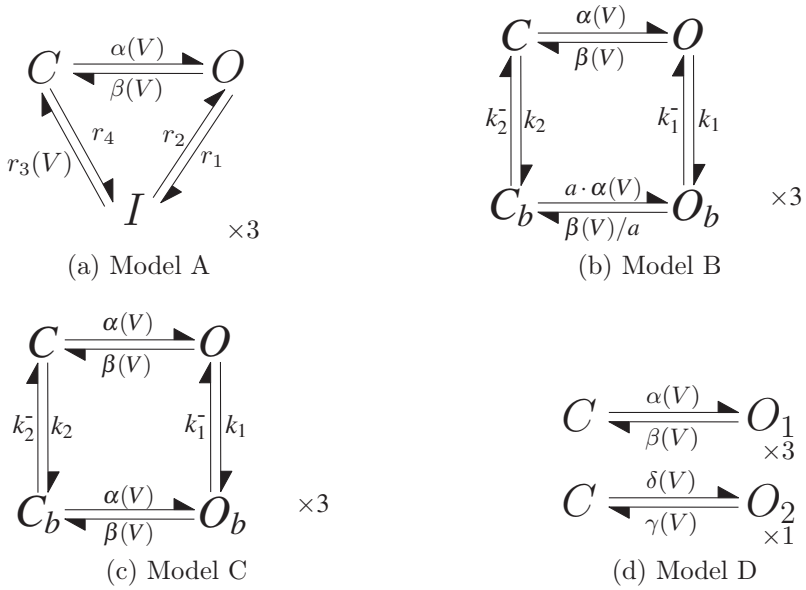

(a) Model A (b) Model B

(c) Model C (d) Model D

Figure 3.3.5: Schematic diagrams for the four Markov models of I_{NaF} tested under the phase plane fitting method. Each diagram represents the transitions undertaken by independent subunits of the Na^+ channel (the number of subunits is indicated by a multiplier next to each diagram). (a) 3-state reversible model. (b) 4-state reversible model satisfying microscopic reversibility. (c) 4-state reversible model without microscopic reversibility. (d) Hodgkin-Huxley gating model.

The voltage dependent rates α, β, r_3 appearing in Figure 3.3.5a-c are given by sigmoidal functions of the form $\frac{a}{1+\exp(\frac{V+b}{c})}$, while α, β and δ, γ of Figure 3.3.5d are given by pairs of exponentials of the form $a\exp(-\frac{bV}{c})$ and $d\exp(\frac{(1-b)V}{c})$, $0 \leq b \leq 1$ [68]. The macroscopic current equation for models A-C is given by,

$$I_{NaF} = g_{NaF}O^3(V - E_{Na}), \tag{3.3.7}$$

while for model D,

$$I_{NaF} = g_{NaF}O_1^3O_2(V - E_{Na}). \tag{3.3.8}$$

The physical interpretation of the Na^+ channel according to models A-C is that it consists of three independent subunits where each subunit has identical transition kinetics as determined by the appropriate diagram in Figure 3.3.5. Meanwhile, the Hodgkin-Huxley model assumes three identical "activation" subunits and one "inactivation" subunit, all of which operate independently. Note that it is possible to extend the Markov models of A-D, shown in 3.3.5, to include all possible subunit configurations associated with the Na^+ channel and describe the macroscopic current by the equation

$$I_{NaF} = g_{NaF}O(V - E_{Na}),$$

but these complex models are expensive to compute due to the number of states that they possess. For example, the Hodgkin-Huxley model (model D) has the well-known equivalent Markov formulation shown in Figure 3.3.6a, whereas the equivalent formulation for the 2 subunit version of model A is shown in Figure 3.3.6b. Writing down the differential equations for these equivalent formulations results in large systems of ODEs with dimension determined by the number of states (minus one to account for conservation). On the other hand, using the subunit formulation, the ODE systems corresponding to (3.3.7) and (3.3.8) have dimension 2 for models A and D, and dimension 3 for models B and C.

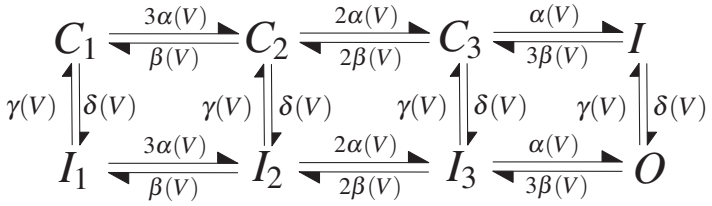

(a) Model D

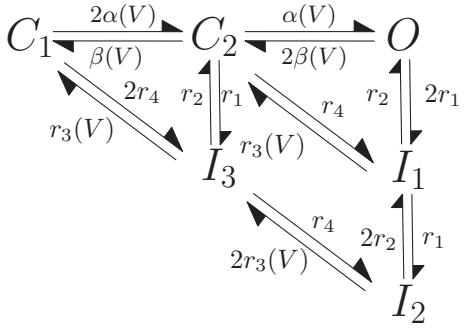

(b) Model A (2 subunit version)

Figure 3.3.6: Extended Markov models corresponding to (a) model D, and (b) model A of Fig. 3.3.5.

The four different models vary in the number of free parameters with model A having 12, and models B-D having 10. For the phase plane parameter fitting, these kinetic parameters plus the maximum conductance g_{NaF}, and the two I_K parameters were varied within the parameter space. Figure 3.3.7 shows the results associated with models A and C, which had the most success in fitting the various components of the action potential. Specifically, these two models fit well to all components except the peak of the action potential, where an overshoot in the maximum voltage occurs. In fact, the overshoot in peak voltage was encountered by all four models suggesting that the kinetics for I_K need to be optimized, or that there is an ionic current missing from the model. A potential candidate for this missing current is the "big-conductance" Ca^{2+}-activated K^+ current I_{BK}, which is present in GnRH neurons [27, 3], and is known to contribute to repolarization of the action potential [64]. The voltage and Ca^{2+} dependence of activation for this current, however, have yet to be quantified experimentally in GnRH neurons.

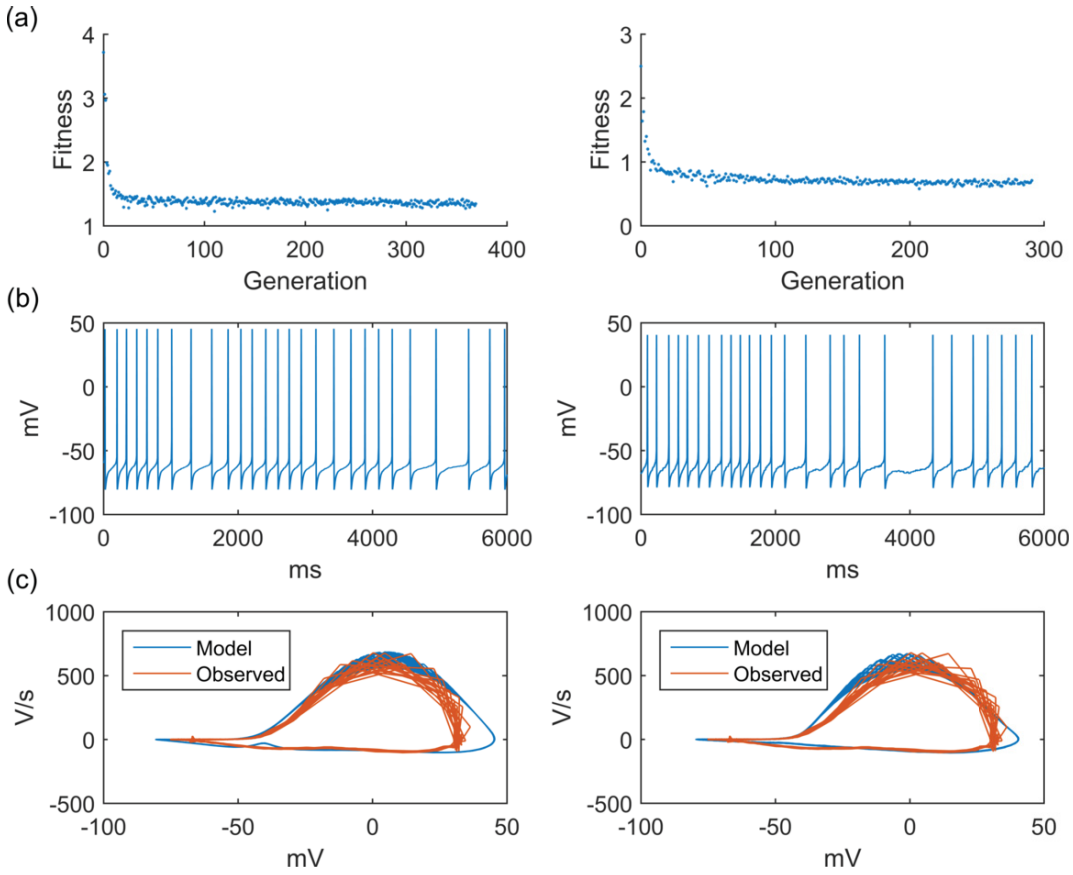

Figure 3.3.7: Phase plane fitting results corresponding to I_{NaF} models A (*left column*) and C (*right column*). (a) Value of the fitness function plotted against generation number. (b) Voltage time-series corresponding to best iteration of the genetic algorithm. (c) Comparison of best model trajectory with experimentally observed trajectory in the $(V, \dot{V})$ phase plane.

Figures 3.3.7 and 3.3.8 show that models B and D performed worse than models A and C. The main issue with model B is that the onset of the action potential is too depolarized. Meanwhile model D shows a clear inability to fit to the phase plane data. It is also worth noting that the detailed-balance constraint for model B produces undesirable stiffness in the system, leading to a timestep requirement of $dt = 0.001$ for stable numerical integration. For the other models, a timestep of $dt = 0.01$ was sufficient. Although the requirement for a smaller timestep might be perceived as a non-issue, recall that GnRH neurons exhibit interburst intervals on the order of 1-100 seconds. Therefore, long-term stochastic simulations of bursting behaviour, which are typically integrated using the Euler-Maruyama (EM) method (see Section 2.1.2), may be rendered impractical with such a small timestep. The implementation of an adaptive Runge-Kutta SDE solver [79] or an implicit SDE solver [44] would likely alleviate the problem, and should be considered for future fittings.

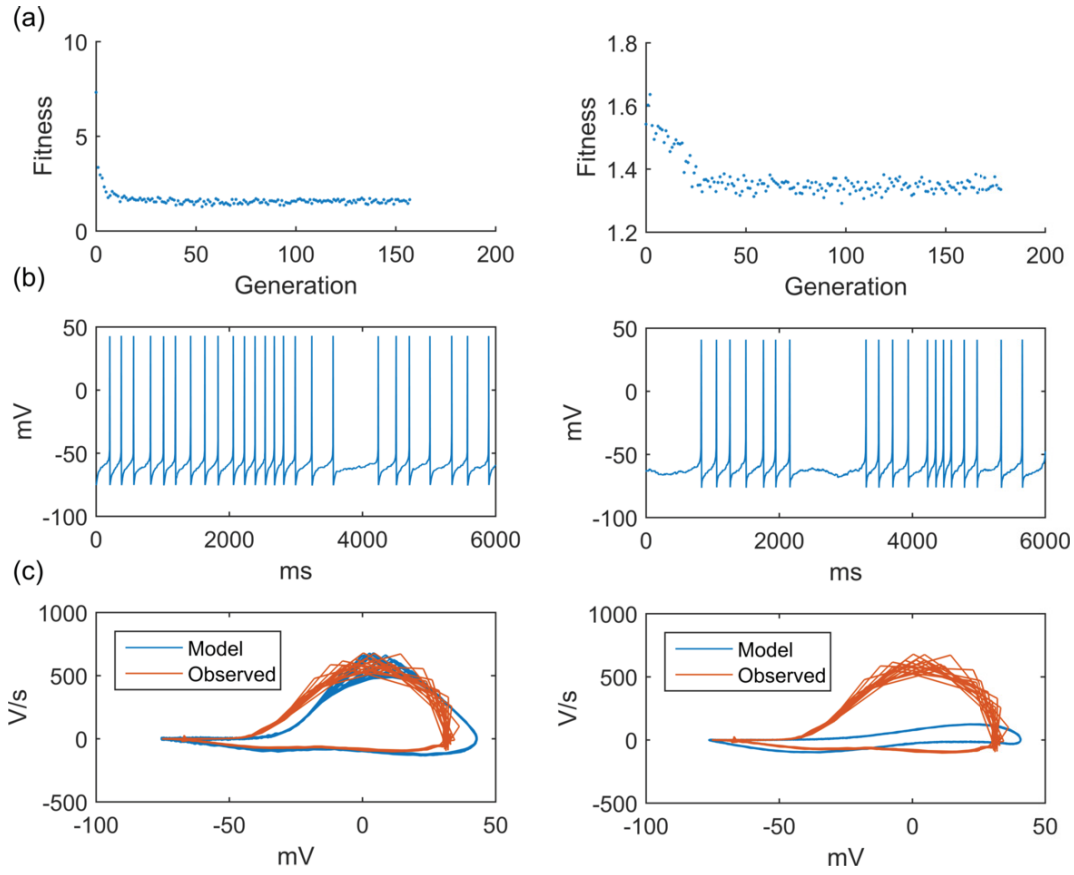

Figure 3.3.8: Phase plane fitting results with I_{NaF} models B (*left column*) and D (*right column*). Rows (a)-(c) show the same information as in Fig. 3.3.7.

Based on the results shown in Figs. 3.3.7 and 3.3.8, we can conclude that model A is the best to use for studying bursting activity in GnRH neurons. Unfortunately, this model is not able to capture the desired behaviour when fitting to the voltage-ramp data for the combined Na^+ current (recall Section 3.3.1) and the phase plane data simultaneously. Resolving this discrepancy remains an open topic of research. To conclude, although more biophysically-detailed models for I_{NaF} certainly exist [80, 63, 81], the selected model provides a reasonable balance between biophysical detail and the ability to simulate most features of the GnRH neuron action potential.

3.3.4 Limitations of phase plane fitting

The results from Section 3.3.3 suggest that the phase plane fitting method is a powerful tool for the development of neuronal models. The method has also established success in parameter fitting for other complicated neuronal systems [82, 83]. However, the use of this method revealed certain practical issues while fitting to GnRH neuron data. Specifically,

for the initial fitting attempt the genetic algorithm converged to solutions for which the maximum value of the derivative $\dot{V}$ is well below the observed value. Occasionally, the genetic algorithm would even converge to solutions with no action potentials. The issue becomes clear when considering the phase plane density of the trajectory for the GnRH neuron data as shown in Figure 3.3.9—the density of points is highest in the region corresponding to the quiescent phase of the neuron. For the purposes of demonstration the color bar in Figure 3.3.9 reaches a maximum of 5, but many cells in the quiescent region of the phase plane have a much higher density. This phenomenon is a consequence of short duration spikes separated by interspike intervals that are 2-4 orders of magnitude longer. This issue can be addressed by using a modified form of (3.3.5),

$$E_{tot} = \left(\sum_{i,j} \sqrt{\frac{E(x_{ij})}{\Omega_{ij}}} \right)^2, \tag{3.3.9}$$

which gives more weight to sparsely populated cells, but at the expense of giving a higher weight to noise [83]. Figure 3.3.9 also demonstrates the effect of the grid spacing on the distribution of the trajectory density. As shown in Fig. 3.3.9c, a large grid spacing distributes more points to the regions of negative $\dot{V}$, which may assist the genetic algorithm in escaping from suboptimal solutions at the expense of a less accurate solution. Although the grid spacing does affect the performance of the genetic algorithm, this issue can be overcome using the technique of Section 3.3.1, that is by the coupling of additional terms to the fitness function. Following this strategy, relative errors in the minima and maxima of V and $\dot{V}$, mean action potential width, and mean interspike interval were computed and added to (3.3.6) to achieve the best overall fits to the data, which are shown in Section 3.3.3.

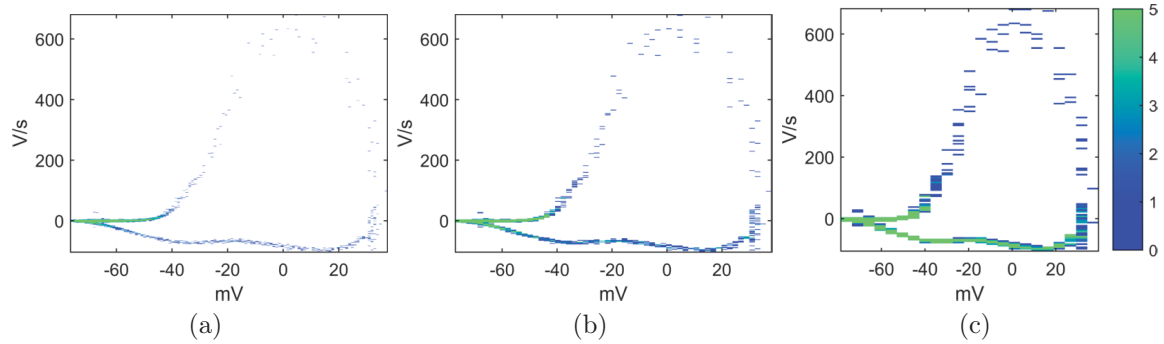

(a) (b) (c)

Figure 3.3.9: Phase plane density of the GnRH neuron time-series data under different grid discretizations. Colors represent the number of data points in a given cell. (a) $h_i = h_j = 1$. (b) $h_i = h_j = 2$. (c) $h_i = h_j = 5$.

3.4 Modelling oscillations

3.4.1 Review of oscillatory electrical activity in neurons

Various ionic mechanisms exist for generating intrinsic oscillations in single neurons. Although there are many different combinations of currents that can produce oscillations, it is helpful to consider what *classes* of currents must be present in order to generate oscillations. With this knowledge, certain currents can be ruled in or out in terms of their contribution to pacemaking activity.

A simple way to achieve oscillations in a HH model is to combine two currents, one with an amplifying gating variable and one with a resonant gating variable [48]. Recall that an inward *amplifying* current is one that undergoes positive feedback with a depolarizing perturbation of the membrane potential, while an inward *resonant* current undergoes negative feedback with depolarization to produce a net outward current. Outward amplifying and resonant currents have a similar definition. A classic example of an inward resonant current is the hyperpolarization-activated current I_h that appears in the present model. This current is modelled using only an inactivation or "h" gate whose resonance effects are clear. More specifically, with a depolarizing perturbation in membrane potential, h decreases to produce a net outward current to shunt the depolarization, whereas the opposite effect is observed when hyperpolarizing perturbations increase h to cause a rebound depolarization. The situation is reversed when we consider a current with the same type of gating as I_h but with a reversal potential that reverses the direction of the current. A well-studied current that has this property is the inward-rectifier potassium current or I_{Kir}. By considering the behaviour of the current with small hyperpolarizing perturbations to the membrane potential, we conclude that I_{Kir} is an outward amplifying current. Therefore, combining I_{Kir} and I_h should theoretically be able to generate sustained oscillations, an outcome that is confirmed in Figure 3.4.1. The voltage equation used to generate the simulations in Figure 3.4.1 is

$$\dot{V} = I_{app} - g_L(V - E_L) - I_h - I_{Kir},$$

where the kinetics of the I_h model are the same as that used in the GnRH neuron model. The kinetics of I_{Kir} were obtained from [48]. Figure 3.4.1 also shows the existence of hysteresis in the trajectory of I_h, while I_{Kir} assumes approximately the same trajectory during the repolarizing and depolarizing phases of the oscillation. A similar phenomenon has been observed in the I_{NaP}+I_h subsystem, where I_{NaP} assumes the role of I_{Kir} [72]. The overall effect is reflected in the voltage time-series, where a delay in the activation of I_h causes a long-lasting plateau at the peak of the oscillation. Mathematically, this effect is explained

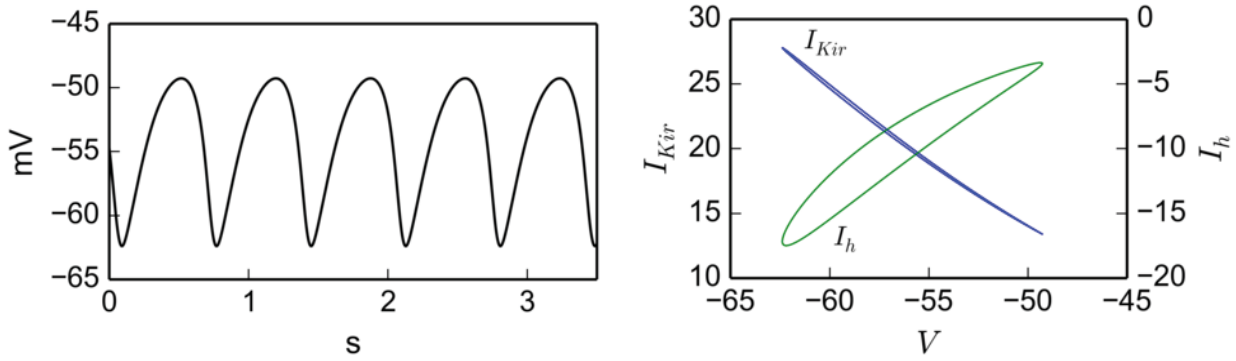

(a) (b)

Figure 3.4.1: Membrane potential oscillations in the $I_h + I_{Kir}$ system. (a) Voltage time series showing stable oscillations. (b) Phase plane diagram of I_h (*green*) and I_{Kir} (*blue*) vs. V. The upstroke and downstroke of the oscillation in I_h occurs via different pathways, indicative of a hysteresis. I_{Kir} shows approximately the same linear dependence on V during both phases of the oscillation, suggesting little or no hysteresis.

by the large separation in time scales between the gating variables for I_h and I_{Kir}. In summary, we remark that in a two current system (+ leak), oscillations may occur for some (narrow) set of parameters regardless of the directions of the ionic currents, as long as one of them is amplifying and one of them is resonant. Furthermore, the kinetic parameters of the interacting currents dictate the period and shape of the oscillations.

3.4.2 Membrane potential oscillations in GnRH neurons

Although rare, slow oscillations in membrane potential with period of 10-20 s and amplitude of 20-40 mV have been observed in GnRH neurons [10]. These oscillations are referred to as "subthreshold" since the peaks of the oscillations are not sufficiently depolarized to initiate action potentials. Given that oscillatory activity is rare, we expect that the voltage-clamp fitted values of the parameters may deviate from those needed to produce oscillations. Higher frequency (∼1 Hz) subthreshold oscillations have been observed in entorhinal cortex layer II (EC) cells [72], where it was shown via a minimal Hodgkin-Huxley model that the currents I_h, I_{NaP}, and I_L interact in a feedback loop to generate oscillations. In the previous subsection, it was also demonstrated that I_h, I_{Kir}, and I_L can produce oscillations that peak in the subthreshold regime. Although these currents are active in the present model, the frequency of the subthreshold oscillations generated by their interaction preclude them from being solely responsible for generating the much slower oscillations observed in GnRH neurons. Given the difficulty in simulating subthreshold oscillations with the correct period using the voltage-

clamp fitted currents, a phenomenological approach was taken. Motivation for this approach was drawn from a successful model for parabolic bursting in *Aplysia*, which is commonly referred to as the Plant model [84]. In the Plant system, there are two slow processes that interact to generate oscillations with a similar period to that observed in GnRH neurons, namely a slow inward Ca^{2+} current (I_s) and a Ca^{2+}-dependent K^+current (I_{KCa}). Although the activation of I_{KCa} by intracellular Ca^{2+} is instantaneous, Ca is a variable in the model with slow dynamics, ultimately leading to slow dynamics in I_{KCa}. A feedback loop can occur in this system as a result of the slow inward current I_s transporting Ca^{2+} ions into the cell and subsequently activating I_{KCa} which counteracts the depolarization induced by I_s. Due to the similarities in parabolic bursting between the R15 neuron of *Aplysia* and GnRH neurons in mice, a reparameterized form of the I_s, I_{KCa}, Ca submodel was incorporated into the full GnRH neuron model, where I_{KCa} is defined by (3.1.13) and

$$I_s = g_s m_s (V - E_{Ca}). \tag{3.4.1}$$

To partially support the claim that this submodel is compatible with the physiology of GnRH neurons, we note that I_{KCa} (as carried by SK channels) has been shown to exist in these neurons [17]. However, I_s has not been isolated and thus its presence remains a conjecture. In Chapter 4 we show that this phenomenological description is adequate for qualitatively reproducing the two types of bursting behaviour observed in GnRH neurons. We remark that, in contrast with the phenomenological current $I_{AHP-UCL}$ used in previous models and described in Chapter 1, the maximum conductance values of I_s used to simulate electrical activity are of the same order of magnitude as other currents in the model (see Table A.3).

The slow submodel described above was parameterized simultaneously by coupling it with the voltage-clamp fitted currents described in Section 3.3, and manually adjusting the parameters to achieve a subthreshold oscillating state. Initial estimates for the parameters were obtained from the Plant model and a previous model for irregular bursting in GnRH neurons [34]. The parameters were further constrained by requiring that intracellular Ca^{2+}concentration remains within physiological levels ($< 1\mu M$). In the process, some maximum conductances of the previously fitted currents were adjusted in order to simulate the correct behaviour—these parameter discrepancies are listed in Table A.3. In Table A.3, the set of parameters g_{sub} are those used to simulate subthreshold oscillations in the model.

Figures 3.4.2a,b show the conductance parameter regimes where stable subthreshold oscillations can occur. The one-parameter bifurcation diagram (Fig. 3.4.2a) shows that a narrow interval for g_s supports stable oscillations. To understand how g_s and g_{KCa} are correlated when stable oscillations exist, a periodic solution with period of $T = 15$ s was

continued in two parameters to obtain the locus of points shown in Fig. 3.4.2b. The positive and near-linear relationship between g_s and g_{KCa} shows that I_s and I_{KCa} oppose each other in a feedback loop provided that a certain ratio of g_s to g_{KCa} is maintained.

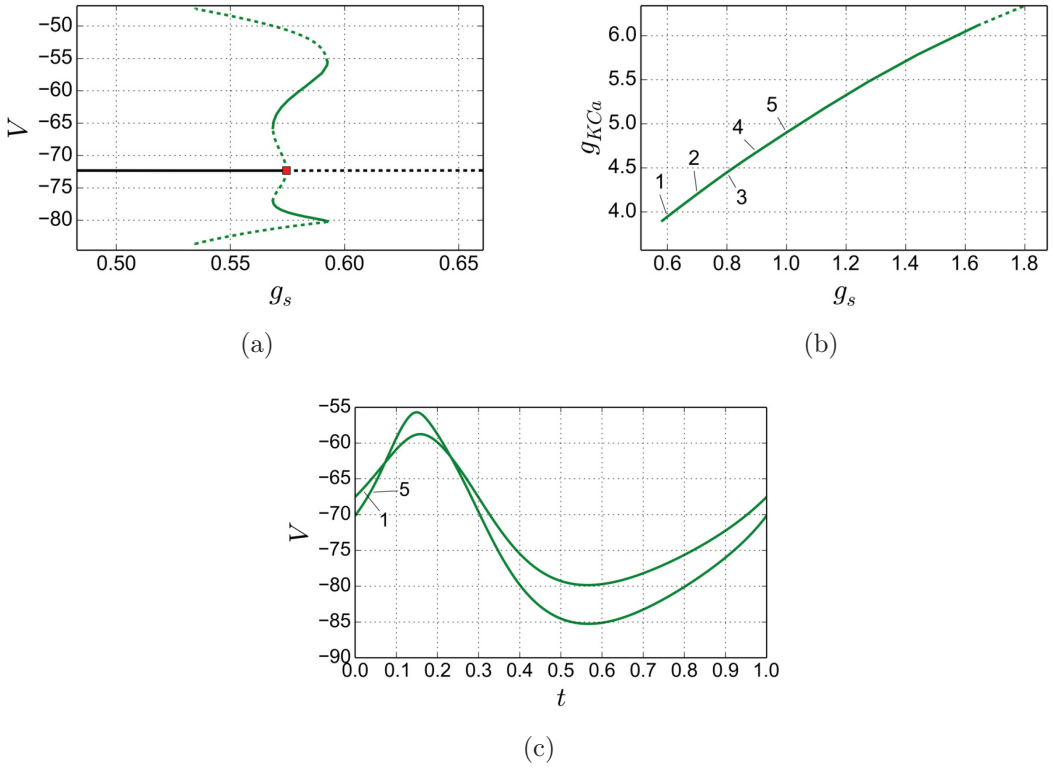

Figure 3.4.2: Dependence of subthreshold oscillations on model parameters. (a) One-parameter bifurcation diagram of V vs. g_s. Black-solid (-dashed) lines represent the stable (unstable) branches of steady states and green-solid (-dashed) lines represent the branches of stable (unstable) periodic orbits emerging from a subcritical Hopf bifurcation point (red square). Note that periodic orbits are represented by their minimum and maximum values attained during a cycle. (b) Existence of periodic solutions with fixed period of $T = 15$ s as a function of g_{KCa} and g_s. (c) Fixed period solutions of V at parameter values specified by the points labeled "1" and "5" in (b), where t represents time divided by the period of the oscillations. The periodic solution labeled "5" shows a sharpened peak due to the partial activation of Na^{2+} current.

Chapter 4

Model simulations and analysis

In this chapter, we demonstrate that the model presented in Chapter 3 can reproduce both the parabolic and irregular bursting behaviour with an appropriate choice of maximum conductance parameter set chosen from Table A.3. Using the model, we (i) demonstrate how individual ionic currents contribute to different phases of the parabolic burst cycle, (ii) show that changes in the conductance of I_{KCa} modulate excitability, and (iii) explain how noise leads to the generation of irregular bursts. To understand bursting behaviour from a dynamical systems point of view, we also apply slow-fast subsystem analysis to examine the mechanism(s) underlying the transitions between quiescence and spiking during both types of bursts. In turn, these numerical findings motivate the study of a simplified quadratic integrate-and-fire (QIF) model [38] that generates the two types of bursting and can be analyzed analytically.

4.1 Parabolic bursting

It was demonstrated experimentally that 1-2% of GnRH neurons can spontaneously generate parabolic bursts of action potentials with slow oscillations underlying them [10]. This type of bursting can be generated by the model described in Chapter 3 using the set of conductance parameters g_p defined in Table A.3. Compared with the parameter set g_{sub}, the set of parameters g_p allowed the model to generate slow oscillations in membrane potential that are depolarized enough to generate a cluster of action potentials at the peak of the wave. Parabolic bursting was observed in the deterministic model ($\eta = 0$) and was also sustained in the presence of noise as shown in Figure 4.1.1b. The model agreed with experimental recordings of parabolic bursting in terms of interburst interval, active phase

duration, interspike interval (ISI), and spike frequency profile (Fig. 4.1.1c). The model did however produce larger amplitude action potentials than observed experimentally but still within the range $(80-100$ mV) observed for action potentials generated via current injection or irregular bursting [20, 10].

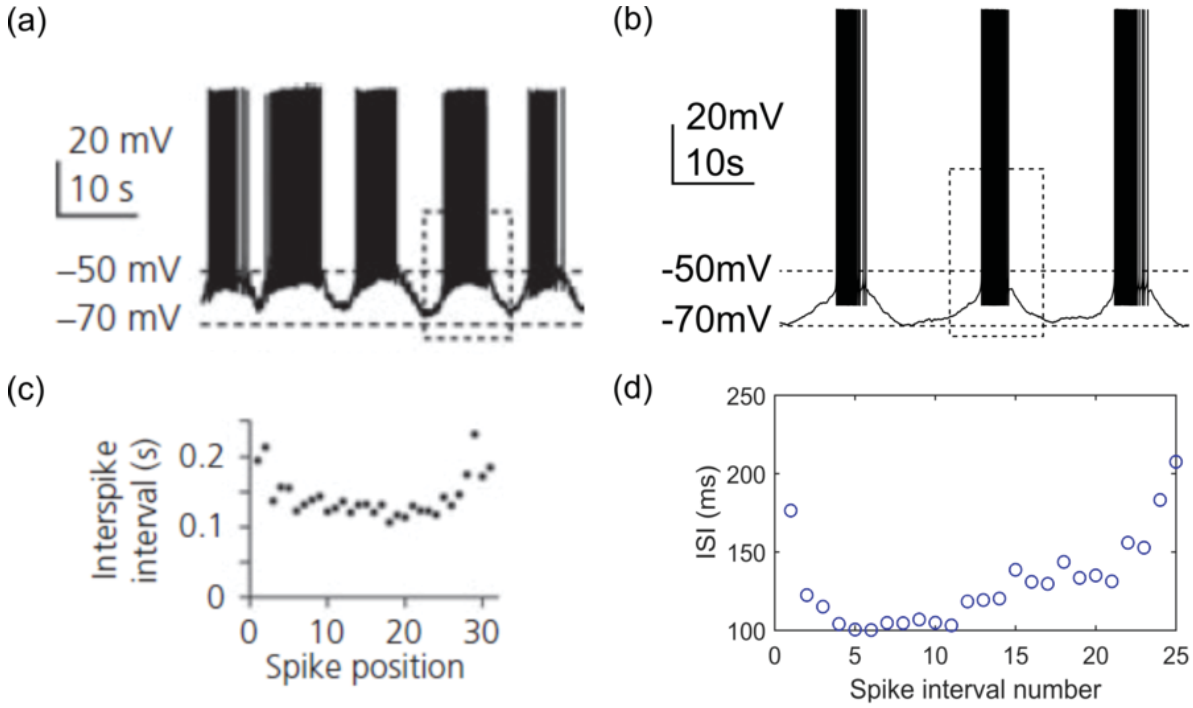

Figure 4.1.1: Parabolic bursting in GnRH neurons. (a) Experimental recording of membrane potential in a GnRH neuron. (b) Stochastic simulation ($D = 0.25$) of membrane potential. (c), (d) ISI profile during the active phases marked by a dashed rectangle in (a), (b) for both the (c) experimental recording and (d) numerical simulation.

Furthermore, the parabolic bursting model was capable of displaying slow oscillations when spiking is suppressed by TTX (i.e. by setting $g_{NaF} = g_{NaP} = 0$), as observed experimentally [10]. Since the Na^+ currents I_{NaF} and I_{NaP} are essentially inactive during the quiescent phase of the burst cycle, the slow wave underlying parabolic bursting is reasonably approximated by that obtained during the TTX-simulation. Therefore, by studying the simpler dynamics of the non-spiking wave, we can gain insights into the processes generating the quiescent phase of parabolic bursting. Similar to the case of subthreshold oscillations discussed in Section 3.4.2, the underlying slow wave is mainly driven by the interaction between I_s and I_{KCa}. Although there are other currents that are active during the slow wave, mainly I_A, I_h, I_{HVA}, and I_K, their amplitudes are smaller than that of I_s and I_{KCa}. However, the currents I_A and I_h did have some effect on certain aspects of the slow wave: increasing the conductance of I_A lengthened the period of the wave, while increasing the conductance of I_h

reduced the amplitude of the oscillations. The model also revealed that contributions from the two currents I_{HVA}, and I_K were more prominent at the peak of the wave, suggesting a more significant role for these currents in the generation of action potentials, i.e., during the active phase of the burst. The Ca^{2+} current I_{LVA} was minimally active during the slow wave, consistent with observations from a previous modelling effort [36]. These observations concerning the slow wave are demonstrated in Figure 4.1.2, where we show the contributions of various ionic currents underlying slow oscillations in membrane potential. Figure 4.1.2 also demonstrates the model prediction that there exists a latency in peak intracellular Ca^{2+} relative to voltage, a phenomenon that has been observed in cells exhibiting irregular bursting [1]. To the author's best knowledge, the Ca^{2+}-imaging experiments needed to confirm the prediction for the parabolic bursting case have yet to be performed.

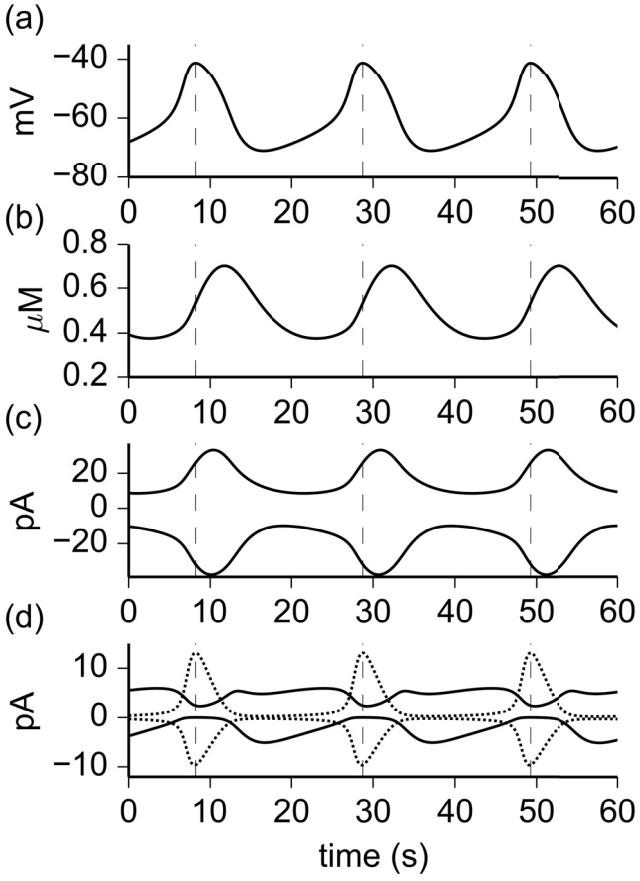

Figure 4.1.2: Measurements of various physical quantities when simulating TTX-induced suppression of spiking during parabolic bursting. (a) Membrane potential (V). (b) Intracellular calcium concentration (Ca). (c) I_s (*inward*) and I_{KCa} (*outward*). (d) I_h (*inward*), I_{HVA} (*inward, dashed line*), I_A (*outward, solid line*), and I_K (*outward, dashed line*).

Analogous to the subthreshold oscillation case, we analyzed the dependence of g_s and g_{KCa}

on oscillatory solutions by plotting bifurcation diagrams. In this case, it was found that the parameter regime supporting stable oscillations was wider than in the subthreshold case (Fig. 4.1.3a), and that there appeared to be non-linear dependence between g_s and g_{KCa} in the two parameter continuation of periodic solutions of fixed period (Fig. 4.1.3b). In Figure 4.1.3c, we show the solutions of fixed period in the $V - Ca$ plane to demonstrate the dependence of Ca on the parameters g_s and g_{KCa}. Note that by inspecting these solutions, we can exclude certain parameter tuples (g_s, g_{KCa}) that cause the solution of Ca to exceed its physiological upper bound of $1\mu M$.

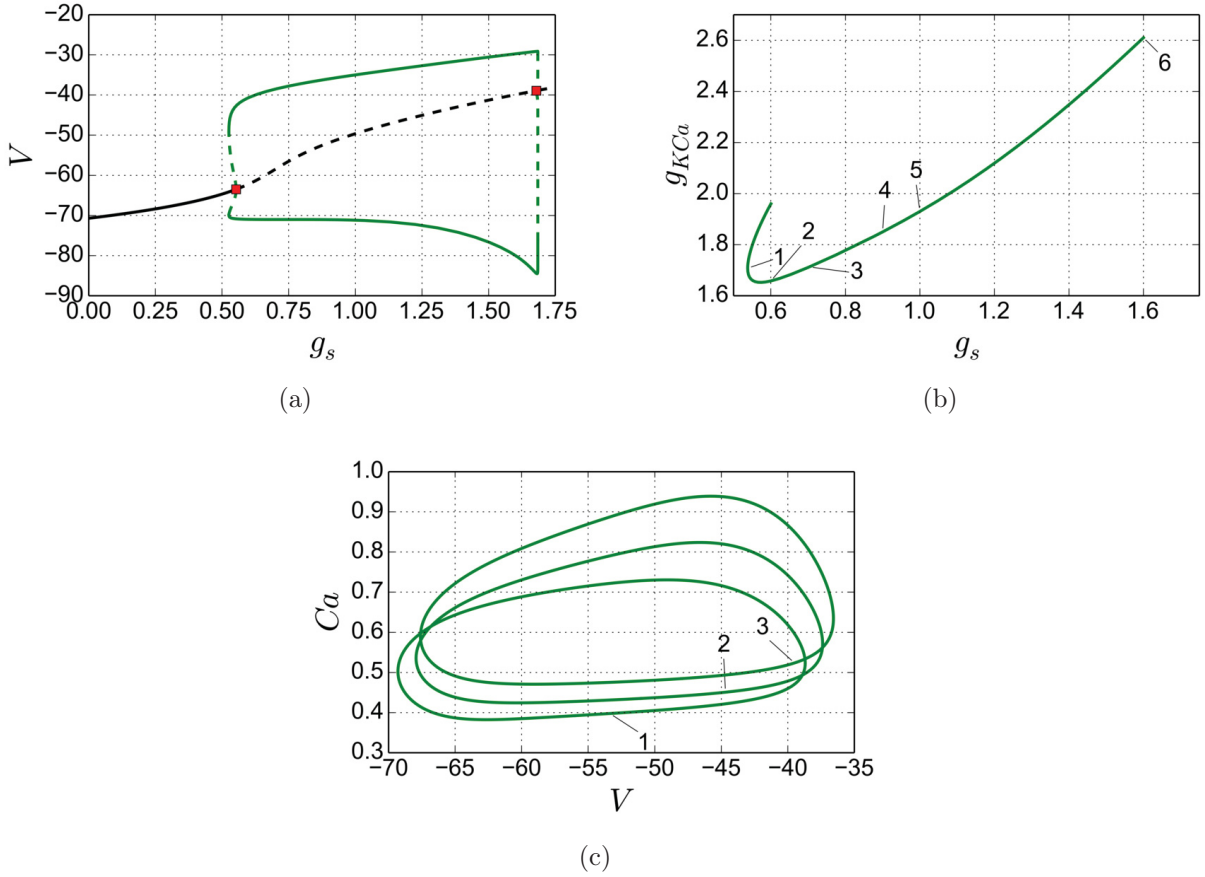

Figure 4.1.3: Parameter dependence of TTX-induced oscillations. Line colors and styles can be interpreted in the same way as in Fig. 3.4.2. (a) One parameter bifurcation of V vs. g_s. Two subcritical Hopf bifurcations (*red squares*) connect a family of periodic orbits. Stable periodic solutions (*solid green*) increase in amplitude with increasing g_s. (b) Family of periodic solutions with fixed period $T = 20$ s as a function of g_{KCa} and g_s. (c) Fixed period solutions in the V vs. Ca plane at the parameter values specified by the points "1-3", labeled in panel (b).

Returning to the case of bursting (i.e., when Na^+ currents are active), action potentials are initiated as the population of Na^+ channels is recruited during the slow depolarization of

the membrane. The channels that conduct the large-amplitude I_{NaF} begin to transition from the deactivated (C) state to the open (O) state of Fig. 3.1.3 according to the voltage-dependent rate $\alpha(V)$, which increases with depolarization. A weaker contribution from the persistent sodium current I_{NaP} also contributes to the formation of action potentials, but is not necessary for generating bursting activity. However, it was found that increasing the conductance of I_{NaP} decreases the minimum interspike interval and the amplitude of the spike AHP within the active phase of the burst. As suggested by Figure 4.1.2, spiking activity during parabolic bursting is also dependent on the currents I_K and I_{HVA}. For instance, increasing the conductance of I_K increases the amplitude of spike AHPs, and increasing the magnitude of the parameter k of $m_{K,\infty}$ (i.e., reducing the steepness of the steady-state activation curve of I_K) increases the minimum interspike interval within the burst. Meanwhile, decreasing the conductance of I_{HVA} allows for longer active phase duration due to a decrease in Ca^{2+} flux through HVA Ca^{2+} channels during the burst. This ultimately leads to reduced activation of the current I_{KCa}, and thus a delay in the termination of the burst.

4.2 Irregular bursting

Due to the irregularity in interburst interval and active phase duration observed during this type of bursting (e.g. Fig. 4.2.1a), it was assumed during model development that intrinsic noise was present in the system. Furthermore, we required that the deterministic version of the irregular bursting model (i.e., when $D = 0$) to be non-spiking and have a stable resting equilibrium, based on the hypothesis that long interburst intervals observed experimentally are caused by a tendency of the system to relax towards its resting state for average noise amplitudes. These two requirements led to an irregular bursting model where the noise term $\eta(t)$ was governed by the OU process (2.1.8), and the conductance parameters assumed the values from the set g_{irr} in Table A.3. By comparing the parameter sets g_p and g_{irr}, we see that stability is achieved in the irregular bursting model primarily through changes in the conductances g_s, g_{KCa}, and g_K. The reductions in g_s, g_{KCa} relative to the parabolic bursting model eliminated the oscillatory behaviour but still allowed for clusters of action potentials to be generated in the presence of noise. Similar to the parabolic bursting model, the parameter g_K was adjusted to produce an AHP amplitude consistent with that observed experimentally. Specifically, g_K was set to 150 nS to produce an AHP amplitude of -10 mV. In Figures 4.2.1a,c we compare recordings of membrane potential in GnRH neurons exhibiting irregular bursting with model simulations. Beneath each plot we also show the

ISI profile from a representative burst (Figs. 4.2.1b,d). Comparing the data in Figs. 4.2.1b and 4.2.1d, we observe a difference in the ISI curves at the start of the burst, but a common increase in ISI towards the end of the burst. Despite these differences, however, a biphasic ISI curve similar to that in Fig. 4.2.1d has been observed in a recording by Chu et al. [10].

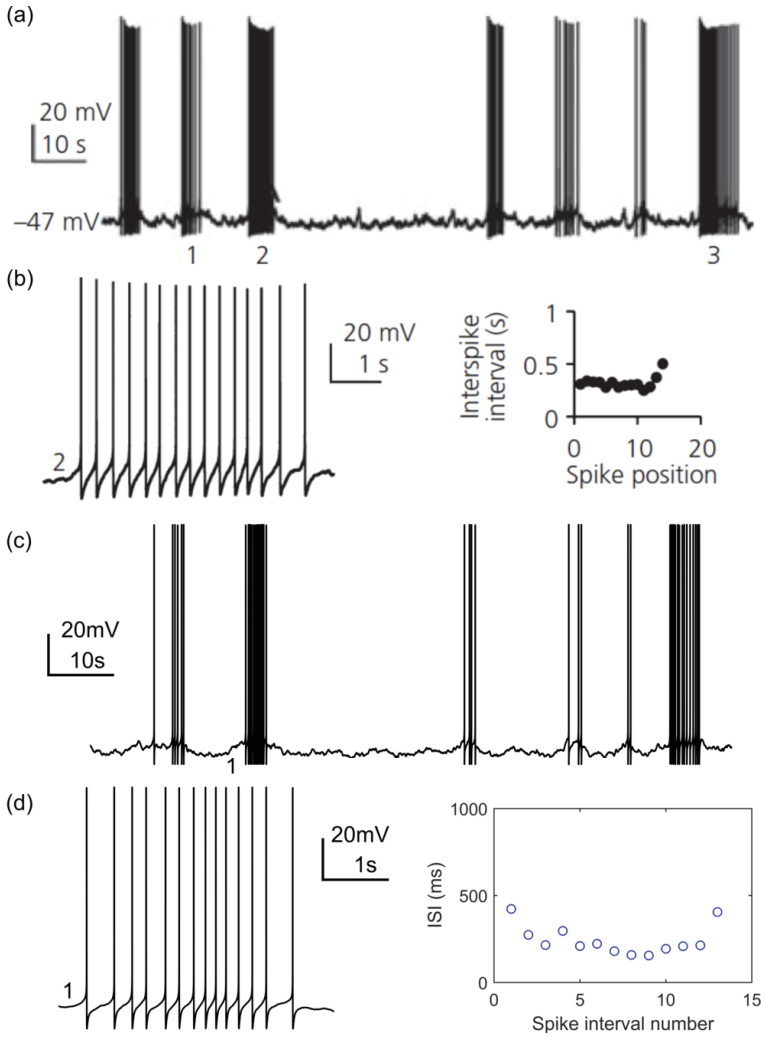

Figure 4.2.1: Irregular bursting in GnRH neurons. (a) Experimental recording of membrane potential. (b) Higher resolution view of the burst labeled "2" in panel (a) followed by ISI profile for that burst. (c) Stochastic simulation ($D = 1.0$) of membrane potential. (d) Same information as (b) but for the model-generated burst labeled "1" in panel (c).

Although we enforced that the deterministic model has a stable resting equilibrium with the parameter set g_{irr}, it was not necessary for generating irregular bursting behaviour. In fact, by selecting a parameter set that generates tonic (continuous) spiking in the absence of noise, we were able to recover irregular bursting once noise was introduced back into the system. Adopting the terminology in [67], we refer to the tonic spiking state in the deterministic model

as *superthreshold*, while the stable resting state as *subthreshold*. In other words, we are able to generate irregular bursting in two distinct fashions; namely, through the introduction of noise into the subthreshold (Fig. 4.2.2a) and superthreshold models (Fig. 4.2.2b). The superthreshold state can be obtained from the parameter set g_{irr} by decreasing g_{KCa}. In Figure 4.2.1 we show that irregular bursting initiated via the superthreshold state leads to increased excitability relative to bursting obtained from the subthreshold state. The increase in excitability is consistent with the experimental results of Liu et al. [17] who showed that excitability in GnRH neurons can be increased when I_{KCa} is blocked by the pharmacological agent apamin. The results from Figure 4.2.2 suggest that the modulation of excitability via g_{KCa} is a possible mechanism for the slow modulation of mean firing rate that occurs on the time order of hormone release, as observed by Nunemaker et al. [15].

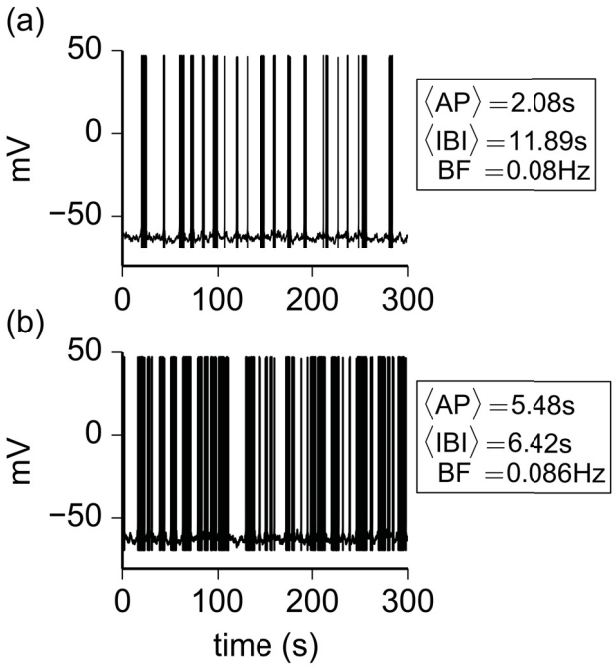

Figure 4.2.2: Comparison of excitability in model simulations of irregular bursting, as determined by the maximum conductance parameter g_{KCa}. Bursting simulations generated from (a) the subthreshold state ($g_{KCa} = 1.23$ nS) and (b) the superthreshold state ($g_{KCa} = 0.95$ nS).

The model for irregular bursting was also consistent with that observed experimentally [28, 1] in that transients in intracellular Ca^{2+} concentration peak at approximately 10% of their baseline values and persist after the termination of the active phase of the burst (Fig. 4.2.3). The correspondence with the model simulations in [1] is intriguing as it suggests that the generation of irregular bursting does not require a two-compartment model of intracellular Ca^{2+}, nor does it need the presence of the UCL2077-sensitive current $I_{AHP-UCL}$ in the

model—two important features of the model in [1]. Further similarities in the dynamics of these two models are revealed in Section 4.3 when conducting the slow-fast subsystem analysis.

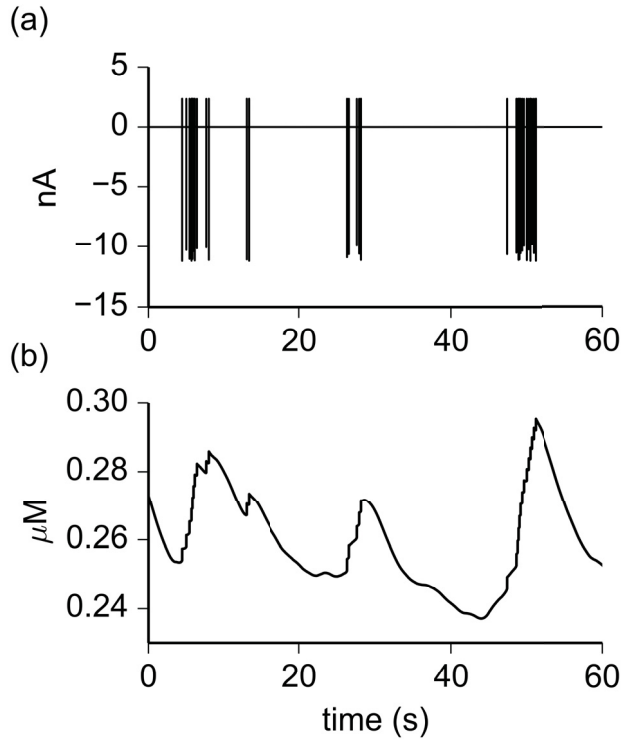

Figure 4.2.3: Simulations of action currents (sum of all ionic currents) and intracellular Ca^{2+} (Ca) generated by the irregular bursting model. (a) Action currents showing similar profile to that of membrane potential during bursting and (b) plot of Ca aligned with the time axis in (a) to demonstrate latency in Ca transients.

Given that the stochastic variable η is required to generate irregular burst patterns in the model, we inspected the time course of η separately to understand why bursting occurs in the presence of noise. Since the equation for $\dot{\eta}$ (2.1.8) does not depend on other model variables, its time series can be thought of as an independent external stimuli to the system. The long correlation time of η allows for sustained intervals of positive stimuli within the system, which generate positive feedback from other depolarizing currents in the model to initiate bursts. Similarly, periods of quiescence correspond to periods of lower values of η, during which the full model trajectory does not cross the threshold for spike initiation. The effect of η on the total ionic current in the irregular bursting model is shown graphically in Figure 4.2.4a, demonstrating that spikes in ionic current during an active phase correspond with periods of elevated η. In contrast, Figure 4.2.4b shows the effect of replacing $\eta(t)$ in the voltage equation (3.1.2) with a Gaussian white noise process $\xi(t)$, with a similar amplitude as

$\eta(t)$. The stochastic process $\xi(t)$ does not cause spiking in the model because the fluctuations in current are too fast to allow for the activation of the slow depolarizing current I_s.

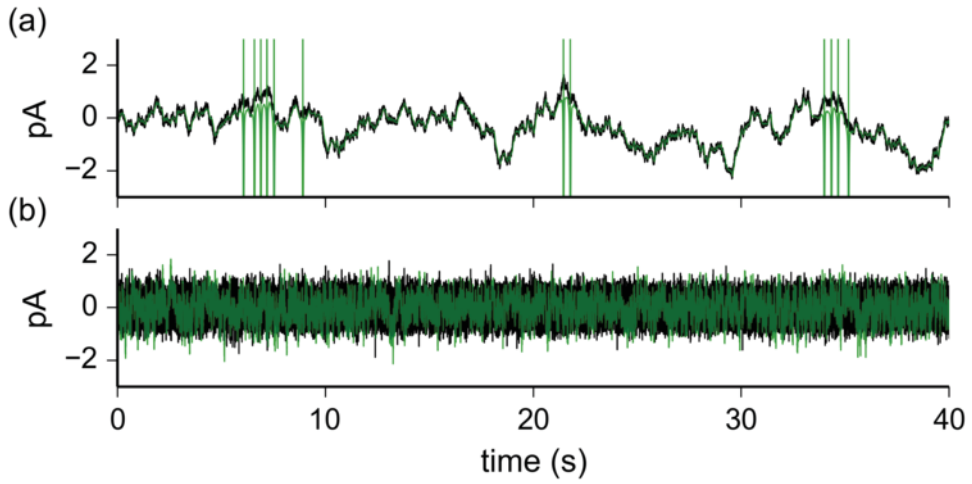

Figure 4.2.4: Representative model simulations of noise (*black*) and total ionic current (*green*). (a) Bursting simulation where noise is modelled by the OU process $\eta(t)$. Notice the (truncated) spikes in ionic current aligned with intervals of positive η. (b) Simulation using same model parameters as in (a) but now with a white noise process $\xi(t)$. In this case no spikes are fired during the simulation.

4.3 Slow-fast subsystem analysis

The GnRH neuron model developed in Chapter 3 is comprised of dynamic variables that operate on different time scales (slow and fast), and so the system is amenable to slow-fast bifurcation analysis (see Section 2.2 for a review). The purpose of this analysis is to be able to classify the type of bursting observed in GnRH neurons mathematically. By doing so, we may be able to leverage mathematical results pertaining to this classification and ultimately form new model predictions. To begin this section, we apply the slow-fast subsystem analysis on the parabolic bursting model and then repeat the analysis on the irregular bursting model. The activation variable of I_s appearing in (3.4.1), the second inactivation variable of I_{HVA} appearing in (3.2.10), and the variable Ca, were identified as slowly varying in our system based on the values of the parameters τ_{m_s}, $\tau_{h_{HVA,2}}$, and f appearing in the dynamical equations ((3.1.5),(3.1.6),(3.1.12)) for these three variables (see Table A.1 for parameter values). Based on this, the fast subsystem is then defined by the original model equations with m_s, $h_{HVA,2}$, and Ca treated as parameters. Following the methodology presented in [47], to test that the choice of slow variables was valid, we compared the slow wave generated by the parabolic bursting model with that obtained by

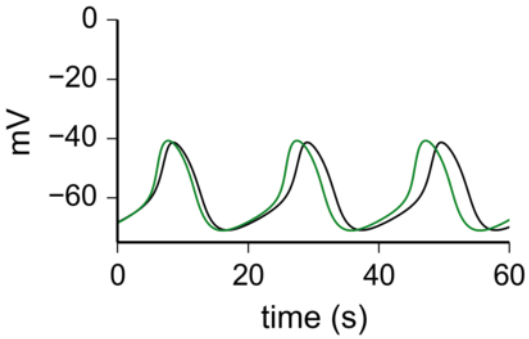

Figure 4.3.1: Comparison of the slow wave solutions generated by the full parabolic bursting model (*black*) and the four-dimensional (m_s, Ca, $h_{HVA,2}$, V) quasistatic state model (*green*).

setting all variables in the parabolic bursting model to their steady state values (except for the three slow variables, and the voltage, V). If the identification of slow variables is correct, we expect the solution of the four-dimensional system to be a good approximation to the slow wave solution of the full model. The simulations shown in Figure 4.3.1 do indeed suggest that the choice of slow variables is valid since the solutions of the four-dimensional model and the full model are in qualitative agreement.

To proceed with the analysis, we record the values of the variables m_s, $h_{HVA,2}$, Ca, and V from a selected burst cycle along a parabolic bursting trajectory. Then at selected time points t_i within the burst interval, we compute the one-parameter bifurcation diagram in the $m_s - V$ plane for the fast subsystem, by assigning $h_{HVA,2}$, and Ca (which are now treated as parameters) the values they attain at time t_i. Note that since the fast subsystem depends explicitly on each slow variable (in contrast to the situation in Section 2.2), the one-parameter bifurcation diagram is not static throughout the burst cycle, but rather is continuously shifted during the cycle (hence a *moving* bifurcation diagram). To examine next how the solution trajectory of the burst cycle in the $m_s - V$ plane evolves with respect to the moving bifurcation diagram, for each t_i we plot the phase point $(m_s(t_i), V(t_i))$ from the parabolic bursting trajectory on top of the bifurcation diagram computed in the previous step. Thus by taking sufficiently many time points t_i, we can infer what types of bifurcations are crossed in the fast subsystem upon initiation of the first spike and termination of the last spike in the active phase of the burst cycle. The results of the analysis are summarized in Figure 4.3.2, which suggests that the initiation and termination of spiking corresponds to the passage of the trajectory through a saddle-node on invariant circle (SNIC) bifurcation in the fast subsystem, while the quiescent phase of the burst corresponds to a trajectory along the lower stable branch of the equilibrium manifold. With these numerical results, we tentatively classify parabolic bursting in GnRH neurons as *Type II bursting*, according to

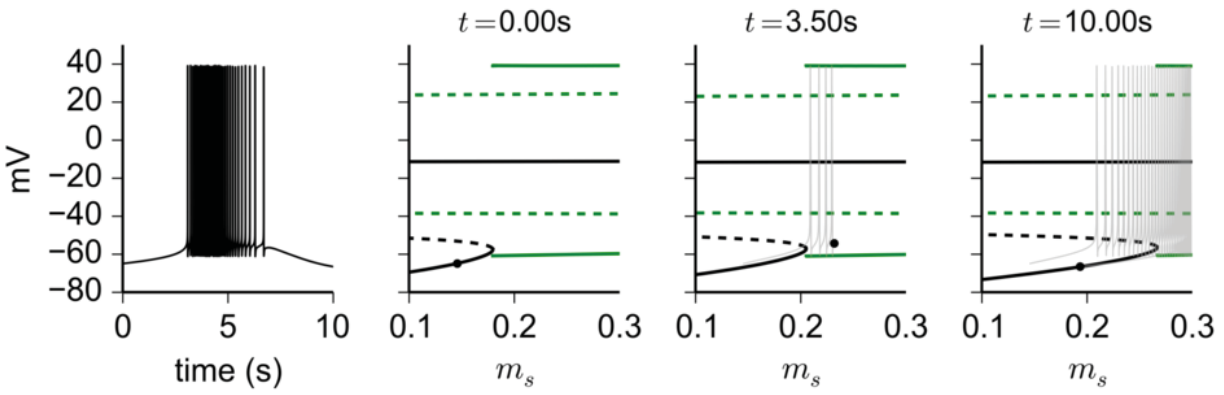

Figure 4.3.2: Slow-fast subsystem analysis of the parabolic bursting model as determined by one-parameter bifurcation diagrams in the $m_s - V$ plane, where m_s is treated as a parameter and the other slow variables $h_{HVA,2}$ and Ca are assigned the values they attained during a representative burst trajectory (*leftmost panel*). Bifurcation diagrams in the three right panels are computed at arbitrary times t during the initiation (*second panel*), active (*third panel*), and termination phases (*fourth panel*) of the burst. The thick lines in the three bifurcation diagrams represent stable and unstable branches of steady states and periodic orbits as defined in Fig. 3.4.2. The phase trajectories in the $m_s - V$ plane, up to time t, are superimposed on the bifurcation diagrams (*solid gray and black dot)* to illustrate the connection between the steady-solutions of the fast subsystem, and the full model trajectory.

the classifications by Bertram et al. [54].

To provide more numerical support for the existence of a SNIC bifurcation, a three-parameter (m_s,$h_{HVA,2}$, Ca) continuation of the saddle-node bifurcation and homoclinic bifurcation in the fast subsystem was computed and then superimposed on the full model trajectory in $(m_s, h_{HVA,2}, Ca)$ phase space. Since the continuation of these bifurcation points in three-parameter space is not feasible in `AUTO`, two-parameter (m_s, Ca) bifurcations were computed for discrete values of $h_{HVA,2}$ attained during the burst. To obtain the approximate locus of homoclinic points for each value of $h_{HVA,2}$, a two-parameter continuation of periodic orbits with fixed period $T = 1000$ ms was computed. Treating the loci of saddle-node and homoclinic points in 3-space as two surfaces of the form $h_{HVA,2} = h(m_s, Ca)$, the results were interpolated using `numpy` to obtain the smooth surfaces shown in Figure 4.3.3. Notice that spiking is initiated and terminated close to the intersection points of the trajectory with the two surfaces.

For the irregular bursting model we followed a similar procedure as above, but now with η treated as a slow variable in the fast subsystem. Justification for this treatment was based on the fact that t_c, which affects the correlation time of the OU process $\eta(t)$ defined by (2.1.8), has a value similar to the time constants of other slow variables in the model (compare parameters in Section A.2). As argued by Longtin et al. [85], η can be treated as

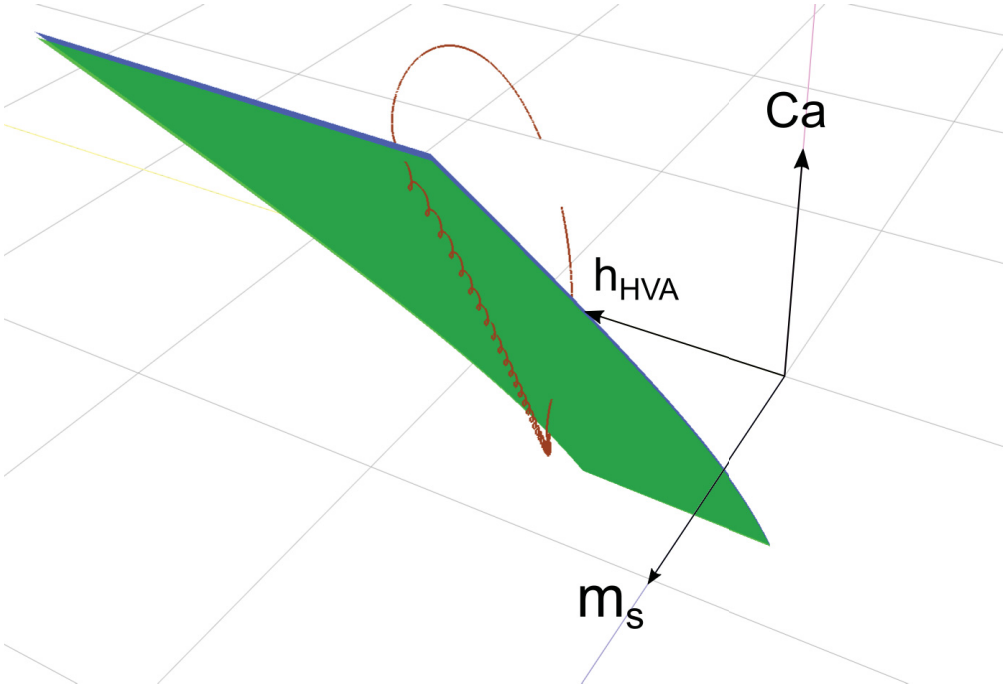

Figure 4.3.3: Three-parameter (m_s, $h_{HVA,2}$, Ca) bifurcation diagram of the fast subsystem plotted on top of full model trajectory (*red*) in phase space. Note that the surfaces of saddle-node points (*blue*) and homoclinic points (*green*) appear to coincide, suggesting the existence of a SNIC bifurcation in the fast subsystem.

quasi-constant relative to other variables in the model, which operate on faster time scales. The slow-fast subsystem analysis of the irregular bursting model not only revealed a similar bifurcation structure as in the parabolic case, but also the same mechanism for the initiation and termination of the burst. In particular, Figure 4.3.4 shows that the phase trajectory follows the locus of stable equilibria of the fast subsystem and then crosses what appears to be a SNIC bifurcation to initiate spiking. The burst is terminated when the trajectory crosses the SNIC in the opposite direction and travels along the locus of stable equilibria once again. Note, however, that once an irregular burst is terminated, a second passage through the SNIC bifurcation in the fast subsystem can be accelerated or delayed depending on the time course of η. This gives rise to the variation in interburst interval that is evident from the simulation in Fig. 4.2.1.

4.4 Minimal bursting model

With the tentative classification of both parabolic and irregular bursters as Type II [54], we sought to reproduce the two types of bursting in a canonical/minimal model for *circle-circle* bursting, that is, bursting where the initiation and termination of the active phase involves

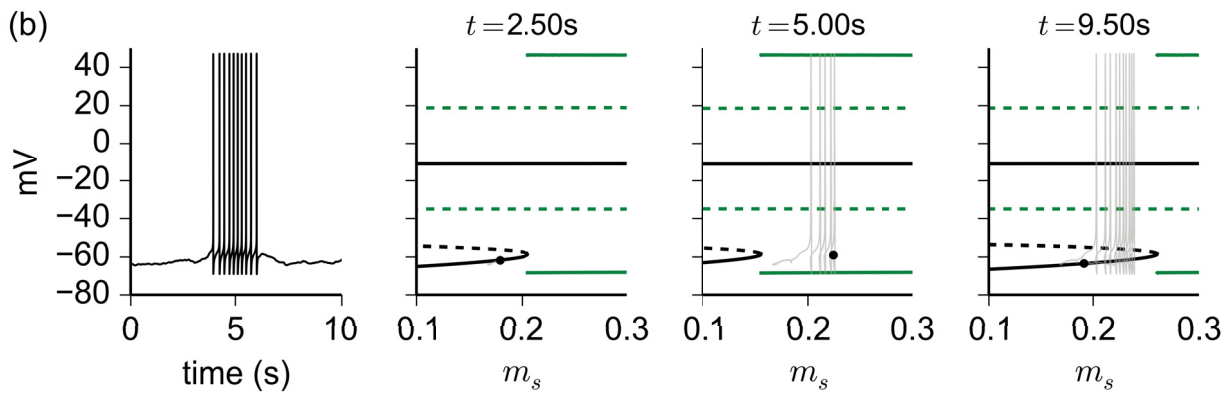

Figure 4.3.4: Same analysis as (4.3.2) but with additional slow variable η. The bifurcation diagrams computed for the three different phases of the trajectory show similar structure as in the parabolic case. Note that the lower stable stationary branches (*solid black*) are flatter than in the parabolic case, which explains why the irregular burster doesn't undergo large amplitude hyperpolarizations after spiking has terminated.

passage through a SNIC bifurcation in the fast subsystem [48]. This minimal model, which is based on previous work by Izhikevich [86], is three-dimensional (in the deterministic case), and as a result the derivation of analytical results is more feasible compared with the model presented in Chapter 3. Furthermore, numerical solutions can be computed faster which may have a noticeable effect if simulating networks of synaptically coupled cells. In this section, we present the model that first appeared in [86], to show that it is capable of recreating the desired qualitative behaviour, and to derive some basic results.

The modified canonical model for circle-circle bursting is a type of QIF model given by the set of equations

$$\begin{aligned} \dot{v} &= I + a(v - v_b)^2 + bu_1 + \eta(t) \\ \dot{u_1} &= -\mu_1 u_2 \\ \dot{u_2} &= -\mu_2(u_2 - u_1), \quad \mu_2 < 4\mu_1, \quad \mu_1, \mu_2 \ll 1 \end{aligned} \tag{4.4.1}$$

$$v \to v_r,\ (u_1, u_2) \to (u_1 + d_1, u_2 + d_2), \quad \text{when } v = v_p,$$

where η is the same OU process as defined in Section 2.1. According to (4.4.1), the variables v, u_1, and u_2 are reset when v attains its arbitrarily set peak value v_p, where the reset is determined by parameters v_r, d_1, and d_2. The set of equations in (4.4.1) is modified from that of [86] by the use of the terms $a(v - v_b)^2$ vs. v^2, bu_1 vs. u_1, and the inclusion of the stochastic variable η in the equation for v. With v representing membrane potential and t the time in seconds, the additional parameters a, b and v_b are convenient for achieving closer

correspondence of v with the bursting observed experimentally. For example, increases in a decrease interspike interval during spiking, b affects the amplitude of repolarization during the quiescent phase, whereas v_b controls the voltage threshold for spike initiation. Using the appropriate parameters (see Table A.4), model (4.4.1) generates qualitatively similar burst patterns as those obtained by detailed model, as shown in Figure 4.4.1. Note that the original canonical model [86] is dynamically equivalent to (4.4.1), when $\eta = 0$, by the change of variables $\tau = at$, $\tilde{v} = v - v_b$, $\tilde{u}_i = \frac{b}{a}u_i$.

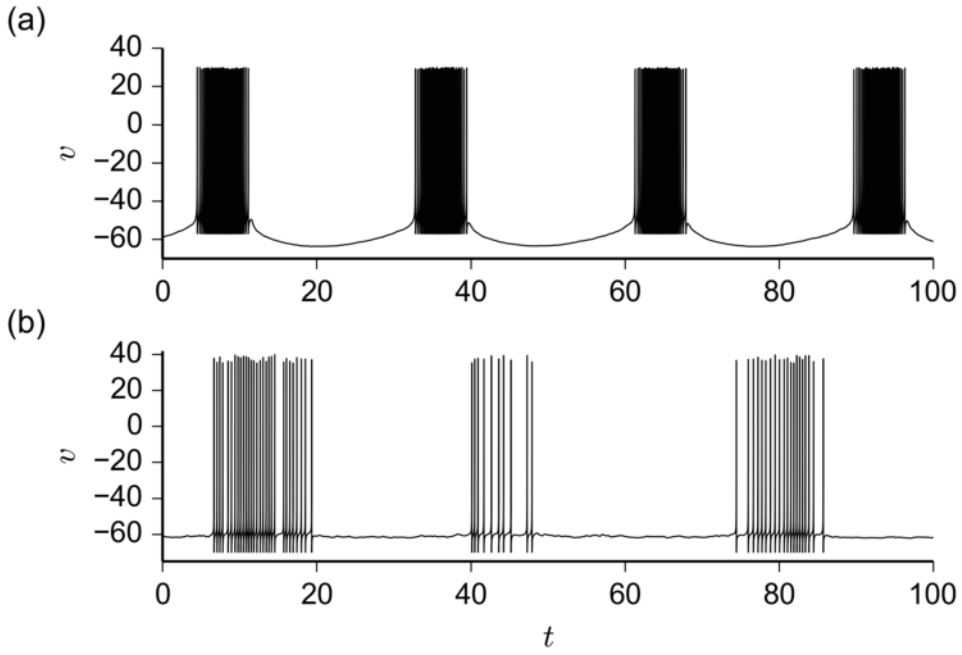

Figure 4.4.1: Two types of bursting simulated by the reduced model (4.4.1) in the presence of noise η. (a) Parabolic bursting simulation. (b) Irregular bursting simulation. Both types of bursting agree qualitatively with the model simulations in Sections 4.1 and 4.2.

To explain how parabolic bursting arises in the reduced model, we follow the approach of Sections 2.2 and 4.3, and decompose the model into fast and slow subsystems, with the temporary assumption that $\eta = 0$. The slow subsystem in (4.4.1) is comprised of the dynamical equations for the variables u_1 and u_2. Selecting μ_1 and μ_2 so that $\mu_2 < 4\mu_1$, the equations for u_1 and u_2 form a slow subsystem whose equilibrium is a stable focus. However, if $\mu_2 > 4\mu_1$, the equilibrium of the slow subsystem is a stable node, in which case (4.4.1) can be transformed into an alternate canonical model for circle/circle bursting [86]. Meanwhile, the fast subsystem is one-dimensional, consisting of one equation for $\dot{v}$, since u_1 is now treated as a parameter. To show that the fast subsystem possesses a saddle-node bifurcation, we

solve for the equilibrium points of v:

$$v_{\pm} = v_b \pm \sqrt{-\frac{(I + bu_1)}{a}}. \tag{4.4.2}$$

Thus when $\tilde{I} \equiv I + bu_1 = 0$, the two equilibria coalesce into the saddle-node equilibrium $v = v_b$. When $\tilde{I} > 0$ the equilibrium disappears and the fast variable v blows up in finite time to $+\infty$, an outcome that is prevented by enforcing the reset condition $v \to v_r$ when $v = v_p$. Since we still have that $\tilde{I} > 0$ after the reset, repeated application of the reset condition occurs and periodic spiking is observed. With this understanding of the fast dynamics, we can now describe how bursting occurs in the full model. Before the first spike is initiated, $\tilde{I} < 0$ and the trajectory follows the stable equilibrium manifold $v(u_1, u_2) = v_b - \sqrt{-\frac{(I+b_1u_1)}{a}}$ (Fig. 4.4.2a). Once the saddle-node bifurcation is crossed in the fast subsystem, spiking persists until u_1 is such that $\tilde{I} < 0$. The system allows for the firing of multiple spikes due to the reset conditions on u_1 and u_2, which delay the crossing of the line $u_1 = -\frac{I}{b_1} \equiv u_*$ in the phase space of the slow variables u_1 and u_2 (Fig. 4.4.2b).

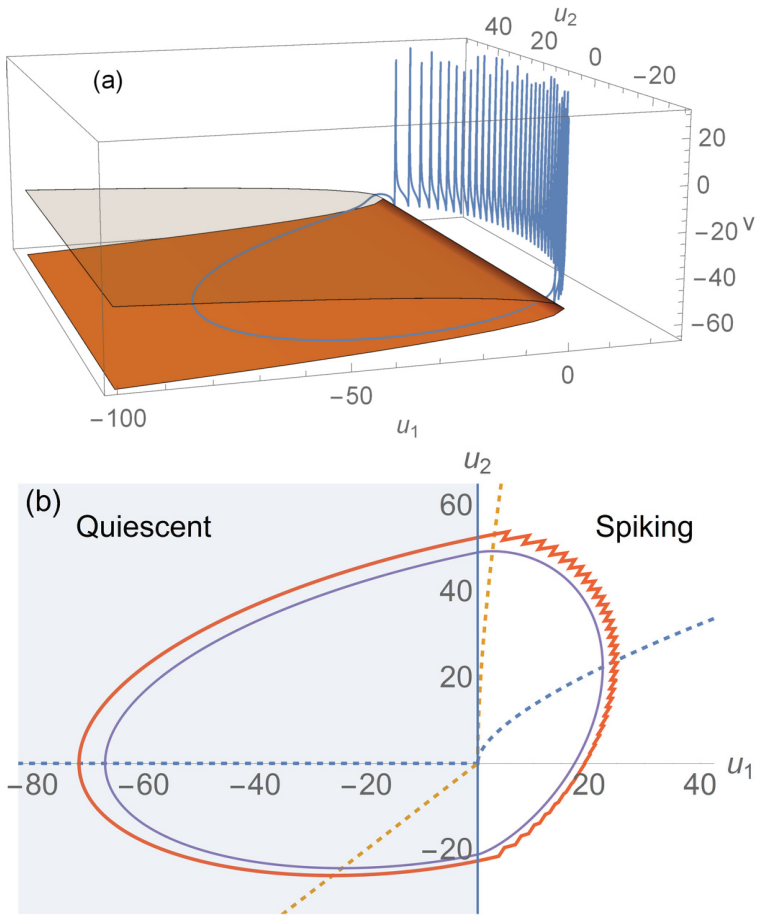

Figure 4.4.2: Phase plane analysis for one burst cycle generated by the parabolic bursting model (4.4.1). (a) The solution (*blue*) in the full phase space follows the stable equilibrium manifold (*orange*) during the quiescent phase of the burst, while the spiking phase occurs off the manifold. (b) Solution in the $u_1 - u_2$ plane (*orange*) plotted against the solution (*purple*) and nullclines (*blue-dashed, yellow-dashed*) of the averaged slow subsystem, as determined by Eq. (4.4.3).

To obtain some analytical results, we first rewrite the set of equations in (4.4.1) in the singularly perturbed form

$$\begin{aligned} \dot{v} &= f(v,u) \\ \dot{u} &= \mu g(v,u), \quad \mu \ll 1, \end{aligned}$$

where $u = (u_1, u_2)$ and μ is a small parameter. Following the methodology in [87], the smooth trajectory and nullclines plotted in Figure 4.4.2b are obtained through a change of variables $z = u + \mathcal{O}(\mu)$ as determined by the solution of the averaged slow subsystem,

$$\dot{z} = \frac{\mu}{T(z)} \int_0^{T(z)} g(v(t,z),z)\, dt, \tag{4.4.3}$$

where $v(t,z)$ is the periodic spiking solution of the fast subsystem, and $T(z)$ is the period of spiking as a function of $z=(z_1,z_2)$. When $u_1 \leq u_*$, the averaged system is equal to the original system. However, when $u_1 > u_*$ we have

$$g(v(t,z),z) = \begin{pmatrix} -\mu_1 z_2 + d_1\delta(T) \\ -\mu_2(z_2-z_1) + d_2\delta(T) \end{pmatrix}$$
$$\implies \dot{z} = \begin{pmatrix} -\mu_1 z_2 + \frac{d_1}{T(z)} \\ -\mu_2(z_2-z_1) + \frac{d_2}{T(z)} \end{pmatrix}.$$

Fortunately, we can obtain the period $T(z)$ analytically by solving the fast subsystem during a single spike:

$$\int_{v_r}^{v_p} \frac{dv}{\tilde{I} + a(v-v_b)^2} = \int_0^T dt$$
$$\implies T(z_1) = \frac{\kappa}{\sqrt{z_1-u_*}} \left\{ \arctan\left[\frac{a\kappa}{\sqrt{z_1-u_*}}(v_p-v_b)\right] - \arctan\left[\frac{a\kappa}{\sqrt{z_1-u_*}}(v_r-v_b)\right] \right\},$$

where $\kappa = \sqrt{\frac{1}{ba}}$. Solving for the nullclines we obtain

$$z_1\text{-nullcline: } z_2 = \begin{cases} 0, & u_1 \leq u_* \\ \frac{d_1}{\mu_1 T(z_1)}, & u_1 > u_* \end{cases} \tag{4.4.4}$$

$$z_2\text{-nullcline: } z_2 = \begin{cases} z_1, & u_1 \leq u_* \\ z_1 + \frac{d_2}{\mu_2 T(z_1)}, & u_1 > u_*. \end{cases} \tag{4.4.5}$$

On a practical note, in Figure 4.4.2b there is a noticeable error between the solution of the averaged slow subsystem and the solution of the full model in the $u_1 - u_2$ plane. This discrepancy is a result of the choice of μ_1 and μ_2 used for the particular simulation, which were selected to obtain qualitative agreement with the parabolic bursting simulations in the biophysically detailed model, but are still somewhat large. Using smaller values of μ_1 and μ_2, the solution for v loses qualitative agreement with that of the detailed model, but the solution of the averaged slow subsystem gets closer to that of the full system. Although the parameter space was only explored manually, the fact that μ_1 and μ_2 require "intermediate" values to obtain the correct bursting behaviour suggests an intermediate separation of timescales in the detailed model as well. Nonetheless, in both the minimal and detailed models, the transition from quiescence to spiking during bursting corresponds closely with the passage of a SNIC bifurcation in the fast subsystem, indicating that for the purposes of bursting classification,

the separation of timescales is sufficiently large.

Up to this point, the analysis of the minimal model has focused on deterministic parabolic bursting. Now we consider the effect of the stochastic process $\eta(t)$ and explain how irregular bursting is generated in the minimal model. Analogous to the detailed model, irregular bursting occurs when enabling noise from a subthreshold steady-state. Therefore, we choose the initial condition for the irregular bursting simulations to be $(v_b - \sqrt{-\frac{I}{a}}, 0, 0, 0)$. Starting from this point with a sufficiently high noise intensity, the slow variable η will push the system past the threshold for firing in the fast subsystem. Once a spike is fired, $u = (u_1, u_2)$ is activated via the reset condition, which may trigger further spikes. After the termination of the burst, an interval of elevated η may lower the threshold for firing as u spirals towards the origin (the stable steady state of the slow subsystem), triggering another cluster of spikes as shown in Fig. 4.4.3b. This can be understood by recalling that the threshold for firing in the fast subsystem is crossed when $\tilde{I} = bu_1 + I + \eta > 0$. In this case, the quiescent phase of the burst cycle is interrupted leading to a "short" interburst interval. "Long" interburst intervals, on the other hand, occur when an interval of decreased η forms after the burst (e.g. Fig 4.2.4a), which prevent u from triggering another set of spikes as it spirals towards the origin. This interaction between u and η persists to sustain an irregular bursting pattern as $t \to \infty$. Although the steady-state behaviour is only predicted by integrating the system for long enough times, we would expect that with a sufficiently high noise intensity D in (2.1.11), the system will always be able to initiate a spike to reactivate u and generate irregular burst patterns. In other words, such behaviour is not transient, but rather persistent in the presence of noise.

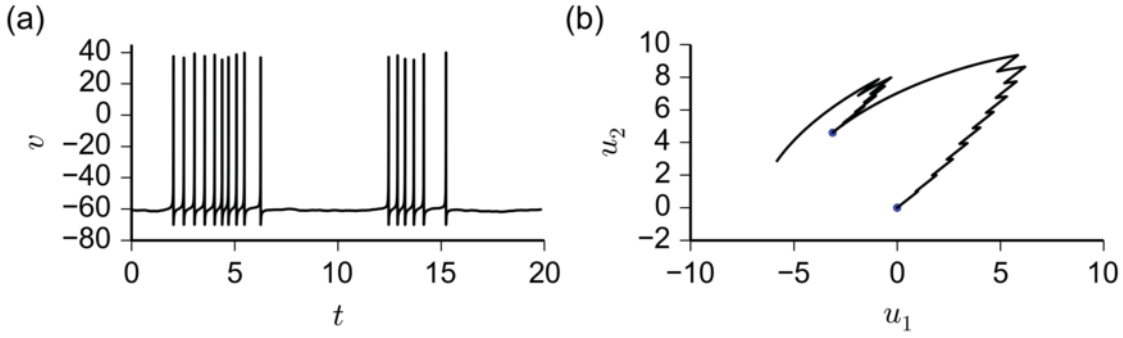

Figure 4.4.3: Simulation of irregular bursting in the minimal model starting from a subthreshold state. (a) Solution $v(t)$ showing two clusters of spikes separated by a "short" interburst interval. (b) Each cluster of spikes in (a) is initiated from a different value of u (*blue markers*) because the threshold for firing also depends on η.

Chapter 5

Summary and conclusion

At the time of writing this thesis, there remains an intense focus on deciphering the mechanisms underlying bursting behaviour in GnRH neurons, and ultimately, the connection between burst firing and hormone release. Indeed, the body of literature concerned with the modelling of bursting activity in GnRH neurons is growing rapidly. As indicated by the literature review in Chapter 1, several GnRH neuron models have a common lineage tracing back to the seminal studies by Van Goor et al. [33] and Lebeau et al. [34], in which neuronal models are developed for describing electrical excitability in the GT1 cell line. A common approach in recent models [35, 36, 1, 39, 41] is to construct a submodel consisting of currents that are adapted from the set of "GT1 currents" $\{I_{NaF}, I_K, I_M, I_{Kir}, I_{CaL}, I_{CaT}\}$ modelled by Van Goor et al. [33] and Lebeau et al. [34]. For instance, in the bursting models by Duan et al. [1] and Chen et al. [39], the submodel consisting of GT1 currents is extended by adding currents such as the persistent Na^+ current I_{NaP} (from Roberts et al. [35]), the small-conductance Ca^{2+}-activated K^+ (SK) current (denoted I_{KCa} in the present model), and others. In contrast with several of the models reviewed in Chapter 1, that developed in Chapter 3 does not assume that the models for the GT1 currents are valid for use in a GnRH neuron model. Instead, the present model includes revisions to a subset of the GT1 current models based on recent voltage- and current-clamp data obtained from whole-cell recordings of GnRH neurons in brain slices of mice.

The results obtained from fitting the currents in the set $S = \{I_{NaP}, I_K, I_A, I_{HVA}, I_{LVA}, I_h\}$ to voltage-clamp recordings are shown in Section 3.2.4. The fast Na^+ current I_{NaF}, crucial for the generation of action potentials, was not fit to voltage-clamp data but rather to current-clamp data. As described in Section 3.3.3, the current I_{NaF} was parameterized in the context of the full model. In brief, we used the genetic algorithm to search for parameter values of the I_{NaF} submodel that minimize the error between model simulations

and recordings of spiking trajectories in the $(V, \dot{V})$ phase plane. We remark that for the purposes of simplifying the model, the K^+ currents I_M and I_{Kir}, shown to be conducted in GnRH neurons (see Table 1.1), were excluded. The current I_M was excluded because it is assumed to be captured implicitly by the I_K model, whereas I_{Kir} was excluded because its contribution is most significant in the voltage regime hyperpolarized relative to the reversal potential E_K [88], and electrical activity in this regime was not studied in this thesis. Models for these two currents, adapted closely from Roberts. et al. [35], were tested in the model and were not found to affect the ability of the model to simulate parabolic and irregular bursting.

In addition to the ionic components described above, the model also includes the SK current I_{KCa}, a slow inward Ca^{2+} current I_s, and a single-compartment model for Ca, the intracellular Ca^{2+} concentration. The subsystem consisting of these three components was essential for sustaining endogenous, rhythmic electrical activity; namely, subthreshold oscillations (shown in Section 3.4.2), and parabolic and irregular bursting (shown in Sections 4.1 and 4.2). Whereas the existence of the SK current I_{KCa} in GnRH neurons is well-established [17, 28], there is currently no voltage-clamp data to support the inclusion of I_s in the model. The rationale for including the current I_s, however, is based on two key observations: (i) that the other ionic currents in the model (in the absence of I_s) do not appear to possess the kinetic properties required for generating oscillations with a period of approximately 20 s as observed experimentally, and (ii) that the Plant model for parabolic bursting, which possesses a similar I_s, I_{KCa}, Ca subsystem, reproduces several characteristics of the parabolic bursting exhibited by GnRH neurons, including a statistically significant correlation between the active phase duration and the subsequent quiescent phase of the burst [10]. The agreement between model simulations and experimental recordings of parabolic and irregular bursting, demonstrated in Chapter 4 (specifically by Figs. 4.1.1, 4.2.1, 4.2.2, and 4.2.3) provide further support for the inclusion of I_s. At the very least, even if I_s cannot be isolated experimentally, the model simulations shown in this thesis demonstrate that the I_s, I_{KCa}, Ca subsystem is a reasonable abstraction of a more complex rhythm generating mechanism in GnRH neurons.

Finally, we suggest how the proposed model might be extended in future research efforts. A logical extension of the model is to account for the morphology of the GnRH neuron by using either (i) a detailed multicompartmental model consisting of many compartments, similar to that of Roberts et al. [35], (ii) a simplified three compartment (two dendrite, one soma) model, similar to that of Csercsik et al. [37], or (iii) a continuous cable model similar to that of Chen et al. [39]. The most appropriate choice of formalism will depend on the goals of the modelling study. For example, a modelling study that aims to predict

the synchronization properties of a simple network of GnRH neurons connected synaptically will likely adopt formalism (ii) or (iii) for the purposes of computational efficiency. On the other hand, a realistic modelling study that aims to predict the effects of dendrites on parabolic and irregular bursting in a single GnRH neuron will likely adopt formalism (i). We also remark that the minimal GnRH neuron model presented in Section 4.4 is a good candidate for large-scale simulations of networks of bursting GnRH neurons. In conclusion, we predict that the bursting models presented in this thesis will serve as a framework for more sophisticated studies of intrinsic electrical activity in GnRH neurons.

Appendix A

A.1 AUTO configuration files

The following sections of code are working configuration (`c.*`) files that were used to setup AUTO for computing the various bifurcation diagrams that appear in the main text. They provide a useful starting point for researchers studying parameter dependency in neuronal systems.

A.1.1 Periodic branches (slow-fast subsystem analysis)

```
unames={1:'v'}
parnames={1:'hhvas',2:'ms',3:'ca',4:'MIN␣v'}
NDIM= 16, IPS = 2, IRS = 0, ILP = 0
ICP = ['ms',11,'MIN␣v']
NTST= 70, NCOL= 4, IAD = 3
ISP = 1, ISW = 1, IPLT= 0, NBC= 0, NINT= 0
NMX= 5000, NPR= 1000, MXBF= 10, IID = 2
ITMX= 8, ITNW= 5, NWTN= 3, JAC= 0
EPSL= 1e-07, EPSU = 1e-07, EPSS = 1e-05
DS = 0.1, DSMIN= 1e-05, DSMAX= 1000.0, IADS= 1
NPAR= 14, THL = {}, THU = {}
UZSTOP={11:1e5}
```

A.1.2 Two parameter continuation of fixed period orbits

```
unames = {1:'v',19:'ca'}
parnames = {1:'gs',2:'gkca',3:'MIN␣v',4:'AMP␣v'}
NDIM= 19, IPS = 2, IRS = 0, ILP = 1
ICP = [1,2,3]
```

```
NTST= 100, NCOL= 4, IAD = 3
ISP = 2, ISW = 1, IPLT= 0, NBC= 0, NINT= 0
NMX= 200, NPR= 200, MXBF= 5, IID = 2
 ITMX= 8, ITNW= 5, NWTN= 3, JAC= 0
EPSL=1e-7, EPSU=1e-7, EPSS=1e-5
DS = 0.01, DSMIN= 1e-5, DSMAX= 1.0, IADS= 1
NPAR= 14 , THU = {}
UZR={1:0.5,1:0.6,1:0.7,1:0.8,1:0.9:,1:1.0}
UZSTOP={1:5.0}
PAR={11:1.5e4}
```

A.2 Parameter sets

A.2.1 Detailed model

Parameters for the GnRH neuron model appearing in Section 3.1 are listed here. The maximum conductances parameters in Table A.3 are those that are changed to generate the various electrical phenomena. Note that all parameters not listed in Table A.3 remain static when generating the different electrical phenomena unless otherwise noted in the main text.

HH gating parameters:

	I_{NaP}		I_A			I_K	I_{LVA}		I_{HVA}			I_s	I_h	
	m	h	m	h_1	h_2	m	m	h	m	h_1	h_2	m	h_1	h_2
p	1	—	1	—	—	4	2	—	1	—	—	1	—	—
f_i	—	1	—	0.8	0.2	—	—	1	—	0.2	0.8	—	0.364	0.636
V_h (mV)	-41.5	-47.4	-15	-69	-69	15	-56.1	-80	-11	-32	-32	-45	-77.45	-77.45
k (mV)	-3.0	8.2	-11	6	6	-9	-10.7	4.7	-7	11	11	-12	9.22	9.22
$\tau(V)$ (ms)	0.4	τ_2	τ_2	30	500	τ_2	τ_2	20	τ_2	45	950	1500	τ_1	τ_1
a	—	67.3	-40	—	—	-43	50	—	20	—	—	—	-89.8	-82.6
b	—	-27.5	26.5	—	—	18.5	9	—	-10	—	—	—	11.6	25.7
c	—	67.3	43	—	—	144	50	—	20	—	—	—	35.8	370.9
d	—	27.5	-8.4	—	—	-49	-9	—	10	—	—	—	7.6	54.1
e	—	574.48	1	—	—	0.38	7	—	1	—	—	—	—	—
f	—	62.6	0.1	—	—	0	0.5	—	0.6	—	—	—	—	—

Table A.1: Kinetic parameters for currents with gating described by Equations (3.1.5) and (3.1.6). Units for time constant parameters a, b, c, d, e, f vary and are inferred from the functions τ_1 and τ_2.

Non-HH gating parameters:

I_{NaF}: $r_2 = 0.2$ ms^{-1}, $r_4 = 0.05$ ms^{-1}

	$\alpha(V)$	$\beta(V)$	$r_3(V)$
a (ms^{-1})	55	60	30
b (mV)	33	32	77.5
c (mV)	-7	10	12

Table A.2: I_{NaF} rate parameters for voltage-dependent functions

$I_{KCa} : K = 1.0\mu$M

Electrical parameters:

Capacitance: $C_m = 20$pF (experimentally observed value [19]).

	I_{NaF}	I_{NaP}	I_A	I_K	I_{LVA}	I_{HVA}	I_s	I_h	I_{KCa}	I_L
E (mV)	54	54	-101	-101	82.5	82.5	82.5	-40	-101	-65
g_{vc} (nS)	—	0.68	45	100	0.2	8	—	1	—	1
g_p (nS)	300	0.68	45	115	0.2	8	0.58	0.5	1.96	0
g_{irr} (nS)	500	0.68	45	150	0.2	8	0.18	1	1.18	0
g_{sub} (nS)	500	0.68	45	150	0.2	8	0.58	0.5	3.88	0

Table A.3: Electrical parameters for ionic currents. E is the reversal potential. The values in row g_{vc} are the maximum conductances used to fit to voltage-clamp experiments. The values in rows g_p, g_{irr}, g_{sub} are the maximum conductances used to fit to parabolic bursting, irregular bursting, and subthreshold oscillating models.

Calcium submodel parameters:

$f = 0.0025$, $k_p = 0.265$ms^{-1}, $K_p = 1.2\mu$M, $\beta = 10^6$, $V_{cyt} = 2.8$pL.

Noise:

$D = 1.0$ pA^2/ms, $t_c = 1500$ ms.

A.2.2 Minimal model

The parameters used to generate parabolic and irregular bursting in the minimal model are listed here.

	a	b	I	μ_1	μ_2	v_b	v_r	v_p	d_1	d_2	D	t_c
Irregular	5	1.2	-2	0.2	0.12	-60	-70	40	1	1	30	1.4
Parabolic	2	5	0	0.3	0.08	-50	-57	30	1	2	30	1.4

Table A.4: Parameters used for generating parabolic and irregular bursting in the minimal model (4.4.1).

A.3 Voltage-dependent curves

In Figure A.3.1 we provide plots of the (in)activation curves and voltage-dependent time constants for the gating variables of voltage-gated ionic currents in the GnRH neuron model. The purpose of this section is to serve as a visual reference for researchers studying the model. For all plots, V has units of mV while τ has units of ms. For I_{NaF} (Fig. A.3.1a), all functions have units ms^{-1}.

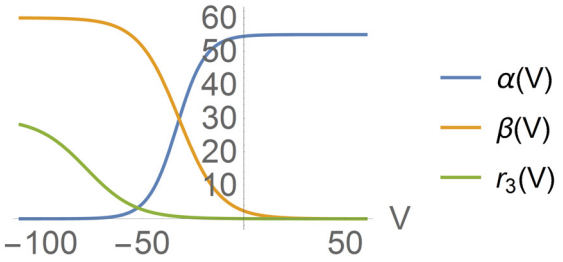

(a) I_{NaF}

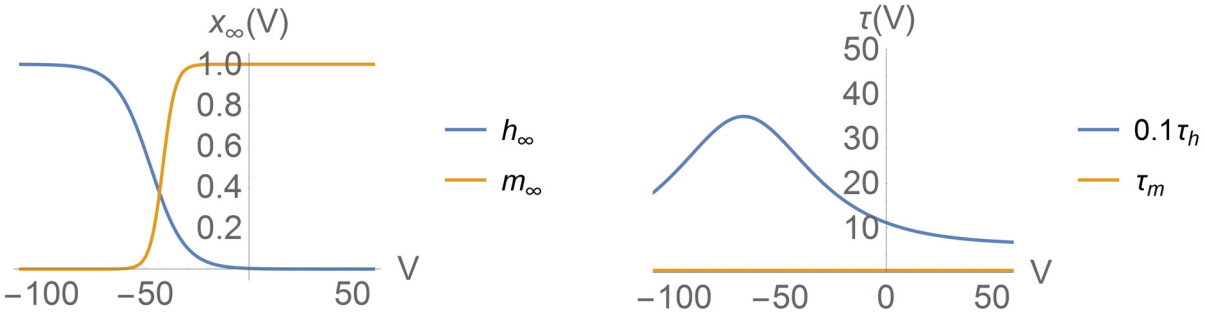

(b) I_{NaP}

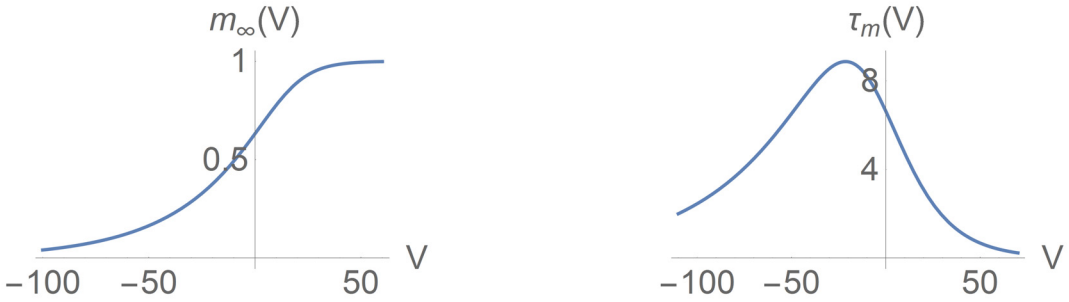

(c) I_{K}

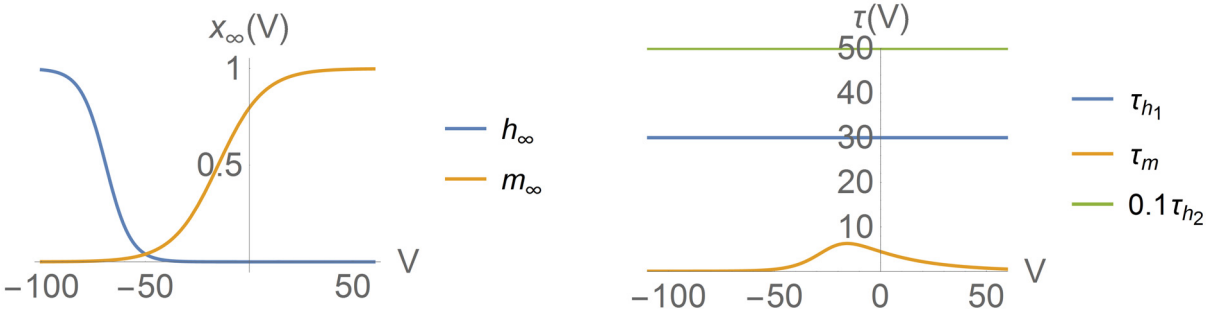

(d) I_{A}

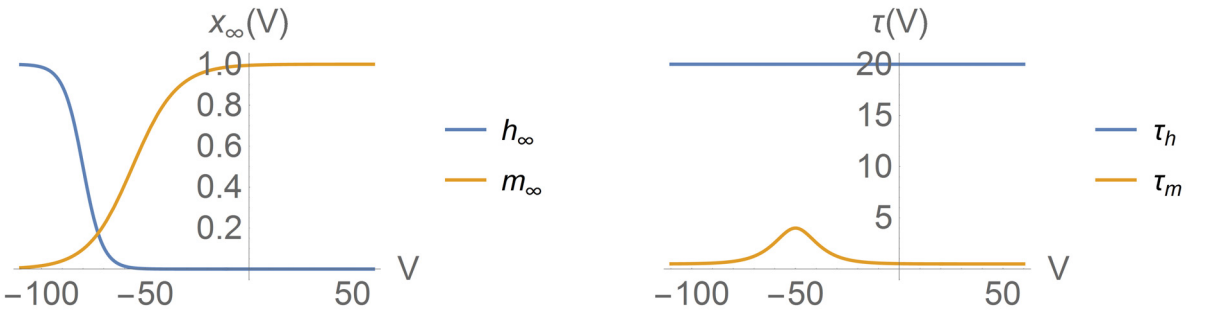

(e) I_{LVA}

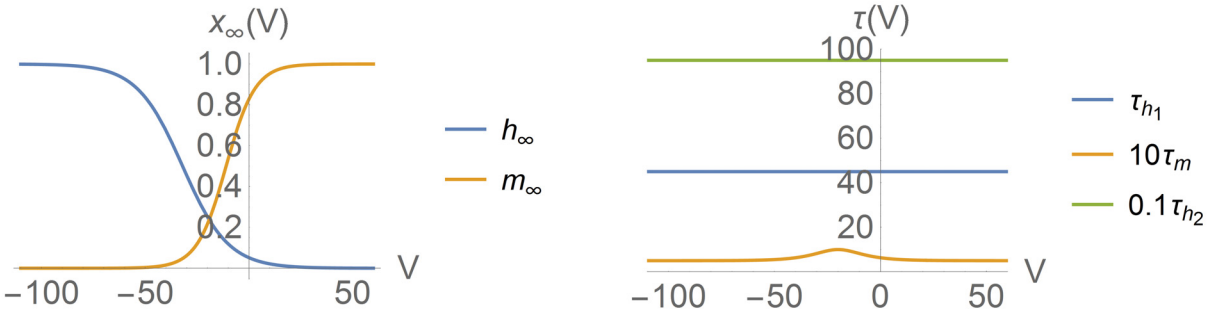

(f) I_{HVA}

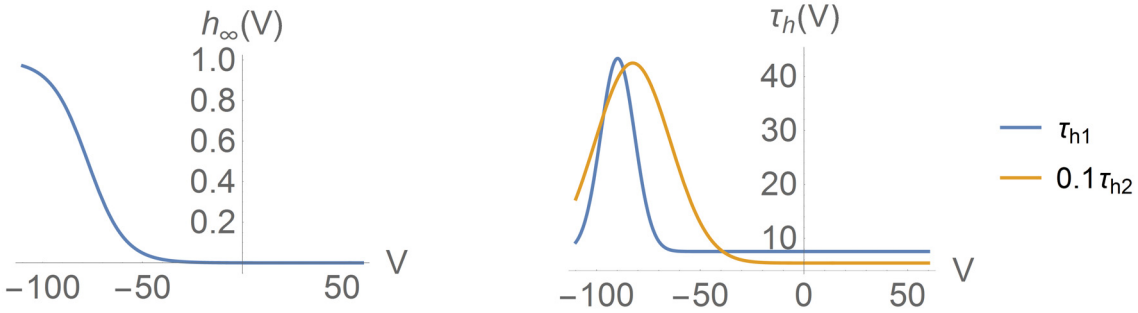

(g) I_{h}

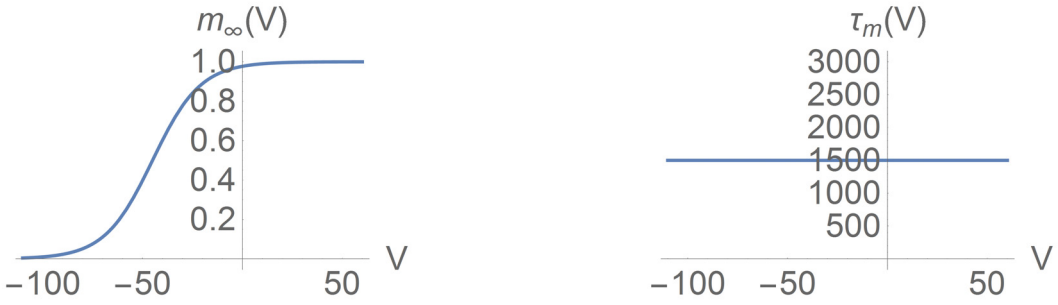

(h) I_{s}

Figure A.3.1: Kinetic curves for voltage-gated currents in the GnRH neuron model.

Bibliography

[1] Wen Duan, Kiho Lee, Allan E. Herbison, and James Sneyd. A mathematical model of adult GnRH neurons in mouse brain and its bifurcation analysis. *Journal of Theoretical Biology*, 276(1):22–34, 2011.

[2] Marc E. Freeman, David R. Grattan, and Thomas A. Houpt. *Neuroscience in Medicine*. Humana Press, third edition, 2008.

[3] Suzanne M. Moenter. Identified GnRH neuron electrophysiology: A decade of study. *Brain Research*, 1364:10–24, 2010.

[4] P E Belchetz, T M Plant, Y Nakai, E J Keogh, and E Knobil. Hypophysial responses to continuous and intermittent delivery of hypopthalamic gonadotropin-releasing hormone. *Science (New York, N.Y.)*, 202(February):631–633, 1978.

[5] L Wildt, A Häusler, G Marshall, J S Hutchison, T M Plant, P E Belchetz, and E Knobil. Frequency and amplitude of gonadotropin-releasing hormone stimulation and gonadotropin secretion in the rhesus monkey. *Endocrinology*, 109:376–385, 1981.

[6] Suzanne M. Moenter, Z. Chu, and C. A. Christian. Neurobiological mechanisms underlying oestradiol negative and positive feedback regulation of gonadotrophin-releasing hormone neurones. In *Journal of Neuroendocrinology*, volume 21, pages 327–333, 2009.

[7] A Dutton and R E Dyball. Phasic firing enhances vasopressin release from the rat neurohypophysis. *The Journal of physiology*, 290:433–440, 1979.

[8] R J Bicknell. Optimizing release from peptide hormone secretory nerve terminals. *The Journal of experimental biology*, 139:51–65, 1988.

[9] Katarzyna M. Glanowska and Suzanne M. Moenter. Differential Regulation of GnRH Secretion in the Preoptic Area (POA) and the Median Eminence (ME) in Male Mice. *Endocrinology*, 156(January):231–241, 2015.

[10] Z. Chu, M. Tomaiuolo, R. Bertram, and S. M. Moenter. Two Types of Burst Firing in Gonadotrophin-Releasing Hormone Neurones. *Journal of Neuroendocrinology*, 24:1065–1077, 2012.

[11] Craig S Nunemaker, R Anthony Defazio, and Suzanne M Moenter. Episodic Firing Patterns of GnRH Neurons. *Endocrinology*, 143(6):2284–2292, 2002.

[12] K. Lee, X. Liu, and A. E. Herbison. Burst Firing in Gonadotrophin-Releasing Hormone Neurones does not Require Ionotrophic GABA or Glutamate Receptor Activation. *Journal of Neuroendocrinology*, 24(18):1476–1483, 2012.

[13] Craig S Nunemaker, R Anthony DeFazio, and Suzanne M Moenter. Calcium current subtypes in GnRH neurons. *Biology of reproduction*, 69(August):1914–1922, 2003.

[14] W.B. Adams and J.A. Benson. The generation and modulation of endogenous rhythmicity in the aplysia bursting pacemaker neurone R15. *Prog. Biophys. Molec. Bio.*, 46:1–49, 1985.

[15] Craig S. Nunemaker, Martin Straume, R. Anthony Defazio, and Suzanne M. Moenter. Gonadotropin-releasing hormone neurons generate interacting rhythms in multiple time domains. *Endocrinology*, 144(February):823–831, 2003.

[16] Yong Wang, Mona Garro, and M. Cathleen Kuehl-Kovarik. Estradiol attenuates multiple tetrodotoxin-sensitive sodium currents in isolated gonadotropin-releasing hormone neurons. *Brain Research*, 1345:137–145, 2010.

[17] Xinhuai Liu and Allan E. Herbison. Small-conductance calcium-activated potassium channels control excitability and firing dynamics in Gonadotropin-Releasing Hormone (GnRH) neurons. *Endocrinology*, 149(7):3598–3604, 2008.

[18] Jianli Sun, Zhiguo Chu, and Suzanne M Moenter. Diurnal in vivo and rapid in vitro effects of estradiol on voltage-gated calcium channels in gonadotropin-releasing hormone neurons. *The Journal of neuroscience*, 30(11):3912–3923, 2010.

[19] J. Pielecka-Fortuna, R. A. DeFazio, and S. M. Moenter. Voltage-Gated Potassium Currents Are Targets of Diurnal Changes in Estradiol Feedback Regulation and Kisspeptin Action on Gonadotropin-Releasing Hormone Neurons in Mice. *Biology of Reproduction*, 85(July):987–995, 2011.

[20] Zhiguo Chu, Hiroshi Takagi, and Suzanne M Moenter. Hyperpolarization-activated currents in gonadotropin-releasing hormone (GnRH) neurons contribute to intrinsic excitability and are regulated by gonadal steroid feedback. *The Journal of neuroscience*, 30(40):13373–13383, 2010.

[21] Zhiguo Chu, Josefa Andrade, Margaret a Shupnik, and Suzanne M Moenter. Differential regulation of gonadotropin-releasing hormone neuron activity and membrane properties by acutely applied estradiol: dependence on dose and estrogen receptor subtype. *The Journal of neuroscience*, 29(17):5616–5627, 2009.

[22] R Anthony DeFazio and Suzanne M Moenter. Estradiol feedback alters potassium currents and firing properties of gonadotropin-releasing hormone neurons. *Molecular endocrinology (Baltimore, Md.)*, 16(10):2255–2265, 2002.

[23] Yong Wang and M. Cathleen Kuehl-Kovarik. Estradiol directly attenuates sodium currents and depolarizing afterpotentials in isolated gonadotropin-releasing hormone neurons. *Brain Research*, 1436:81–91, 2012.

[24] Zhiguo Chu and Suzanne M Moenter. Physiologic regulation of a tetrodotoxin-sensitive sodium influx that mediates a slow afterdepolarization potential in gonadotropin-releasing hormone neurons: possible implications for the central regulation of fertility. *The Journal of neuroscience*, 26(46):11961–11973, 2006.

[25] Chun Xu, Troy A. Roepke, Chunguang Zhang, Oline K. Rø nnekleiv, and Martin J. Kelly. Gonadotropin-releasing hormone (GnRH) activates the M-current in GnRH neurons: An autoregulatory negative feedback mechanism? *Endocrinology*, 149(June):2459–2466, 2008.

[26] Lian Hu, Keiko Wada, Nadia Mores, Lazar Z. Krsmanovic, and Kevin J. Catt. Essential role of G protein-gated inwardly rectifying potassium channels in gonadotropin-induced regulation of GnRH neuronal firing and pulsatile neurosecretion. *Journal of Biological Chemistry*, 281(35):25231–25240, 2006.

[27] Yoshie Hiraizumi, Ichiro Nishimura, Hirotaka Ishii, Nobuyuki Tanaka, Toshiyuki Takeshita, Yasuo Sakuma, and Masakatsu Kato. Rat GnRH neurons exhibit large conductance voltage- and Ca2+-Activated K+ (BK) currents and express BK channel mRNAs. *The journal of physiological sciences*, 58(1):21–29, 2008.

[28] Kiho Lee, Wen Duan, James Sneyd, and Allan E Herbison. Two slow calcium-activated afterhyperpolarization currents control burst firing dynamics in gonadotropin-releasing hormone neurons. *The Journal of neuroscience*, 30(18):6214–6224, 2010.

[29] C Zhang, O K Ronnekleiv, and M J Kelly. Kisspeptin inhibits a slow afterhyperpolarization current via protein kinase C and reduces spike frequency adaptation in GnRH neurons. *American journal of physiology. Endocrinology and metabolism*, 304(11):E1237–44, 2013.

[30] Masakatsu Kato, Kumiko Ui-Tei, Miho Watanabe, and Yasuo Sakuma. Characterization of voltage-gated calcium currents in gonadotropin-releasing hormone neurons tagged with green fluorescent protein in rats. *Endocrinology*, 144(June):5118–5125, 2003.

[31] Chunguang Zhang, Martha A Bosch, Elizabeth A Rick, Martin J Kelly, and Oline K Rø nnekleiv. 17Beta-estradiol regulation of T-type calcium channels in gonadotropin-releasing hormone neurons. *The Journal of neuroscience*, 29(34):10552–10562, 2009.

[32] A. L. Hodgkin and A. F. Huxley. A quantitative description of membrane current and its application to conduction and excitation in nerve. *Bulletin of Mathematical Biology*, 52(1-2):25–71, 1990.

[33] F Van Goor, A P LeBeau, L Z Krsmanovic, A Sherman, K J Catt, and S S Stojilkovic. Amplitude-dependent spike-broadening and enhanced Ca(2+) signaling in GnRH-secreting neurons. *Biophysical journal*, 79(3):1310–1323, 2000.

[34] A P LeBeau, F Van Goor, S S Stojilkovic, and A Sherman. Modeling of membrane excitability in gonadotropin-releasing hormone-secreting hypothalamic neurons regulated by Ca2+-mobilizing and adenylyl cyclase-coupled receptors. *The Journal of neuroscience*, 20(24):9290–9297, 2000.

[35] Carson B. Roberts, M. P. O'Boyle, and K. J. Suter. Dendrites determine the contribution of after depolarization potentials (ADPs) to generation of repetitive action potentials in hypothalamic gonadotropin releasing-hormone (GnRH) neurons. *Journal of Computational Neuroscience*, 26:39–53, 2009.

[36] Patrick A. Fletcher and Yue Xian Li. An integrated model of electrical spiking, bursting, and calcium oscillations in GnRH neurons. *Biophysical Journal*, 96(11):4514–4524, 2009.

[37] Dávid Csercsik, Imre Farkas, Erik Hrabovszky, and Zsolt Liposits. A simple integrative electrophysiological model of bursting GnRH neurons. *Journal of Computational Neuroscience*, 32:119–136, 2012.

[38] P E Latham, B J Richmond, P G Nelson, and S Nirenberg. Intrinsic dynamics in neuronal networks. I. Theory. *Journal of neurophysiology*, 83(2):808–827, 2000.

[39] Xingjiang Chen, Karl Iremonger, Allan Herbison, Vivien Kirk, and James Sneyd. Regulation of Electrical Bursting in a Spatiotemporal Model of a GnRH Neuron. *Bulletin of Mathematical Biology*, 75(10):1941–1960, 2013.

[40] K. J. Iremonger and A. E. Herbison. Initiation and Propagation of Action Potentials in Gonadotropin-Releasing Hormone Neuron Dendrites. *Journal of Neuroscience*, 32(1):151–158, 2012.

[41] Xingjiang Chen and James Sneyd. A Computational Model of the Dendron of the GnRH Neuron. *Bulletin of Mathematical Biology*, pages 904–926, 2014.

[42] G. Bard Ermentrout and David H. Terman. *Mathematical Foundations of Neuroscience*. Springer, New York, 1 edition, 2010.

[43] Lawrence C. Evans. *An Introduction to Stochastic Differential Equations*. American Mathematical Society, 2013.

[44] Peter E. Kloeden and Eckhard Platen. *Numerical Solution of Stochastic Differential Equations*. Springer-Verlag, Berlin, third edition, 1999.

[45] B Ermentrout and A Mahajan. Simulating, Analyzing, and Animating Dynamical Systems: A Guide to XPPAUT for Researchers and Students, 2003.

[46] MATLAB. *version 8.4.0 (R2014b)*. The MathWorks Inc., 2014.

[47] John Rinzel and Young Seek Lee. Dissection of a model for neuronal parabolic bursting. *Journal of Mathematical Biology*, 25:653–675, 1987.

[48] Eugene M. Izhikevich. Neural Excitability, Spiking and Bursting. *International Journal of Bifurcation and Chaos*, 10(6):1171–1266, 2000.

[49] Jonathan E. Rubin and David Terman. Geometric singular perturbation analysis of neuronal dynamics. *Handbook of Dynamical Systems II*, 2:93–146, 2002.

[50] Frank C Hoppensteadt. *Analysis and Simulation of Chaotic Systems*, volume 94 of *Applied Mathematical Sciences*. Springer-Verlag, New York, NY, second edition, 2000.

[51] Euiwoo Lee and David Terman. Uniqueness and stability of periodic bursting solutions. *Journal of Differential Equations*, 158(1):48–78, 1999.

[52] C Soto-Treviño, N Kopell, and D Watson. Parabolic bursting revisited. *Journal of mathematical biology*, 35(1):114–128, 1996.

[53] G. B. Ermentrout and N. Kopell. Parabolic Bursting in an Excitable System Coupled with a Slow Oscillation, 1986.

[54] Richard Bertram, Manish J. Butte, Tim Kiemel, and Arthur Sherman. Topological and phenomenological classification of bursting oscillations. *Bulletin of Mathematical Biology*, 57(3):413–439, 1995.

[55] T. R. Chay and D. L. Cook. Endogenous bursting patterns in excitable cells. *Mathematical Biosciences*, 90(1-2):139–153, 1988.

[56] Eusebius J. Doedel and Bart E. Oldeman. AUTO-07P : Continuation and Bifurcation Software for Ordinary Differential Equations. Concordia University, Montreal, Canada, 2007.

[57] Yuri A Kuznetsov. Elements of Applied Bifurcation Theory. *Elements*, page 591, 1998.

[58] Paul Smolen, David Terman, and John Rinzel. SIAM Journal on Applied Mathematics,. *SIAM Journal on Applied Mathematics*, 53(3):861–892, 1993.

[59] S M Baer, J Rinzel, and H Carrillo. Analysis of an autonomous phase model for neuronal parabolic bursting. *Journal of mathematical biology*, 33(3):309–333, 1995.

[60] Boxun Lu, Yanhua Su, Sudipto Das, Jin Liu, Jingsheng Xia, and Dejian Ren. The Neuronal Channel NALCN Contributes Resting Sodium Permeability and Is Required for Normal Respiratory Rhythm. *Cell*, 129:371–383, 2007.

[61] Charles F. Stevens. Interactions between intrinsic membrane protein and electric field. *Biophysical Journal*, 22:295–306, 1978.

[62] J R Huguenard and D A McCormick. Simulation of the currents involved in rhythmic oscillations in thalamic relay neurons. *Journal of neurophysiology*, 68(4):1373–1383, 1992.

[63] A Destexhe, Z F Mainen, and T J Sejnowski. Synthesis of models for excitable membranes, synaptic transmission and neuromodulation using a common kinetic formalism. *Journal of computational neuroscience*, 1(3):195–230, 1994.

[64] Henrike Berkefeld, Bernd Fakler, and U Schulte. Ca2+-activated K+ channels: from protein complexes to function. *Physiological reviews*, 90(90):1437–1459, 2010.

[65] John R Clay, David Paydarfar, and Daniel B Forger. A simple modification of the Hodgkin and Huxley equations explains type 3 excitability in squid giant axons. *Journal of the Royal Society, Interface / the Royal Society*, 5(29):1421–1428, 2008.

[66] D Purves, GJ Augustine, D Fitzpatrick, and LC Katz. *Neuroscience. 2nd edition.* Sinauer Associates, 2001.

[67] Wulfram Gerstner and Werner M. Kistler. *Spiking Neuron Models.* Cambridge University Press, 2002.

[68] Allan R. Willms, Deborah J. Baro, Ronald M. Harris-Warrick, and John Guckenheimer. An improved parameter estimation method for Hodgkin-Huxley models. *Journal of Computational Neuroscience*, 6:145–168, 1999.

[69] Allan R. Willms. NEUROFIT: Software for fitting Hodgkin-Huxley models to voltage-clamp data. *Journal of Neuroscience Methods*, 121:139–150, 2002.

[70] J Magistretti and A Alonso. Biophysical properties and slow voltage-dependent inactivation of a sustained sodium current in entorhinal cortex layer-II principal neurons: a whole-cell and single-channel study. *The Journal of general physiology*, 114(September):491–509, 1999.

[71] J M Bekkers. Properties of voltage-gated potassium currents in nucleated patches from large layer 5 cortical pyramidal neurons of the rat. *The Journal of physiology*, 525 Pt 3(2000):593–609, 2000.

[72] C T Dickson, J Magistretti, M H Shalinsky, E Fransén, M E Hasselmo, and a Alonso. Properties and role of I(h) in the pacing of subthreshold oscillations in entorhinal cortex layer II neurons. *Journal of neurophysiology*, 83:2562–2579, 2000.

[73] Dan Bar-Yehuda and Alon Korngreen. Space-clamp problems when voltage clamping neurons expressing voltage-gated conductances. *Journal of neurophysiology*, 99(3):1127–1136, 2008.

[74] P. J. Hemond, M. P. O'Boyle, C. B. Roberts, A. Delgado-Reyes, Z. Hemond, and K. J. Suter. Simulated GABA Synaptic Input and L-Type Calcium Channels Form Functional Microdomains in Hypothalamic Gonadotropin-Releasing Hormone Neurons. *Journal of Neuroscience*, 32(26):8756–8766, 2012.

[75] Timothy O'Leary, Alex H. Williams, Alessio Franci, and Eve Marder. Cell Types, Network Homeostasis, and Pathological Compensation from a Biologically Plausible Ion Channel Expression Model. *Neuron*, 82(4):809–821, 2014.

[76] X J Wang and G Buzsáki. Gamma oscillation by synaptic inhibition in a hippocampal interneuronal network model. *The Journal of neuroscience*, 16(20):6402–6413, 1996.

[77] Travis E Oliphant. SciPy: Open source scientific tools for Python. *Computing in Science and Engineering*, 9:10–20, 2007.

[78] Gwendal LeMasson and Reinoud Maex. *Introduction to Equation Solving and Parameter Fitting. In: Computational neuroscience: Realistic modeling for experimentalists*. CRC Press, 2001.

[79] A. Foroush Bastani and S. Mohammad Hosseini. A new adaptive Runge-Kutta method for stochastic differential equations. *Journal of Computational and Applied Mathematics*, 206(2):631–644, 2007.

[80] C A Vandenberg and F Bezanilla. A sodium channel gating model based on single channel, macroscopic ionic, and gating currents in the squid giant axon. *Biophysical journal*, 60(6):1511–1533, 1991.

[81] Chung Chin Kuo and Bruce P. Bean. Na+ channels must deactivate to recover from inactivation. *Neuron*, 12:819–829, 1994.

[82] Pablo Achard and Erik De Schutter. Complex parameter landscape for a complex neuron model. *PLoS Computational Biology*, 2(7):0794–0804, 2006.

[83] Werner Van Geit, Pablo Achard, and Erik De Schutter. Neurofitter: a parameter tuning package for a wide range of electrophysiological neuron models. *Frontiers in neuroinformatics*, 1(November):1, 2007.

[84] R E Plant. Bifurcation and resonance in a model for bursting nerve cells. *Journal of mathematical biology*, 11:15–32, 1981.

[85] André Longtin, Carlo Laing, and Maurice J Chacron. *Processes with Long-Range Correlations*, volume 621. Springer-Verlag, Berlin, 2003.

[86] Eugene M Izhikevich. *Dynamical Systems in Neuroscience*. 2007.

[87] Jonathan P. Newman and Robert J. Butera. Mechanism, dynamics, and biological existence of multistability in a large class of bursting neurons. *Chaos*, 20(2), 2010.

[88] Hiroshi Hibino, Atsushi Inanobe, Kazuharu Furutani, Shingo Murakami, and I a N Findlay. Inwardly Rectifying Potassium Channels : Their Structure, Function, and Physiological Roles. *Physiology Reviews*, 90:291–366, 2010.